DEVELOPING MICROFLUIDIC SYSTEMS TO RESOLVE LONGSTANDING HEMATOLOGIC QUESTIONS

A Dissertation
Presented to
The Academic Faculty

by

Jordan Ciciliano

In Partial Fulfillment
of the Requirements for the Degree
Doctor of Philosophy in Bioengineering

Parker H. Petit Institute for Bioengineering and Bioscience
Georgia Institute of Technology
August 2017

DEVELOPING MICROFLUIDIC SYSTEMS TO RESOLVE LONGSTANDING HEMATOLOGIC QUESTIONS

Approved by:

Dr. Wilbur A. Lam, Advisor
School of Engineering
Wallace H. Coulter Department of Biomedical Engineering
Georgia Institute of Technology

Dr. Susan Thomas
School of Mechanical Engineering
Georgia Institute of Technology

Dr. J. Brandon Dixon
School of Mechanical Engineering
Georgia Institute of Technology

Dr. Hua Wang
School of Electrical Engineering
Georgia Institute of Technology

Dr. Todd Sulchek
School of Mechanical Engineering
Georgia Institute of Technology

Date Approved: June 27, 2017

ACKNOWLEDGEMENTS

I wish to acknowledge the following people for their continued support throughout my graduate work. I never in a million years dreamed that I would earn a PhD and it would not have been possible without the support of so many wonderful people.

My advisor—

Thank you to my advisor, **Wilbur A. Lam**, for his guidance and support throughout graduate school. I came to graduate school looking for a mentor who would support my independence and let me make my own way, and what I found was so much more. Wilbur's door was always open to discuss crazy ideas, frustrations, career plans, life struggles, not to mention scientific breakthroughs and setbacks. Armed with coffee and Kleenex, Wilbur was ready to take my sass and fire, and turn it in to productivity; for that, I will always be thankful.

Committee—

Dr. J. Brandon Dixon for his help in modeling flux to create an *in vitro* representation of an *in vivo* model.

Dr. Susan Thomas for her role in my development as a graduate student, from qualifying exams to my teaching practicum to honest feedback about my work.

Dr. Todd Sulchek for his help in brainstorming microfluidic devices for monitoring blood cell deformability.

Dr. Hua Wang for bringing his knowledge of electrical engineering and sensors to discussions about my work.

Collaborators—

Thank you to all of my collaborators across disciplinary bounds, without whom my understanding of the many fields I sought to explore would be sorely lacking. Special thanks to **Dr. Andrew Lyon** for helping me to grasp colloidal chemistry, **Dr. Christian Gachet** and **Beatrice Hechler** for their assistance with animal experiments, and **Reza Abbaspour** and **Dr. Bakir** for their fabrication expertise in the cell deformation project.

Laura Paige—

Thank you for knowing exactly what forms needed to be completed, what people needed to be consulted, and most importantly, for always being a warm and welcoming presence.

Lab family—

Many thanks to the Lam lab, where I found a home, a support network, and lifelong friends. I'm so glad that we chose each other five years ago, and that we have since shared many successes, opportunities for improvement (failures), and cakes. With such an eclectic collection of personalities and areas of expertise, we make a wonderful, and oftentimes dysfunctional, family. Special thanks to **Yumiko Sakura** for being the heart and soul of the lab (and for teaching me to knit!). To **Yumiko**, **Erika Tyburski**, my fellow graduate students— **Dr. Reggie Tran, Rob Mannino, Meredith Fay, Caroline Hansen, Jessica Lin**— and the doctors— **Dr. Hope Gole, Dr. Elaissa Hardy, Dr. David Myers, Dr. Yong Qiu, Dr. Byungwook Ahn, Dr. Margo Rollins, Dr. Sarah Mitchell, Dr. Marcus Carden**—, thank you for your friendship, for your being there to celebrate and commiserate

at every stage in the graduate school journey, as well as for your insightful scientific (and non-scientific) discussions and guidance (and for dealing with my opinionated commentary on any and every topic). From hot dog eating contests to craft fairs to heated lab debates, I couldn't have asked for a better crew.

A special thank you to **Julia Woodall** for her help in the schistocyte project, and for being patient with me as I grew as a mentor.

Rugby family—

Rugby has been my outlet in graduate school. Many thanks to my teammates and friends who made my research journey manageable through encouragement, hard hits, socials, and the bond that only rugby can bring. The ARC Angels and Atlanta Harlequins will always have a place in my heart (and on my couch)!

Friends—

Thank you to my many friends spread around the country who have played an indispensable role in my life; I carry each of you with me everywhere I go.

Dr. Judy Dickson – My graduate student (and rugby) partner in crime, hailing from a different discipline but somehow always asking the right questions, having the reasonable answers, and giving the best advice. Judy has given me endless support (and more importantly, tough love) in graduate school, in the gym, on the rugby pitch, and in life. Our coffee dates propelled me headlong through this process, and though we are headed to separate states, I will always call her my sister.

Family—

Every day of childhood I wanted to emulate **my brother**, Dylan; he has always served as an exquisite example of intellectual prowess, and I credit him for my stubborn drive to always figure out the "right" answer.

My **mom and dad** instilled in me a love of learning, and for that I cannot thank them enough. More importantly, they have shown me what it is to work hard, how it feels to love and be loved, and the many places in which success and happiness are found. I am beyond proud to be their daughter and I am honored to call them my friends. This success is not mine alone, but to be shared with my parents completely.

TABLE OF CONTENTS

LIST OF TABLES

Page

LIST OF FIGURES

Page

LIST OF SYMBOLS AND ABBREVIATIONS

BSA	Bovine Serum Albumin
CAD	Computer Aided Design
HUVEC	Human Umbilical Vein Endothelial Cell
$FeCl_3$	Ferric Chloride
$AlCl_3$	Aluminum Chloride
$CrCl_3$	Chromium Chloride
PPP	Platelet Poor Plasma
PRP	Platelet Rich Plasma
RBC	Red Blood Cell
WBC	White Blood Cell
PDMS	Polydimethylsiloxane
EBL	Electron-beam Lithography
PECVD	Plasma Enhanced Vapor Deposition
HMDS	Hexamethyldisiloxane
SCD	Sickle Cell Disease
$\dot{\gamma}$	Shear Rate (s^{-1})
η	Dynamic Viscosity ($kg \cdot m^{-1} \cdot s^{-1}$)
τ	Shear Stress ($dyn \cdot s^{-1}$)
Q	Flow Rate ($cm^3 \cdot s^{-1}$)
μ	Viscosity
V	Volume
P	Pressure

R	Resistance
R_H	Hydraulic Resistance
w	Channel Width
h	Channel Height
l	Channel Length

SUMMARY

Recent research has revealed that cells dynamically sense and respond to their physical microenvironments. In hematology, it has been shown that shear mediated red blood cell (RBC) deformation results in release, and that platelets attenuate contraction force based on substrate stiffness. Blood cells exist in a dynamic fluidic microenvironment, and they also interact with various matrices such as fibrin clots and the extracellular matrix proteins. The objective of this thesis is thus to create microfluidic systems in which the biophysical and biochemical aspects of hematological processes are independently investigated toward the aim of discovering new solution spaces for diagnostics and therapeutics. To that end, this work presents novel microfluidic systems: 1) an "endothelial"-ized, T-junction fluidic to elucidate the biophysical processes that define the mechanism of action of the ferric chloride thrombosis model and 2) microfluidic devices with single-micron features (pillars and canals) to examine the effects of physical interactions between blood cells—RBCs, platelets, and neutrophils—and geometrically relevant, non-biological matrices at the single cell level.

Using the T-junction fluidic I resolved the mechanism of action of the most commonly used thrombosis injury model – the ferric chloride- thrombosis model. I show that the mechanism of action of ferric chloride is non-biological in nature. Rather, the chemical induces charge-based aggregation of blood cells that then triggers the conventional clotting cascade. This finding both reconciles discrepancies in the literature, and cautions researchers against using this injury model, especially for the study of clot initiation. My work also highlights the importance of considering mass transfer properties in biological processes.

The second suite of devices recapitulates the physical dimensions of vascular matrices with which blood cells interact. By combining electron beam lithography, photolithography, and soft lithography, I considered hematological questions that were previously technologically infeasible. I found that the physical presence of a micropillar array creates a shear microgradient that leads to the localized adherence and aggregation of platelets that propagates to stem blood flow in the absence of exogenous agonists. Furthermore, I visualized the process of RBC fragmentation (schistocyte formation) real-time in an *in vitro* system by creating microcanals that force RBCs to deform through a small cross-sectional area over various distances. This suggests that RBC fragmentation is a time dependent process, contrary to what is historically cited in medical literature. Furthermore, pathologically altered cells—RBCs from a patient with SCD—have an altered fragmentation profile as compared to healthy cells. Finally, by perfusing neutrophils through the microcanals, I show that mechanical forces can cause neutrophils to fragment into membranous debris that has neutrophil extracellular trap (NET)-like properties. These NET-like surfaces appear to be procoagulant in that they bind platelets and display histone, elastase and MPO. This suggests new insight into the pathological role of neutrophils in thrombosis. Moreover, RBCs become trapped in the neutrophil membrane, and can hemolyze as a result. This system them provides insights into the synergy between hemolytic anemias, sepsis, and thrombosis. Microfluidic platforms allow for real-time, microscopic evaluation of cell response (via both brightfield morphology analysis and immunostaining) and precise spatiotemporal control of system inputs and flow characteristics, including shear stress. The mechanistic understandings gained by creating systems that successfully decouple the biophysical and biological aspects of blood cells, as

is done in this work, can result in enhanced understanding of the etiology of pathologies, improved diagnostic assays for blood cell activity, and new targets for therapeutics.

CHAPTER 1: INTRODUCTION

In vivo animal models and *in vitro* biological assays continue to be indispensable to the study of hematology. However, as recent research reveals that cells dynamically sense and respond to their physical microenvironments, assays that decouple biophysical and biological processes have become increasingly important. Blood cells pass through, and interact with, biological matrices such as fibrin clots and endothelial cell gaps, but the physical and biochemical aspects of these interactions are relatively indistinguishable from one another in vivo. A more global understanding of the effects of biophysical factors—e.g. mass transfer, pressure, and physical dimensions– on hematological processes will inform the field towards a new set of solutions.

1.1 Motivation

Numerous cellular mechanics studies have shown that cells dynamically sense and respond to physical signals in their microenvironments.[1, 2] As blood cells exist in a biological environment that is governed by fluid mechanics, their response to biophysical stimuli is of great interest. Hemostasis, or the cessation of blood flow, is a tenuous system made up of feedback loops that ensure that clotting stops blood loss, but does not impede blood flow; therefore, both the inability to clot and pathological clotting (thrombosis) form a significant body of research in hematology. Cardiovascular disease is the leading cause of death globally, and thrombosis is the underlying pathology in conditions such as heart attack and stroke. Further, thrombosis resulting from medical implants presents a new avenue for research considerations. Clotting is known to be regulated by physical processes in a number of ways: mass transfer of clotting agonists from the injury site, elevated shear causing platelet activation and aggregation, disturbed flow causing endothelial cell

dysfunction, etcetera. [3] Physical alterations in the fluidic environment, such as in stenotic vessels or implanted heart valves, then greatly affects hemostasis and pathological clotting. Having a better understanding of the effects of physical parameters on blood cells gives a more global understanding of hematology and thus presents a previously unconsidered realm of solutions for blood cell activity assays and antithrombotic therapeutics.

1.2 Research Objectives and Specific Aims

The *long term goal* of the project is to enhance understanding of the biophysical aspects of hematological processes to improve diagnostic assays and to inspire the discovery of novel therapeutic targets. The *overall objective* of this work is to develop microfluidic systems in which precise spatiotemporal control of experimental conditions allows for biological and biophysical effects to be considered independently, towards the aim of resolving unknown mechanisms in hematology. My ***central hypothesis*** is that microfluidics can be leveraged to study hematological processes in a reductionist manner, where confounding biological and biophysical factors are considered both in isolation and in conjunction, with the aim of resolving longstanding questions in hematology. My central hypothesis will be tested in the following specific aims:

Aim 1. Resolve the mechanism of the ferric chloride ($FeCl_3$) injury model. A T-junction microfluidic was designed to recapitulate the introduction of $FeCl_3$ to a blood vessel lumen. By introducing $FeCl_3$ to blood components and endothelial cells in a reductionist manner, I could resolve the mechanism of injury in the $FeCl_3$-induced thrombosis model. Flow into each channel can be controlled by a syringe pump to create an interface of the two fluid

streams near the wall of the main channel (as it would in the luminal introduction of a chemical *in vivo*) for the real-time monitoring of blood cell aggregation. Individual blood cells can thus be exposed to $FeCl_3$, in the presence and absence of endothelial cells, to explore the many interrelated facets of the *in vivo* experimental space. Furthermore, the *in vitro* model can assess the effects of $FeCl_3$ in altered clotting environments (in the presence of therapeutics and in clotting deficient blood), to have a more global understanding of the injury mechanism. Finally, by characterizing the role of mass transfer in this model, the experimental differences related to the concentration of $FeCl_3$ and the vessel it is applied to can be elucidated. Chapter 3 describes this work and concludes with a description of the mechanism of the injury model.

Aim 2. Create a suite of devices to probe the interaction of blood cells with their physical microenvironment. The *working hypothesis* was that a combination of microfabrication techniques could be leveraged to create microfluidic devices that allow for the recapitulation of interactions between single blood cells and their physical microenvironments. The interaction of cells with these physical structures could then be monitored real time via microscopy to have a better understanding of biophysical stimulus on blood cells. Electron beam lithography (EBL), in combination with photolithography and soft lithography, can be used to create microfluidic devices with robust, repeatable, single micron features. To that end, I created an array of micropillars that recapitulates the gaps and fibers that a platelet would traverse and interact with, to establish the effect of a physical matrix on platelet activation and aggregation. The interaction of the biophysical and biochemical can be probed by adsorbing biologics to the micropillar surfaces. For the

second half of this aim, I designed and fabricated a microcanal device that challenges RBCs to deform through a 2x3 μm cross-section over various distances. RBCs are monitored real time to gain insight into the parameter space for RBC fragmentation. Blood from a patient with SCD was perfused through the microcanal array to determine how pathological changes in RBCs change their fragmentation profile. Finally, neutrophils can be perfused through the microcanal array to monitor their interaction with the physical barrier. Neutrophils, red blood cells, and platelets can then be perfused through the microcanal device to better understand how the cells interact with one another as well as with the physical matrix. The experimental procedures and results of these studies are described in Chapter 4.

1.3 Significance of Results

The results of this work have significant impacts for the field of hematology. The successful completion of the first aim—to resolve the mechanism of action of the $FeCl_3$ injury model—both resolves discrepancies between previous literature findings in the field and cautions researchers on the use of the injury model in future research. By showing that the initiation of clotting in this model is non-biological in nature, I suggest that the model not be used to describe the biological receptor-ligand interactions of clot initiation. Further, results must be interpreted cautiously when using this model as there are likely significant, unknowable experimental artifacts. I also found that the extent of thrombosis in this model was directly related to mass transfer of $FeCl_3$ in the vessel, thus providing insight into differences reported in the literature for thrombosis in different vessel types (that vary in diameter and blood velocity, and thus mass transfer parameters).

The work completed in the second aim serves to begin to decouple the biophysical cues of vascular matrices from the biochemical. This is especially important when considering the widespread clotting that occurs in a number of disparate disease states, from sickle cell disease to sepsis. By creating a suite of devices that have single-micron scale features, I have created enabling technology that allows for the real-time monitoring of interactions between blood cells and their physical microenvironment. I show that the physical microenvironment, in and of itself, is able to regulate platelet activity. Further, that red blood cell fragmentation is a force and time dependent process, and that schistocytes and red blood cell derived microparticles can be created through a purely mechanical process. Finally, I show that the mechanical disruption of a neutrophil under flow results in "NET-like" membranous material whose backbone is DNA and that is studded with histone, elastase, and MPO. When the components are considered together, I find that mechanically induced NET-like material is procoagulant and entraps RBCs, as is seen in NETs implicated in thrombosis *in vivo.* Overall my findings suggest a role for cellular mechanics at the interface of inflammation and clotting, and informs how cell types respond in concert to biophysical challenges. This novel result is both pathophysiologically and clinically relevant as it gives insight into disease state and relevant biophysical processes.

CHAPTER 2: BACKGROUND

2.1 Hemostasis

2.1.1 Blood Components

Blood is a colloidal suspension of cells in a protein-rich aqueous solution. Broadly, red blood cells (5 billion cells/ mL of blood) are anuclear cells whose chief role is in oxygen transport throughout the body. White blood cells (5 million/ mL) are primarily involved in the immune response, with the greatest subset—granulocytes—being the noted first-responder of the innate immune system. Platelets (500 million / mL) are fragments of megakaryocytes that form the main cellular component of clots. Blood proteins play various physiological roles ranging from the transport of nutrients and hormones to the regulation of clotting and the activation of the immune system. Of particular importance to clotting are fibrinogen, the fibrous component of clots, and coagulation factors, which circulate in a quiescent state. Blood cells and proteins play an interconnected role in physiologic and pathologic processes, the extent and details of which are still being discovered.

2.1.2 Clotting Cascade

Integral to the study of hematology is an understanding of hemostasis, or the cessation of blood flow. There is a tenuous balance between insufficient clotting and excessive clotting (thrombosis) that must be maintained for physiological function. To this end there are tightly controlled positive and negative feedback loops to provide a rapid, localized

response to blood vessel damage. The coagulation cascade describes the positive feedback loop, and is an extraordinarily complex series of reactions that converts coagulation factors to their active states; it is typically divided into two pathways: contact activation (extrinsic) and tissue factor (intrinsic). These pathways converge in a common pathway whereby thrombin is produced, which then converts fibrinogen to its polymerized form, fibrin. Fibrin binds platelets that have bound to the injury site and those in flow, and the combined platelets and fibrin form a hemostatic plug. Platelets gradually contract, expelling liquid and allowing the fibrin/ platelet clot to effectively seal off the injury while minimally obstructing blood flow. It should be noted that the distinction between the contact and tissue factor pathways is one made in controlled *in vitro* experiments; in reality, both processes likely occur in tandem *in vivo*.

Briefly, the contact pathway describes the process by which factors are activated when interacting with a negatively charged surface. This surface can be a foreign body (e.g., glass) or the activated surface of a platelet or white blood cell. Deficiencies in the contact pathway seem to have consequences for thrombosis, but not explicitly for hemostasis. The tissue factor pathway is more integral to hemostasis (Figure 2.1); a deficiency in this pathway's coagulation factors leads to a bleeding disorder (e.g., factors VII and VIII in hemophilia). Briefly, the tissue factor pathway describes the process by which exposure of the subendothelium leads to release of tissue factor. Tissue factor then activates coagulation factors. As stated, both pathways result in the crosslinking of fibrinogen into insoluble fibrin that forms the fibrous, mesh component of clots.

Platelets play an integral role in the initiation, propagation, and resolution of clotting. In addition to the tissue factor produced during endothelial injury, the injury physically

exposes the subendothelial matrix, namely collagen and fibronectin, to which platelets bind via transmembrane proteins called integrins. Platelet arrest and activation leads to their release of soluble agonists, which further recruits and activates platelets.[4] Platelets can also be activated by thrombin and elevated shear stress. When platelets are activated, the usually internal phospholipid, phosphatidylserine, moves to the outer surface and creates a local procoagulant surface. In arteries where fluid forces are of a certain magnitude, von Willebrand Factor (vWF) also plays a role in platelet arrest and clot propagation.

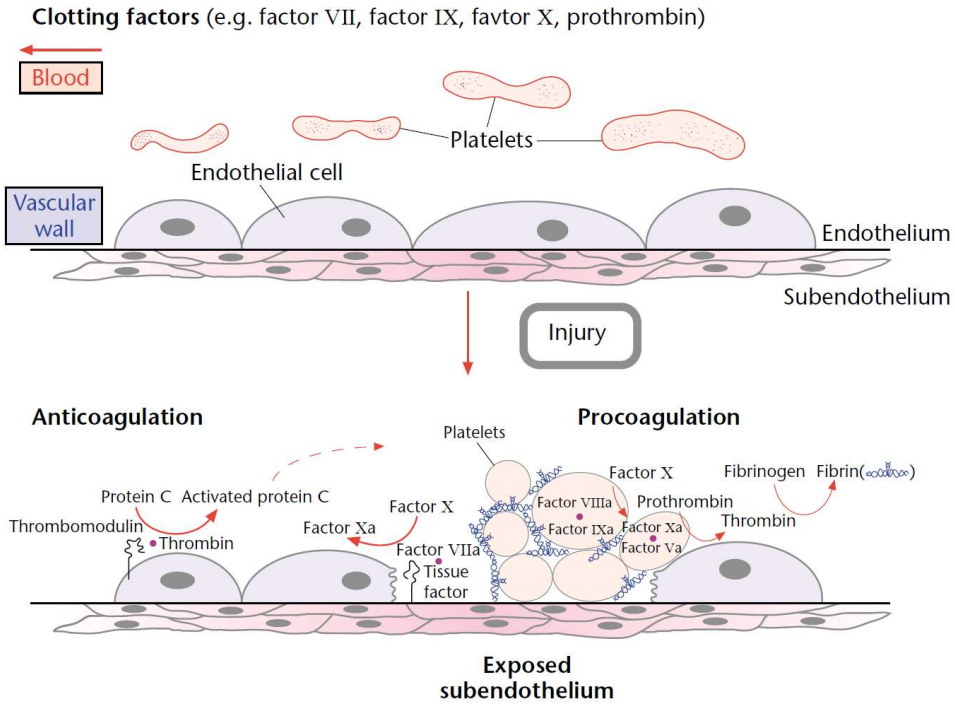

Figure 2.1. The haemostatic response to injury. When the endothelium is disrupted by injury, tissue factor (which is not present on platelets, or on endothelial cells under normal physiological conditions) is exposed to factor VIIa to initiate the complex series of reactions… which give rise to fibrin. The fibrin monomer, which is composed of three different proteins, undergoes polymerization and binds with platelets to the subendothelium to form a haemostatic plug, called the thrombus. Platelets normally circulate in a resting form but are activated at the site of injury, releasing many different chemicals from granules inside the cell (indicated here as grains in the circulating platelets) which are important to platelet adhesion, aggregation and coagulation. Taken from [5].

While RBCs do not play an immediate known biochemical role in the coagulation process, due to their significant numbers in circulation, they become trapped in fibrin clots and interact extensively with clots, especially in the microcirculation (Figure 2.2). Likewise, white blood cells have been shown to interact with platelets and contribute to the tissue factor branch of the coagulation cascade.

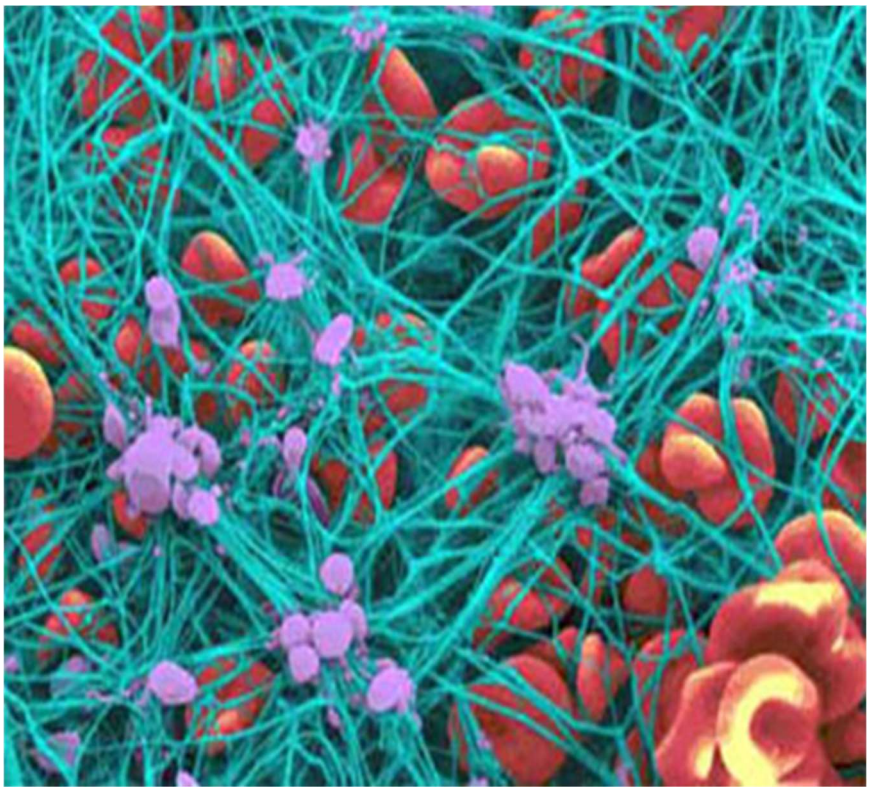

Figure 2.2 SEM of blood clot. Fibrin (green) and platelets (purple) form the structural meshwork of the clot, while red blood cells (red) and white blood cells are trapped in the meshwork. Image **Microfluidics**

While *in vivo* animal models allow for the systemic study of biological processes, the inherent complexity of a living system presents difficulties in studying the role of individual components, as well as in studying the interplay between biochemical and biophysical factors. Similarly, traditional *in vitro* biological assays often require large reagent volumes and are performed in a 2-dimensional environment. The advent of

microfluidics has allowed for the study of biological systems in a 3-dimensional system that gives researchers spatio-temporal control over experimental inputs. Microfluidic systems can thereby incorporate some of the global aspects of *in vivo* models with the precise control of traditional *in vitro* assays. While microfluidics do not replace the utility of animal models, microfluidics can serve as complimentary platforms for understanding biological processes.

Microfluidic systems allow for the handling and manipulation of sub-microliter volumes of fluids in micron-sized channels, and these devices have found many applications, including chemical analysis, lower cost biological assays, and recapitulation of physiological systems. The technology for microfluidic design and fabrication hails from the microchip industry, whereby numerous lithography techniques are employed to transfer features from a pattern to silicon and glass[6]—photolithography and electron beam lithography (EBL) are used in this work. While silicon and glass have been used in microfluidic chips, polymers and plastics are generally preferable due to their transparent nature, low cost, and ease of mass production (and thus their disposability). Typically, microfluidic templates are made on silicon wafers and then used as a substrate from which features are transferred to an elastomeric substrate, in a process termed soft lithography.[7] Polydimethylsiloxane (PDMS) is the material often chosen for soft lithography for its transparent nature, low cost, readily altered surface properties, and moderate stiffness (~1 MPa) that allows it to conformally contact and bond to other substrates,. Here we will discuss photolithography and electron beam lithography, and how each fabrication technique can be combined with soft lithography to create microfluidic devices.

2.2.1 Photolithography

Photolithography is the transfer of features from a photomask to a given substrate (in this case, a silicon wafer coated with a resin) by way of UV light and downstream chemical treatment. A photomask is created to the required specifications by simple printing or by etching the pattern prescribed by a computer aided design (CAD) file onto a chrome coated soda-lime or quartz substrate. The silicon wafer is spun with photoresist, a chemical substrate that is sensitive to UV light exposure (negative photoresist is crosslinked by UV light, impeding its removal; whereas positive photoresist is made more soluble upon UV light exposure) (Figure 2.3a). A variety of photoresists can be used to achieve different feature sizes, and spin curves are available to determine the spin speed and time required to achieve different feature heights. The negative photoresist SU-8 is often used in the creation of microfluidic devices due its durability and ability to create high aspect ratio, straight walled features. Using a mask aligner (oftentimes in a cleanroom), UV light is shone through the photomask and the photoresist coated silicon wafer is effectively patterned with the CAD features (Figure 2.3b). The silicon wafer is then developed to remove soluble photoresist, resulting in the features specified by the photomask (Figure 2.3c). Feature size is determined by the resolution of the photomask (generally 1-2 μm), the photoresist thickness, and the photolithographic method (contact versus projection). Features as small as 40 nm can be achieved via photolithography but this requires specialized equipment and extensive fabrication expertise. Typically, contact photolithography is used in making microfluidics masters and has a resolution of ~5 μm. To achieve robust, reproducible features, microfluids are typically designed to be on the order of tens to hundreds of microns and fabrication becomes non-trivial at <5 μm.

Once the silicon wafer is patterned via photolithography, it can be repeatedly used as a master from which elastomeric microfluidic devices can be made via soft lithography. To reduce the adherence of PDMS to the silicon wafer, and thereby facilitate the clean release of cured PDMS, the wafer is made hydrophobic by any number of chemical treatments, such as hexamethyldisiloxane (HMDS). Uncured PDMS, usually at a ratio of 1:10 crosslinker: prepolymer, is poured over the treated silicon master, degassed in a vacuum chamber, and cured at 60 C for >3 hours to create a solid, transparent, elastomeric substrate (Figure 2.3 d). The patterned PDMS is then cut out and removed from the wafer (Figure 2.3e). Individual devices are cut out of the PDMS template and holes are punched in the device to serve as inlet and outlet ports (Figure 2.3f).

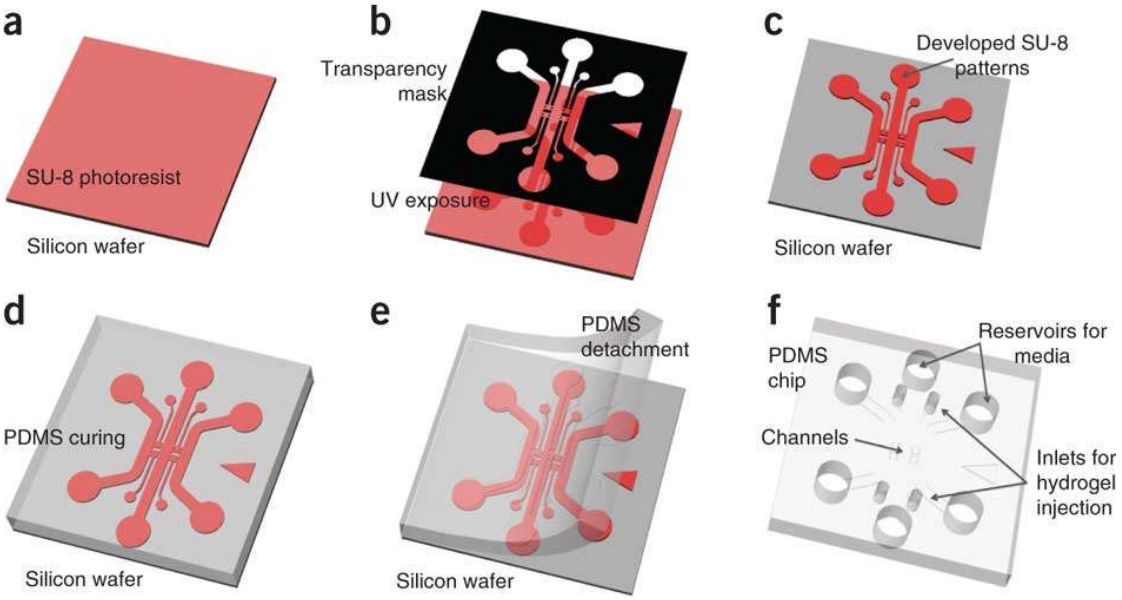

Figure 2.3: Schematic of fabrication process for microfluidic devices using photolithography and soft lithography. (a) SU-8 photoresist is spun onto a silicon wafer. (b) UV light is exposed to the photoresist through a photomask or transparency to transfer the pattern. (c) Uncrosslinked photoresist is removed using photoresist developer. (d) PDMS is poured and cured on the mold. (e) The PDMS is cut and detached from the mold. (f) Inlet and outlet holes are punched, and the channel is covalently bonded to a flat sheet of PDMS or glass using oxygen plasma. Image taken from [8]

To create a sealed microfluidic channel, the PDMS replica of the master is bonded to a flat substrate (typically glass or PDMS). PDMS will reversibly bond to PDMS and glass due to Van der Waals interactions, but irreversible covalent bonding is often required for the pressure induced perfusion of solutions through the channels. Covalent bonding is achieved by activating each surface through oxidation in an oxygen plasma cleaner or by corona treatment, and placing the two activated surfaces together. Bonding can be further enhanced by placing the bonded device on a hot plate at 80 C for 10 minutes. Microfluidic channels can then be perfused via gravity driven flow, a syringe pump, or pressure driven flow (Figure 2.4). A four-inch silicon wafer can thus be patterned with tens of microfluidic devices, and poured with PDMS hundreds of times without significant loss in feature resolution.

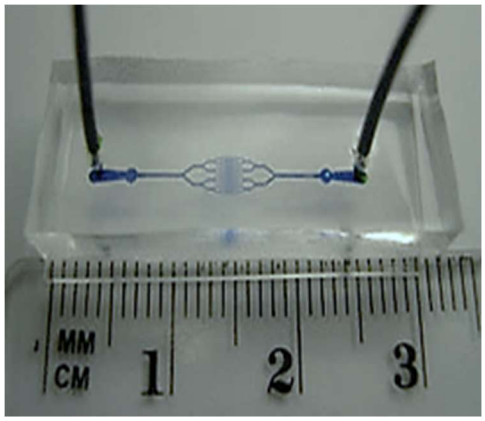

Figure 2.4. Bonded microfluidic device. Microfluidic channels bonded to a PDMS backing and perfused with an aqueous solution through tubing in inlet and outlet ports. Image taken from [9]

2.2.2 Electron Beam Lithography (EBL)

While complex microfluidic geometries can be achieved using standard photolithography, there are significant losses in precision and resolution when using contact photolithography to fabricate microfluidic structures at the single micron scale. To

recapitulate the biophysical environment of cells, namely the matrices that blood cells interact with, robust, single micron geometries are required. Electron beam lithography (EBL) utilizes an electron beam to transfer a CAD pattern to a silicon wafer, and can be employed to achieve sub-micron feature dimensions. EBL can be used in a projection modality, in direct writing, and as a method for material deposition. Direct writing allows for 10 nm resolution, [9] though its pixel by pixel etching requires long write times using expensive clean room equipment, and is thus best suited for creating a limited number of small features. To that end we used direct writing in this work to create arrays of fine features that single cells interact with. As in photolithography, the electron beam patterns a photoresist, in this EBL process, however, the wafer is further processed to transfer the features to the silicon wafer itself.

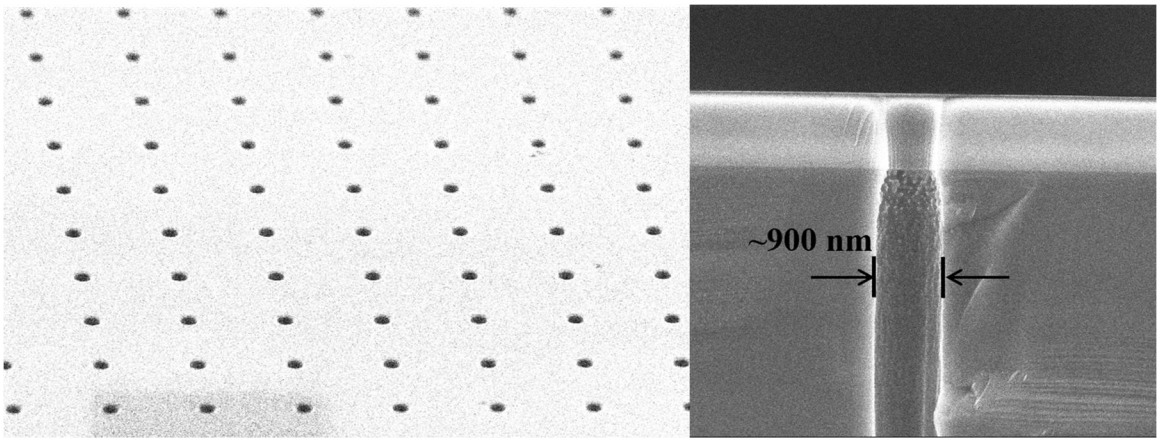

Figure 2.5. SEM of EBL features. Surface of silicon wafer etched with 900 nm holes to a depth of 3 μm (left). Cross section of holes created via EBL, notable for their smooth side walls. The top (slightly thinner) layer is the hardmask which is removed during processing (right).

EBL has been incorporated into the process flow for creating microfluidic devices in a number of ways, including the direct patterning of PDMS, the creation of a silicon master from which a PDMS master can be made for PDMS to PDMS replica molding, and the

creation of a silicon master that can be used for soft lithography.[10, 11] In this work, the goal is to create a silicon mold that is directly compatible with soft lithography, so we aimed to create a master in which PDMS could be repeatedly cast and released without loss of feature quality. To readily release an elastomeric material, the side walls of the silicon mold must be smooth (Figure 2.5). Once a smooth- walled silicon master is made, the master can be treated with HMDS to enhance PDMS release. Soft lithography then proceeds as previously described. To create a closed microfluidic device, channels created with photolithography can be bonded atop the EBL-patterned features (Figure 2.6). This combination of fabrication techniques combines the small feature resolution of EBL with the less costly use of photolithography for traditional, large features.

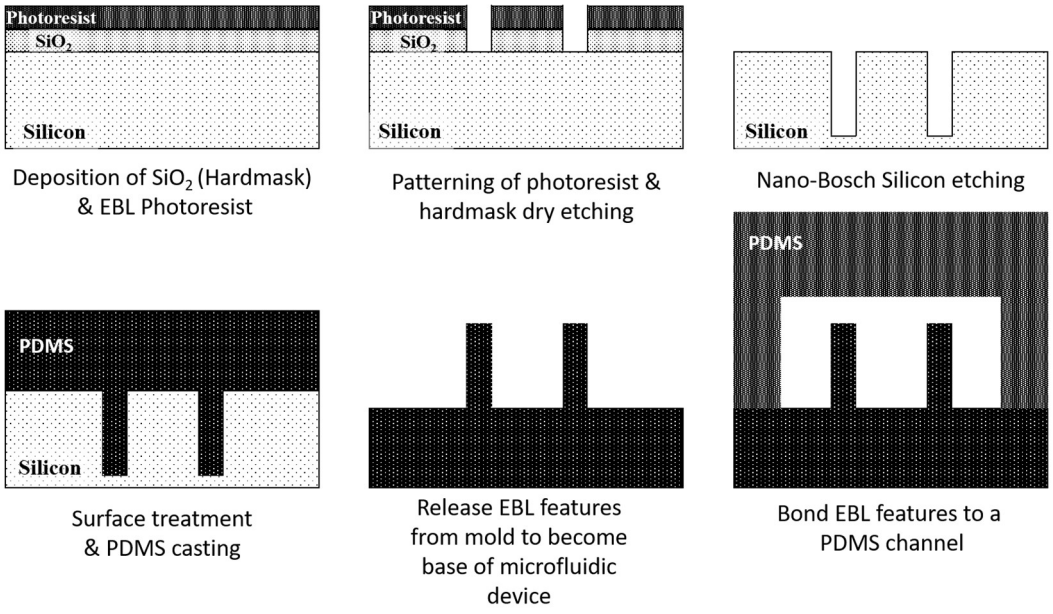

Figure 2.6. Process flow for combining EBL with soft lithography to create enclosed microfluidic devices with micron-sized features. To create an EBL patterned silicon wafer that is compatible with soft lithography, SiO_2 is first deposited on the wafer surface as a hard mask, followed by spin coating of an EBL photoresist. The photoresist is then patterned via an EBL photolithography tool and the hardmask is dry etched. The silicon wafer is etched through an optimized Nano-Bosch process. The patterned silicon wafer is

then treated with HMDS and poured with PDMS. The resulting PDMS structures are bonded to a microfluidic channel to create an enclosed device.

2.3 Tools for mechanical response of single cells

The response of cells to force and mechanical stimulus has been studied using a number of different technologies. Methods such as micropipette aspiration, atomic force microscopy (AFM), and optical tweezers, have been used to probe mechanical properties of cells, including stiffness and visco-elastic deformation.[12] Recently, groups have also used microfluidic devices to measure mechanical properties in a high throughput manner, as well as to leverage differences in cell deformability to physically sort cells and create diagnostic platforms.[13-15]

Micropipette aspiration can be used to apply a wide range of forces and pressures to cells, and their response can be monitored via microscopy. Typically, micropipette aspiration applies suction to a cell, and extension of the membrane into the pipettor is correlated to the applied pressure. This information is then generally fed into a continuum model, where mechanical properties are the read out. Micropipette aspiration can thus be used to study the visco-elastic properties of the cell membrane, or the whole cell itself.[16] While micropipette aspiration can be used to measure a range of mechanical properties, optical tweezers or optical traps are used to measure forces in the piconewton range, such as bond strength. Optical traps employ a highly focused laser beam to hold and manipulate dielectric particles; the intensity gradient of the laser physically holds the particle at its center.[17] Force application causes displacement of the particle from the beam center, and at small displacements, the restoring force of the beam can be modeled as a Hookean spring. By attaching a dielectric bead to the object of interest (DNA, cell, etc), trapping the

bead in the beam, and manipulating the bead position, mechanical quantities such as elasticity and bond force can be measured from subnanometer deflections.[18] Finally, AFM can be used to physically probe the cell surface by bringing a cantilever of known spring constant into contact with a substrate. The subsequent deflection of the cantilever is related to force. AFM has thus been used to measure elasticity and stiffness of various cell components under varied environmental conditions.[19, 20]

While AFM and optical tweezers provide precise measures of nano-scale forces and micropipette aspiration provides global understanding of cell mechanics, the measurement of individual events using these tools are time intensive and suffer from low throughput. Researchers have thus turned to microfabrication to increase measurement throughput. In the simplest form, transit time and geometry through a microchannel—as measured by impedance, high speed imaging, etc—can give insights into viscoelastic parameters of the cell as well as stiffness and deformability. Manipulating fluids at the microchannel scale by inertial focusing and sheath flow can further improve high throughput sorting of cells based on their deformabilities. [21-23]

2.3.1 Red Blood Cell Deformation

The mechanical properties of RBCs have been extensively studied, in part because they lack a nucleus and have relatively few cytoskeletal proteins, and therefore serve as an idealized, "simple" cell whose fundamentals can be applied to more complex cells.[24] More importantly, the hallmark of RBCs is their ability to elastically deform through capillaries that have a diameter smaller than that of the RBCs themselves. These significant deformations do not affect a RBC's ability to transport oxygen, nor do they damage healthy cells in any appreciable ways (as evidenced by RBC's 120 day lifespan in circulation).

Many pathologies affecting RBCs (malaria, sickle cell anemia, etc) directly affect the deformability of RBCs. There is thus significant importance in understanding the deformation mechanics of RBCs and the consequences of pathological changes on RBC mechanics. Many efforts in the realm of RBC mechanics aim to leverage differences in deformability toward the use in disease diagnostics.

Micropipette aspiration has been historically used both to study the mechanical properties of the RBC membrane and the properties of the cell itself. [25] RBC mechanics can also be studied by subjecting RBCs to shear flow. Further, due to the relatively heterogenous nature of RBC populations, microchannel based analysis of RBCs are feasible. There are many experimental studies related to flowing RBCs through a constriction to measure aspects of their deformability, such as their cortical tension or transit time.[26-28] Likewise, many computational studies describe the mechanical properties of RBCs as well as the extensive shape changes that RBCs are likely to undergo *in vivo*.[29, 30]

More recently, studies describe the action of the spleen as a mechanical filter for RBCs by creating microdevices and utilizing a bead based filtration system.[31-35] The spleen is considered to be the most physically challenging deformation (1 μm width x 2 μm height x 4 μm length) that RBCs undergo if there are no other underlying pathologies. If cells are not able to deform through the interendothelial slits in the spleen, they are removed from circulation. Sequestration of RBCs by the spleen in the case of malaria infected RBCs could have negative health outcomes, so a better understanding of a RBCs ability to deform in the spleen is warranted. Computational findings suggest that the most significant

determiner of RBC deformability is not the stiffness, but rather the surface area to volume ratio.

Many microfluidic systems now exist to gauge red blood cell deformability. Some are aimed at gaining a more global understanding of deformation mechanics, including the shape changes that RBCs undergo throughout the deformation processes. Others seek to leverage microfluidics for clinical purposes: for instance, a filter to be used in transfusion medicine that would remove older, less deformable RBCs. Elastic fatigue was also recently studied to show that repeated passage through a constriction reduces the cell's future deformability. The authors aim to correlate this fatigue to different disease states.[36] A recent set of studies also sought to understand the relationship between relaxation time and time exposed to a force (or time in a constricted state), and it was found that there is a critical load time of T~ 180 s at which the relaxation time was significantly extended from 0.1 s to 10 s. [37, 38]

While the wealth of knowledge garnered by these studies gives significant insight into deformation (and sometimes hemolysis), there is still a complete lack of knowledge as to the mechanism or real-time biophysical parameter space of RBC fragmentation (the breaking of RBCs into two disparate cell fragments) and its temporal requirements (outside of shear induced hemolysis). Typically, the presence of RBC fragments is mentioned in publications as an aside, such as when RBCs were passed through a long filter with small pore size.[35] Understanding this process is important as RBC fragmentation is a hallmark of a number of diseases and also of device implants. The morphological abnormalities that are seen on clinical blood smears are described below.

2.3.1.1 RBC Morphological Abnormalities

Mature red blood cells are anuclear, featuring a lipid bilayer traversed by transmembrane proteins (primarily glycophorins and protein 3) bound to a complexly networked spectrin cytoskeleton. RBCs are typically disciform in shape with an average diameter of 7.5 μm. When visualized by traditional pathology stains, RBCs exhibit a light central region (central pallor) one third the cell size. Various morphological abnormalities result from pathological states that alter the RBC membrane or cytoskeleton and/or from mechanical damage to the cells (Figure 2.7). Typical RBCs are described as normocytic (of normal size) and normochromic (of normal coloring, and thus normal haemoglobin content). Morphological abnormalities are then described via peripheral blood smears based on: size of central pallor; increase or decrease in cell size; and alterations in shape (e.g., spherical, fragmented, and spiculated).[39] Clinical diagnoses and treatment courses are based on the presence of these abnormalities, and thus a brief description of the morphologies related to mechanical disruption, is warranted:

- Tear drop cells (dacrocytes) are shaped as named and are primarily linked to bone marrow fibrosis, in which there is increased deposition of reticulin and collagen fibers. It has been posited that these cells form either when released from the abnormal bone marrow matrix or that the newly formed RBCs are fragile and are damaged in the spleen.[40]

- Spiculated cells describe various abnormal RBCs that are characterized by a lack of roundness and the presence of spicules of different size and number. The short, blunt spicules that characterize echinocytes (also referred to as burr cells) often result from electrochemical interactions and ATP depletion; this damage is

generally reversible upon reestablishing a favorable chemical environment. Acanthocytes display large, irregular spicules and are indicative of many inherited and acquired diseases that increase the ratio of cholesterol to phospholipids. Of note are keratocytes and schistocytes, these cell fragments are characterized by irregular edges and are indicative of mechanical damage caused by microangiopathies—diseases that cause clotting in the microcirculation.

- Spherocytes and microspherocytes are indicative of an alteration in the surface area to volume ratio of the RBC that causes them to assume a spherical shape. They are identified on blood smears by lack of central pallor and a reduced diameter. Spherocytes can result from pathologies that alter the cell membrane or cytoskeleton, or can be a byproduct of schistocyte formation.

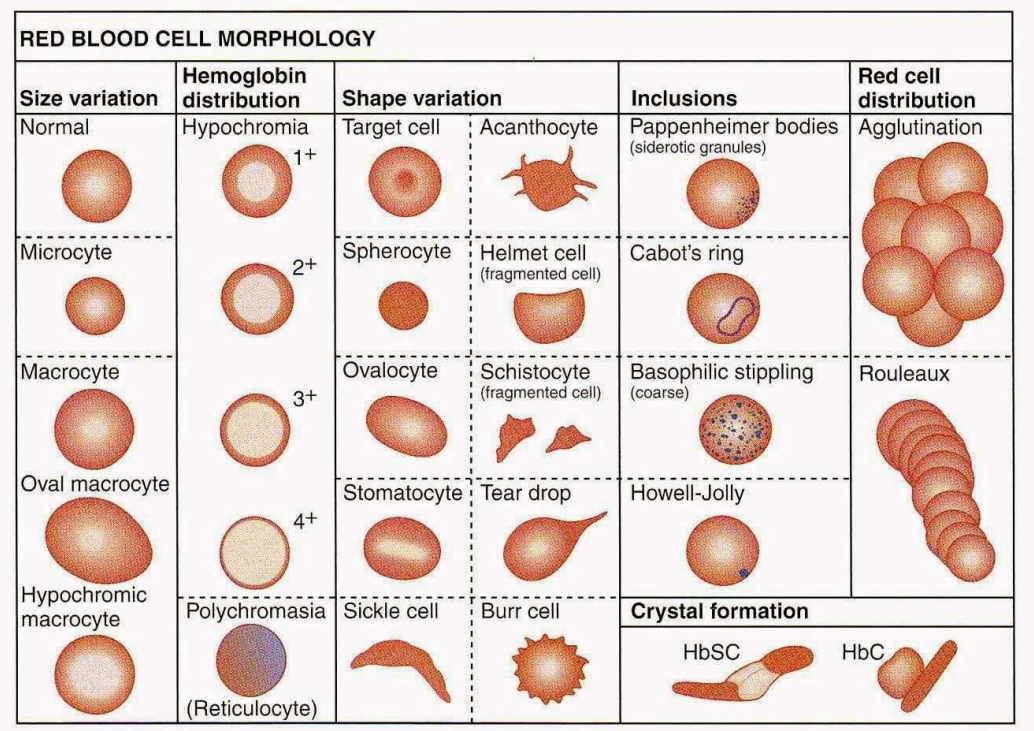

Figure 2.7 Chart of RBC morphological abnormalities. Pathologists categorize abnormal RBC morphology based on size variation, hemoglobin distribution, and shape variation. Spherocytes, helmet cells, schistocytes, tear drop cells, and burr cells are all thought to arise from mechanical damage to RBCs. Image taken from [41]

CHAPTER 3: RESOLVING THE MECHANISM OF THE FERRIC CHLORIDE THROMBOSIS MODEL

3.1 Introduction and Background

In the most commonly used animal model for studying thrombosis (the ferric chloride ($FeCl_3$)-induced thrombosis model), $FeCl_3$ is applied to the adventitia of a mouse blood vessel, and the resulting occlusive clotting is monitored by Doppler flow measurements and/or intravital microscopy.[42-46] This injury model has been used extensively to test the efficacy of therapeutics and to determine the relevant receptor/ ligand interactions for clot initiation and propagation.[47, 48] However, there are discrepancies in literature findings that stem, in part, from the various $FeCl_3$ concentrations used and differences in the vessels to which $FeCl_3$ is applied (see Table 3.1 for percent solution to concentration for anyhydrous and hexahydrate $FeCl_3$). To explain these discrepancies, it has been posited that different ligand/ receptor interactions are involved in vessels with different shear environments. While this may be valid, the concentration dependent nature of the $FeCl_3$ model implicates a role for mass transfer in the system.

Clot initiation in this model is historically attributed to free iron-induced denudation of endothelial cells and the subsequent exposure of the subendothelium that triggers platelet adhesion/aggregation and activation of the coagulation cascade.[48] However, studies using mice deficient in collagen receptor glycoprotein VI have produced contradictory results, reporting both normal and altered thrombus formation.[49, 50] Eckly et al. observed that although endothelial cells appear denuded and platelets are present in the occlusive thrombus, there is limited collagen exposure in the vessel.[51] Further, an elegantly designed SEM analysis revealed that endothelial cells are not denuded, and surprisingly,

that erythrocytes mediate the adherence of platelets to the endothelium by an unknown mechanism.[52] In addition to the uncertain status of the endothelium, the effects of $FeCl_3$ vary based on the vessel to which it is applied: in mice lacking the extracellular domain of GPIbα, the $FeCl_3$ model results in occlusion in mesenteric venules but not in the carotid artery.[49, 53] These inconsistencies, in conjunction with the wide range of published $FeCl_3$ concentrations (10 mM to 2 M) and application times (1-20 min) used to elicit a clotting response, raise questions about the direct chemical effects of $FeCl_3$ on blood components and the role that mass transfer plays in this thrombosis model.[54]

Table 3.1. Percent solution (w/v) of $FeCl_3$ in terms of concentration (M**).**
In the literature, ferric chloride amount is expressed in terms of percent solution, but as both anhydrous ferric chloride (162.2 g/mol) and ferric chloride hexahydrate (270.3 g/mol) are used, concentration must be specified in molarity for consistency and comparability. The molarity of the solution as related to percent solution is shown for each ferric chloride species.

Percent Solution (w/v)	Anhydrous $FeCl_3$ Concentration (M)	$FeCl_3$ Hexahydrate Concentration (M)
0.5	0.031	0.018
1	0.062	0.037
5	0.308	0.185
10	0.617	0.370
20	1.233	0.740

Microfluidic devices allow for spatiotemporal control over the introduction of a precise chemical concentration in defined shear environments. This control then allows for the role of mass transfer in this injury model to be elucidated, a feat not readily achievable *in vivo*. Furthermore, an *in vitro* system allows for piecewise introduction of blood components into the system to determine the role that each part of the complex blood environment plays in the ferric chloride thrombosis model. Discrepancies in the literature and the extensive use of the $FeCl_3$ model makes understanding its mechanism of utmost importance to hematological research. Resolving the mechanism of action and

understanding the role of mass transfer in the injury model using microfluidics not only reconciles inconsistencies in the literature, but informs researchers as to the appropriate uses of the injury model in the future.

3.2 Materials and Methods

3.2.1 Experimental Reagents

Human blood was collected according to IRB-approved protocols per the Declaration of Helsinki into sodium citrate (BD). Blood was separated into its individual components by centrifugation: washed RBCs were obtained by centrifugation of whole blood at 300g for 10 min (followed by 3x PBS wash), PRP was obtained by centrifugation at 150g for 10 minutes with no brake or acceleration, and PPP and platelets were obtained by centrifugation of PRP at 900g for 5 minutes with no brake or acceleration. To study whole blood, RBCs were diluted in PRP to 12.5% to allow for improved microscopy and visualization of clot components. To recalcify blood, $CaCl_2$ (Sigma) was added to a final concentration of 0.01 M directly prior to every experiment, unless otherwise noted. Where appropriate, blood samples were incubated for ~5 minutes with Alexa-Fluor-568 conjugated fibrinogen at 10% v/v, mouse anti-human CD41, M148 (Abcam, Cambridge, UK) at 1:400, and AlexaFluor-488 goat-anti-mouse IgG at 1:400 (Life Technologies, Carlsbad, CA). Human umbilical vein endothelial cells (HUVEC, Lonza, Walkersville, MD) were stained with Hoescht 33342 (Life Technologies) prior to experiments. Live/dead assay was performed with calcein and propidium iodide in serum-free EGM-2 media (Lonza). PBS with calcium and magnesium pH 6.5 was used to dilute anhydrous iron(III)-chloride (Sigma), aluminum (III) chloride (Sigma), and chromium (III) chloride (Sigma) to the desired concentration on the same day as the experiment.

3.2.2 Microfluidic Parameters

To recapitulate the endothelium-blood-$FeCl_3$ interface, a polydimethylsiloxane (PDMS) based T-shaped microfluidic was designed with a 250 mm width main channel, 50 mm width side channel, and overall device height of 50 mm. Device mold was fabricated via traditional photolithography and devices were made via traditional soft lithography. Devices were bonded after exposure to oxygen plasma. To obtain desired flow profile, two Harvard Apparatus pumps were used to infuse fluid at 2.7 μL/ min in the main channel and 0.4 μL/min in the small channel, giving a shear rate of ~ 4 dyne/cm^2 at the interfacial region in the main channel. Non-endothelialized devices were blocked with 3% BSA for 1 hour prior to experiments. When appropriate channels were seeded with HUVEC cells and cultured in EGM-2 media (Lonza), as previously described.[9]

3.2.3 Flocculation Experiments

To visualize blood cell aggregation, 5 μm of the blood component of interest was pipetted on a glass cover slip, 5 μm of $FeCl_3$ at a given concentration (from 5 μM to 1 M) was pipetted on top of the blood, a top cover slip was placed on the sample, and microscopic analysis was immediately performed. To perform light scatter measurements, 250 μL of $FeCl_3$, $AlCl_3$, or $CrCl_3$ at various concentrations was added to 250 μL of blood components in fluorimeter cuvettes (Sigma). Light scatter was measured for 60 seconds at 600 nm by a PTI Fluorescence System Fluorimeter immediately after chemical addition.

3.2.4 Drug treatments and mouse experiments

Blood and endothelialized devices were incubated with drug treatments for 30 minutes prior to experiment. Aspirin (Sigma) was used at 1 mg/mL, heparin (APP Pharmaceuticals, LLC, Schaumburg, IL) at 1 UN/mL, hirudin (Sigma) at 1 UN/mL, and eptifibatide (COR Therapeutics, San Francisco) at 10 μM. vWF deficient blood was created by adding healthy donor washed platelets and washed red blood cells to vWF severe trait 3 plasma (George King Biomedical, Inc., Overland Park, Kansas). C57BL/6 mice (Jackson Laboratory) were used for all wild-type controls, and IL4-R/Iba (glycoprotein Ib-α–deficient) [55] were provided by Jerry Ware. Mouse cardiac punctures were performed following IACUC approved protocols, and mice were approximately 8 weeks old at the time of experiment.

To analyze differences in occlusion, we performed a two-tailed, unpaired (student's) T-test for equality of means between treated blood and control blood with a confidence interval of 95% (values are significantly different when $p<0.05$). Tests were performed between treated blood at a given concentration and untreated blood at that same concentration (control blood with 50 mM $FeCl_3$ vs. aspirin-treated blood with 50 mM $FeCl_3$).

3.2.5 Computational Fluid Dynamics Modeling

I used COMSOL Multiphysics, version 4.4, to simulate simple blood flow in a vessel. I modeled the blood vessel as 2D and used the "laminar flow package" to simulate an incompressible fluid with water-like properties (similar viscosity and density). My model included three domains: an upstream region (1 mm in the y-direction), the ferric chloride patch region (1 mm in the y-direction), and a downstream region (1 cm in the y-direction). For each vessel type, I used the diameter and velocity from the literature and specified a

no-slip boundary condition at the walls. I simulated the diffusion of ferric chloride using the "transport of diluted species package" which solves the convection-diffusion equation. The initial value of ferric chloride was set to 0 throughout the three domains as well as at the inflow boundary. At the upper boundary of the ferric chloride patch region, the concentration of ferric chloride was set to 50 mM (the previously calculated luminal concentration). The diffusion coefficient was set to 6.0 x 10^{-10} m^2/s. I ran the simulation to visualize the diffusion of ferric chloride in the vessels (solution time 16-20 s). I set a manual data range in the plot options of 0.5 mM to 50 mM, to present the concentrations at which ferric chloride induces blood aggregation. Shear stress was also modeled in the vessel to be approximately 4 dyn/cm^2 at the interfacial region.

3.3 Results and Discussions

3.3.1 Creation of an In Vitro Endothelial Cell/ Blood Cell/ Ferric Chloride Interface

Traditional photolithography and soft lithography were used to create a T-junction microfluidic device that would allow for spatiotemporal control of the introduction of $FeCl_3$ through a side channel to interface with blood components perfused through a main channel (Figure 3.1). This system allows for the two species to interface near the wall, as they would in the convection dominated environment of blood vessels. As previously developed in the Lam engineering and hematology laboratory, the main channel can also be seeded with endothelial cells to a confluent monolayer that further recreates the multifaceted *in vivo* environment.[9, 56] With this addition, sundry combinations of biological factors can be introduced to the system to elucidate the effects of $FeCl_3$ on each component of the vessel environment.

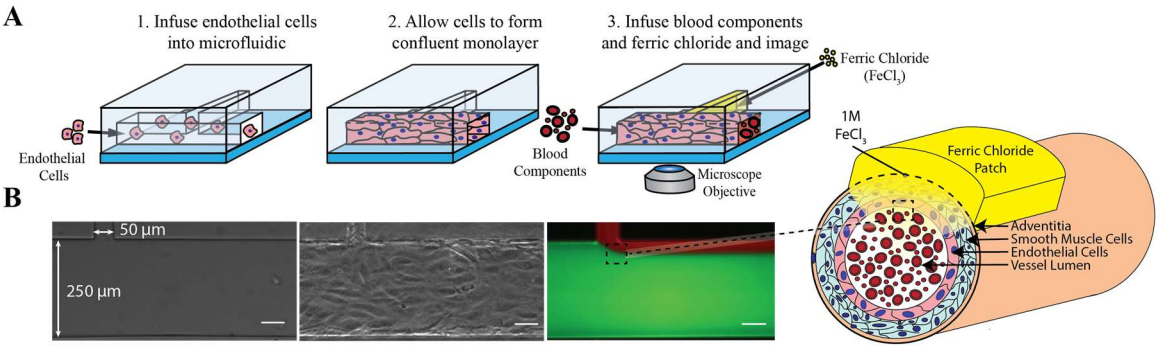

Figure 3.1. T-junction microfluidic recapitulates the $FeCl_3$ interface. A) "Endothelial"-ization of the main channel of T-junction microfluidic results in a blood cell/ ferric chloride/ endothelial cell interface that can be visually monitored via wide field fluorescence microscopy. B) Microscope images of the bare channel (left), an endothelialized channel (center), and the interface of the fluid streams from each inlet (right). The interface is depicted by a cartoon of the model system: $FeCl_3$ patch is applied to the adventitia of a blood vessel. $FeCl_3$ diffuses through the vessel wall and into the lumen. Scale bars are 50 µm.

The main channel is 250 µm wide and 50 µm in height and perfused at 2.7 µL/min, while the side channel is 50 µm wide and 50 µm in height and is perfused at 0.4 µL/min; resulting in a shear stress of ~4 dynes/cm^2 at the interface, as modeled by computational fluid dynamics (Figure 3.2).

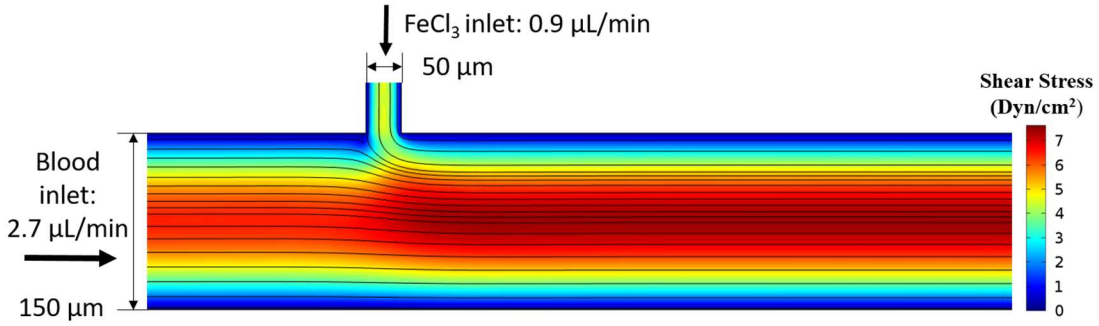

Figure 3.2. Shear Stress in T-junction Fluidic. A COMSOL model of shear stress and streamlines in the designed T-junction microfluidic shows the experimentally verified fluid interface with a shear stress of ~4 dyn/cm^2 in the interfacial region.

3.3.2 Calculation of Relevant $FeCl_3$ Concentration for Microfluidic Influx

A saturated 1 M $FeCl_3$ patch is applied to the adventitial side of the mouse carotid artery to induce robust thrombus formation. This concentration, however, is not the concentration of interest for the microfluidic system; the concentration needed for *in vitro* studies is that at the vessel lumen where the $FeCl_3$ interfaces with the endothelial cells and blood. To obviate complex modeling of $FeCl_3$ diffusion through the multilayered vessels, the bulk *in vivo* $FeCl_3$ concentration was measured downstream of the patch. The left carotid artery of a mouse was exposed by dissection, and injured by topical application of filter paper saturated with 1 M (20% anhydrous) $FeCl_3$—for 2, 5, or 10 minutes. The adventitia of the artery was then rinsed with saline to halt $FeCl_3$ influx, and 400 µL of blood was drawn downstream of the patch and iron content was measured. To account for measurement error due to iron binding to blood components, the assay was performed with a known amount of $FeCl_3$ in buffer and in plasma, absorbance measurements were obtained, and a correction factor of 10 between the solutions was found. The downstream iron concentration was found to be 160 µM or 9 µg/mL. Steady-state $FeCl_3$ flux into the vessel was reached by 5 minutes and maintained at 10 minutes; the input concentration is thus assumed to be constant over the relevant time scales (Figure 3.3).

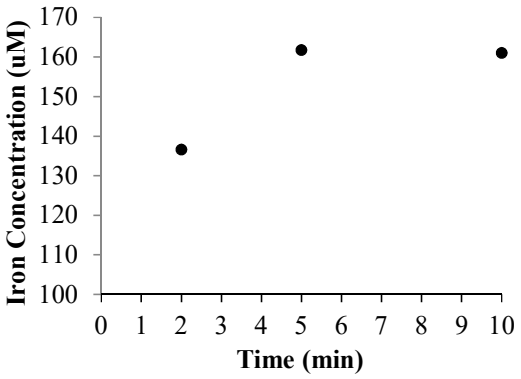

Figure 3.3. In vivo ferric concentration downstream of $FeCl_3$ patch. 1 M $FeCl_3$ patch is applied to carotid artery for 2, 5, and 10 minutes, and the downstream iron concentration is measured. Steady-state downstream concentration is found to be ~160 μM.

Fick's laws of diffusion in a convection dominated system were used to find the endothelial wall concentration. Given the high shear rates and the approximately linear velocity profile near the wall, it was assumed that the contact time of the blood with the patch area is short and a short-contact-time solution of the Navier Stokes equation can be used. The solution for the flux of the solute into the blood along the wall where the patch is located is then:

$$N_{i_y}(y=0) = 0.6783 D C_0 \left(\frac{2V_z}{RDz}\right)^{1/3}; \quad (1)$$

where D= 6 x 10^{-5} ± 1 x 10^{-5} cm^2 /s is the diffusion coefficient of $FeCl_3$ in blood [57], R=250 ± 25 μm is the vessel radius [58, 59], Vz = 20 ± 2 cm/s is the average blood velocity [60, 61], and z= 1 cm is the axial distance from the leading edge of the patch. This approximation is reasonable when

$$\frac{zD}{2\langle v\rangle R^2} < 0.01, \quad (2)$$

or when convection dominates over diffusion.[62] Integrating the equation for flux across the area of the patch gives the total solute flux into the blood vessel, which (assuming there is no uptake of solute along the vessel) must equal the experimentally calculated solute flux downstream. The initial concentration at the vessel wall, and the relevant concentration for the *in vitro* input, is then $C_0 \sim 50$ mM $FeCl_3$ (Figure 3.4).

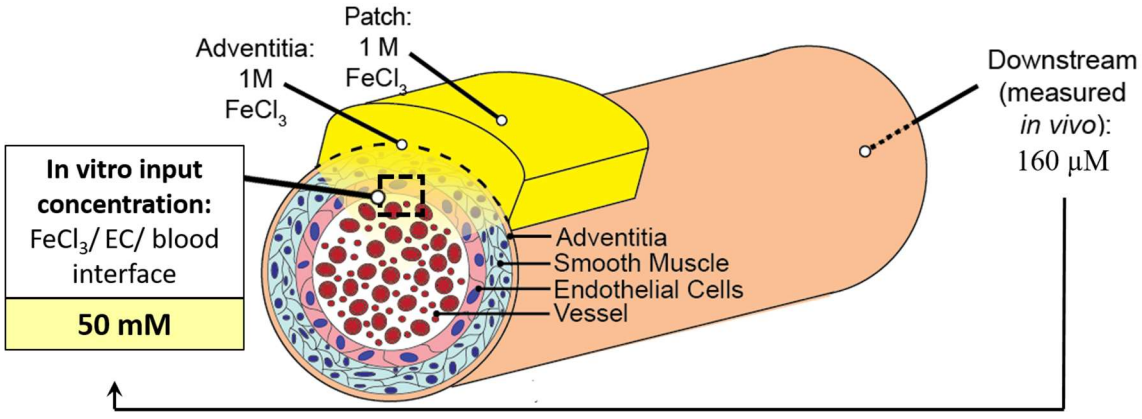

Figure 3.4. Relevant system concentrations. By measuring the *in vivo* iron concentration downstream of the $FeCl_3$ patch, the luminal wall concentration—that at the interface of the blood and endothelial cells—can be found via Fick's Laws of Diffusion. The $FeCl_3$ concentration at the interface is approximately 50 mM when a 1 M patch is applied.

3.3.3 Effects of $FeCl_3$ on the In Vitro "Vasculature"

The endothelialized T-junction from Section 3.2 aptly recreates the *in vivo* effects of the $FeCl_3$ injury model: whole blood exposed to 50 mM $FeCl_3$ results in a channel occluding aggregate without endothelial cell denudation (Figure 3.5). In agreement with the findings of Barr et al, RBCs appear to be a significant component of the aggregate.[52] This is surprising as RBCs are not thought to be directly involved in the biochemically regulated clotting cascade. Interestingly, $FeCl_3$ leads to aggregation of all individual blood components: washed RBCs, platelet rich plasma (PRP), platelet poor plasma (PPP),

and platelets (Figure 3.5). $FeCl_3$ even leads to the aggregations of bovine serum albumin (BSA), a protein uninvolved in clotting (Figure 3.6).

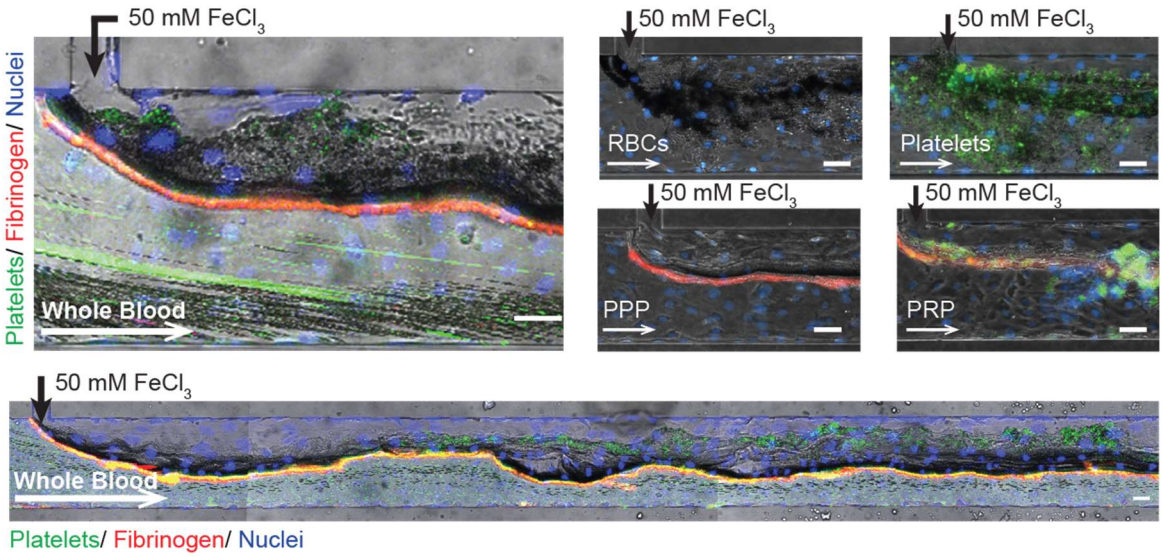

Figure 3.5. Blood components aggregate in the presence of $FeCl_3$ in endothelialized microfluidic channel. When whole blood, red blood cells, platelets, plalelet poor plasma (PPP), and platelet rich plasma (PRP) are exposed to 50 mM $FeCl_3$ they form channel occluding aggregates. Scale bars are 50 μm.

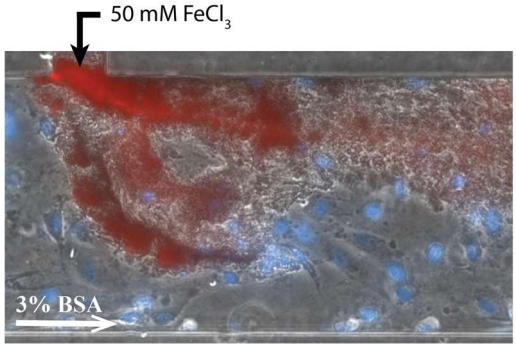

Figure 3.6. BSA aggregates when exposed to $FeCl_3$**.** 3% BSA forms aggregates when exposed to 50 mM $FeCl_3$ in endothelialized microfluidic.

While the endothelial cells remain adherent to the microfluidic channel surface, $FeCl_3$ exposure causes localized dose-dependent cell death (Figure 3.7).

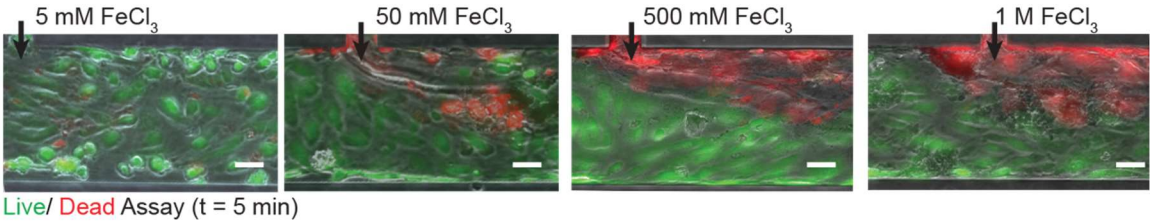

Figure 3.7. Dose-dependent $FeCl_3$-induced endothelial cell death**.** Endothelial cell viability is dependent on the concentration of $FeCl_3$ that cells are exposed to: higher input concentrations result in localized cell death, but not denudation. Panels from left to right show introduction of 5 mM, 50 mM, 500 mM, 1 M $FeCl_3$, respectively. Green/live: calcien; red/dead: propidium iodide. Scale bars represent 50 µm.

3.3.4 Effects of $FeCl_3$ on Blood in the Absence of Endothelial Cells

The aggregation of blood components that are outside of the traditional clotting cascade (RBCs and blood proteins) suggests that aggregation might not be initiated by endothelial cell injury. The *in vitro* system allows the physiochemical effect of $FeCl_3$ to be studied in the absence of endothelial cells, giving mechanistic insight that is not possible *in vivo.* Surprisingly, $FeCl_3$ causes aggregation of all blood components, in the absence of endothelial cells (Figure 3.8).

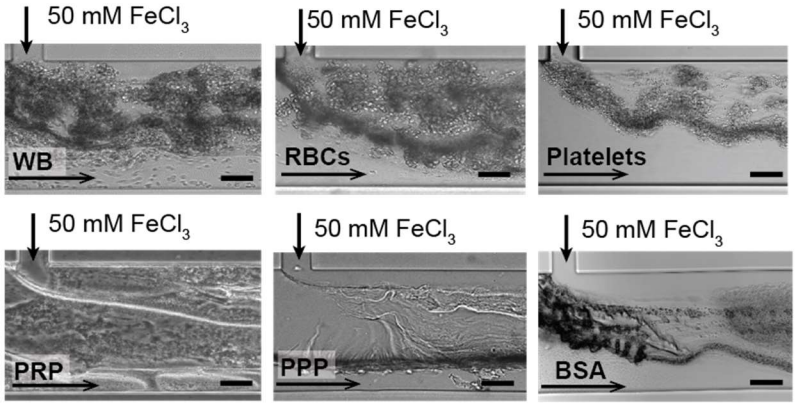

Figure 3.8. Blood aggregates in bare microfluidics. Representative images of blood component aggregates (whole blood, RBCs, platelets, PRP, PPP, BSA) in non-endothelialized microfluidics when exposed to 50 mM $FeCl_3$. The presence of sheet-like protein aggregates is clearly visible in PPP. All scale bars represent 50 µm.

Washed platelets and RBCs are slowest to aggregate, and the protein component of blood (PPP) forms sheet-like structures that appear to enhance aggregate initiation and stability when cells are present (PRP and WB). At 1 M $FeCl_3$, all blood components form a fully occlusive aggregate (Figure 3.9). The aggregation of all blood components in the absence of endothelial cells suggests that the mechanism of aggregate initiation is outside the traditional clotting cascade.

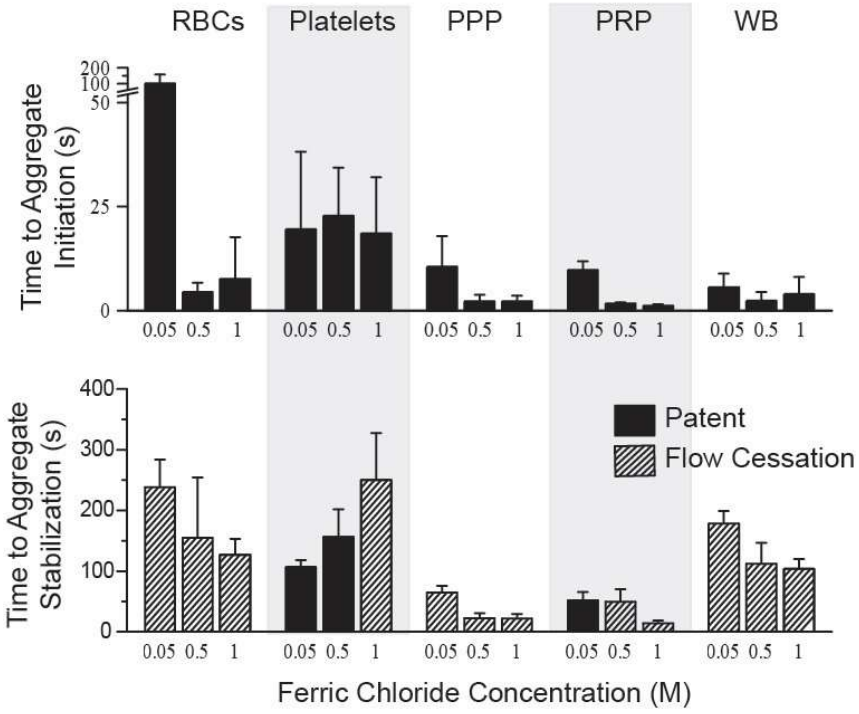

Figure 3.9. Time to aggregate initiation and stabilization in bare microfluidics. Aggregates of washed RBCs, washed platelets, PPP, PRP, and whole blood (WB) form in microfluidic channels at all concentrations ranging from 50 mM to 1 M. Time (in seconds) to initial adherence of blood components and stable aggregate formation (unchanging or complete occlusion) is shown, where complete channel occlusion is denoted by cross-hatched bars.

3.3.5 Proposed Mechanism of $FeCl_3$-induced Aggregate Initiation

As $FeCl_3$ causes aggregation of blood cells and proteins, both in the presence and absence of endothelial cells, a non-biological, charge-based mechanism of aggregation was proposed (Figure 3.10). Blood is a colloidal suspension of negatively charged cells and

proteins, and $FeCl_3$ is used in applications such as waste water treatment to destabilize colloidal suspensions by reducing the zeta potential of the particles, and causing them to aggregate.[63,64] In aqueous solutions $FeCl_3$ continuously hydrolyzes, polymerizes, and precipitates; the species exists primarily as Fe^{3+}, $Fe(OH)^{2+}$, and $Fe_2(OH)_2^{4+}$. [65,66] Fe^{3+} is a strong trivalent cation that can directly bind to negatively charged proteins (both cell bound and in solution), and lead to their destabilization and aggregation (termed flocculation in colloidal chemistry).[67] The cationic hydroxides, on the other hand, deposit on surfaces and create a large particular mesh that can bind negatively charged particles.[68] Together, these charge-based mechanisms cause the aggregation of colloids such as blood cells.

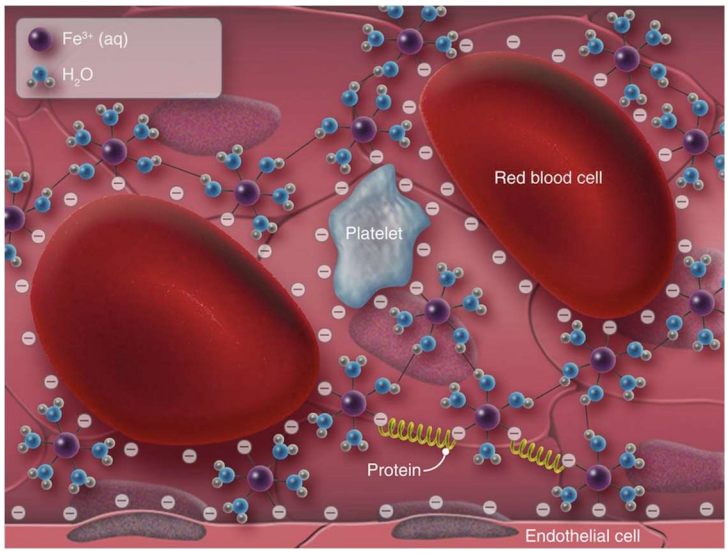

Figure 3.10. Charge-based aggregation of blood components**.** Cartoon representation of the action of Fe^{3+} as it interacts with negatively charged blood cells. "Ferric ions permeate through the endothelium into the lumen. These positively charged ions suppress the negative charge on blood cells, endothelial cells, and plasma proteins, which allows them to form agglomerates. This charge-based mechanism allows blood cells and proteins to accumulate on the vessel wall independent of hemostatic mechanisms." [69]

To test this charge-based hypothesis, another metal salt used in flocculation, $AlCl_3$, was introduced to the system. Al^{3+} has similar binding properties to Fe^{3+}, and in

support of my hypothesis, it too causes RBC aggregation in both bare and endothelialized channels. Further, $AlCl_3$ was recently shown to induce thrombosis *in vivo* when used in a similar manner to $FeCl_3$.[70] Alternatively, introduction of $CrCl_3$, a trivalent cation that is considered chemically inert because it preferentially binds water, does not cause blood cell aggregation.[63, 65, 71] $FeCl_3$, $AlCl_3$, and $CrCl_3$ all cause endothelial cell death likely due to their highly acidic nature, but as shown, they do not have similar aggregation capabilities, thus providing further evidence that cell death alone is not enough to initiate extensive aggregation (Figure 3.11).

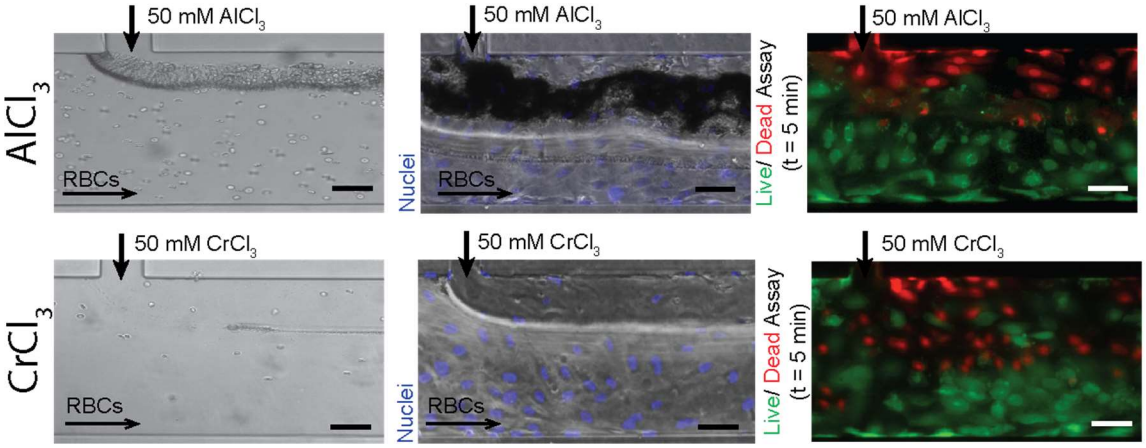

Figure 3.11. $AlCl_3$ causes RBC aggregation similar to $FeCl_3$. The introduction of $AlCl_3$ causes RBCs to aggregate at the fluidic interface in bare (left) and endothelialized (middle) microfluidics. $AlCl_3$ causes endothelial cell death, but the cells remain adherent (right). The introduction of $CrCl_3$ does not result in RBC aggregation in bare (left) or endothelialized (middle) microfluidics. $CrCl_3$ causes endothelial cell death, but the cells remain adherent (right) (green/live- calcien, red/dead- propidium iodide). All scale bars represent 50 μm. N=3.

$FeCl_3$-induced aggregation of blood cells and proteins also proceeds in static flocculation assays. Standard microscopy shows extensive aggregation of blood cells and proteins for concentrations of $FeCl_3$ greater than 0.5 mM, and FeOH precipitates are visible as mesh-like deposits at low $FeCl_3$ concentrations (the hydroxide species predominates in less acidic environments) (Figure 3.12).

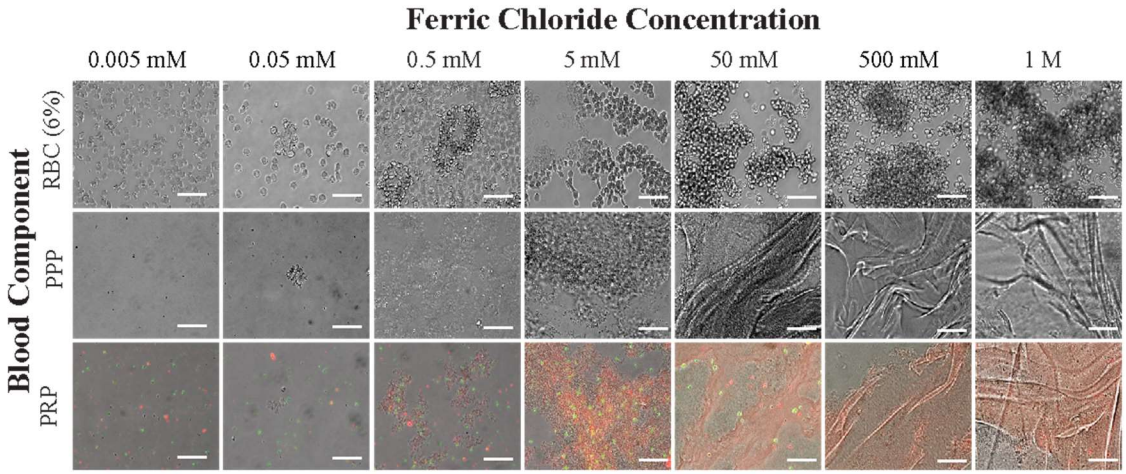

Figure 3.12. Microscope analysis of flocculation activity of $FeCl_3$. Static aggregation of blood components (RBCs, PPP, and PRP) increases in a concentration dependent manner from 0.005 mM to 1 M $FeCl_3$. At mid-range concentrations of $FeCl_3$, amorphous iron hydroxide precipitates are present. Sheets of protein are evident in concentrations greater than 5 mM. Platelets (green: CD41); fibrinogen (red). Scale bar = 50 µm, N=3.

Dynamic light scattering, as measured by a fluorimeter—where increased light scattering correlates to increased aggregate presence—show that $FeCl_3$ and $AlCl_3$ cause aggregation of PRP and PPP (Figure 3.13). At high concentrations, the addition of $FeCl_3$ and $AlCl_3$ results in a solid, macroscopic protein aggregate (Figure 3.14).

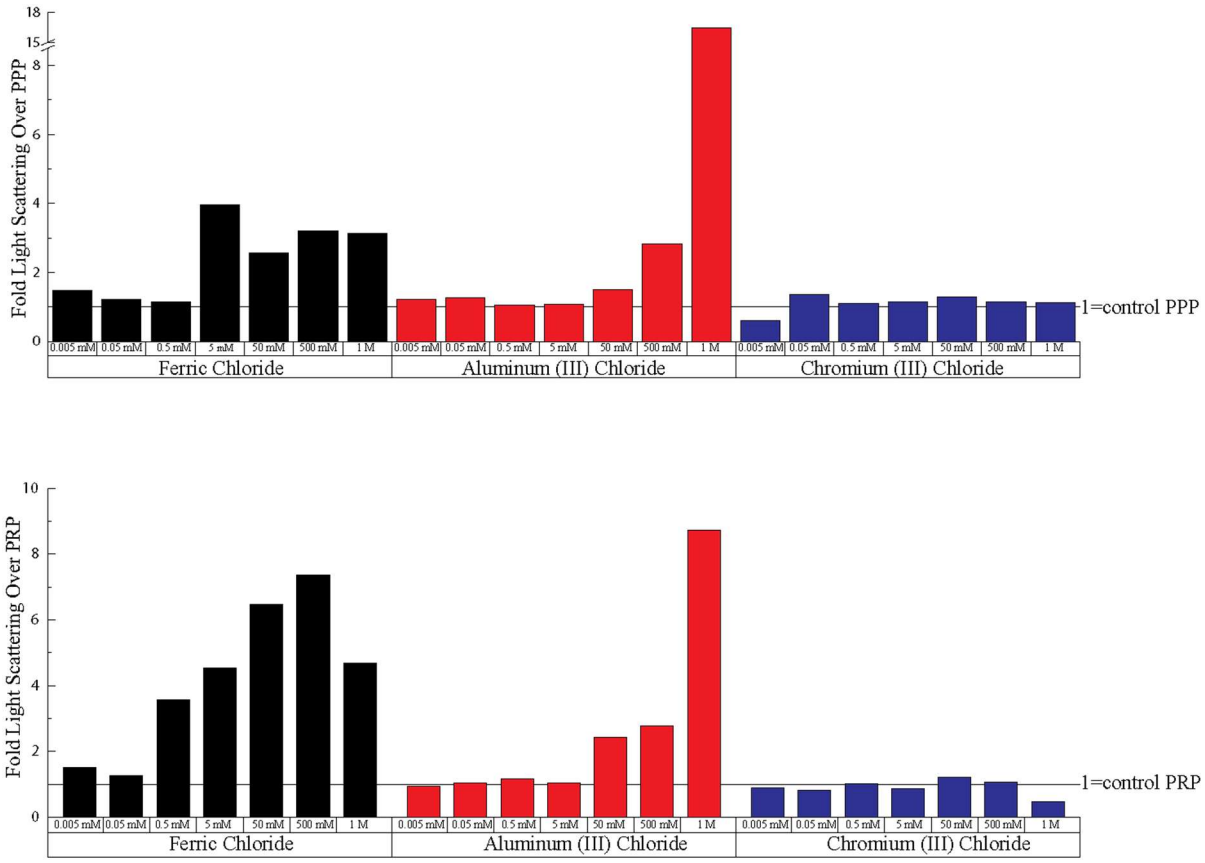

Figure 3.13. Light scattering of PRP and PPP when exposed to a range of $FeCl_3$, $AlCl_3$, and $CrCl_3$ concentrations. Values are expressed as fold increase over control PPP and PRP, where increased scatter corresponds to increased aggregation. All scale bars represent 50 μm; N = 3.

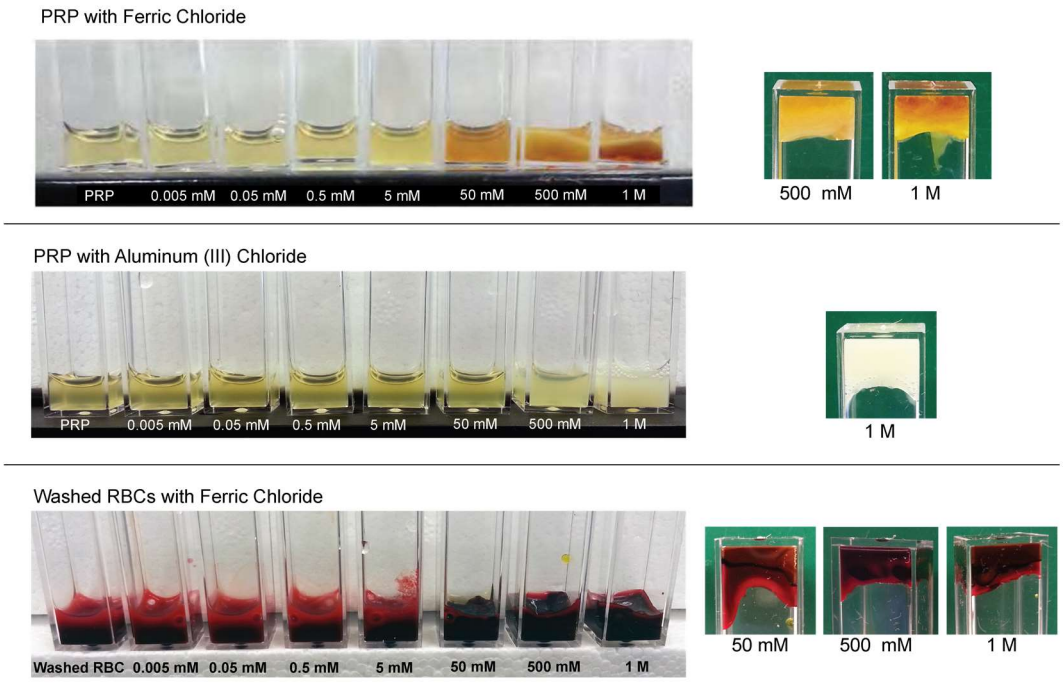

Figure 3.14. $FeCl_3$ and $AlCl_3$ –induced aggregation of blood components in microcuvettes. PRP is exposed to 0.005 mM to 1 M $FeCl_3$ (top). Aggregates are macroscopically visible at concentrations > 0.5 mM. PRP with both 500 mM and 1 M $FeCl_3$ forms a solid aggregate that is not disturbed upon microcuvette inversion. PRP is exposed to 0.005 mM to 1 M $AlCl_3$. Aggregates are macroscopically visible at concentrations > 50 mM. PRP with 1 M $AlCl_3$ forms a solid aggregate that is not disturbed upon microcuvette inversion (right). Washed RBCs are exposed to 0.005 mM to 1 M $FeCl_3$ (bottom). Aggregates are macroscopically visible at concentrations > 0.5 mM. Washed RBCs with 50 mM, 500 mM, and 1 M $FeCl_3$ form a solid aggregate that is not disturbed upon microcuvette inversion (right).

The non-ergodic nature of aggregates (the aggregate being large compared to the incident light beam) at high chemical concentrations, and for erythrocyte suspensions, makes light scattering measurements inaccurate, but aggregation at these concentrations is clear both macro and microscopically.[72] Conversely, $CrCl_3$ does not result in aggregation in any of these assays. My findings suggest then that the aggregation of blood components in this model is due to charge-based mechanisms: the direct inner sphere binding of Fe^{3+} to plasma proteins and cell membrane–localized proteins, as well as binding of cells to FeOH precipitates. Importantly, conventional clotting occurs in concert with $FeCl_3$ induced

aggregation: at t=0, light scattering of $FeCl_3$-treated PRP is three times that of untreated PRP, but at t=20 min, both $FeCl_3$-treated and untreated PRP plateau at seven times the light scattering of PRP at t=0 (Figure 3.15). Further, we found that aggregation is similar in the presence and absence of physiologically relevant concentrations of the covalent ions Ca^{2+} and Mg^{2+}(Figure 3.16).

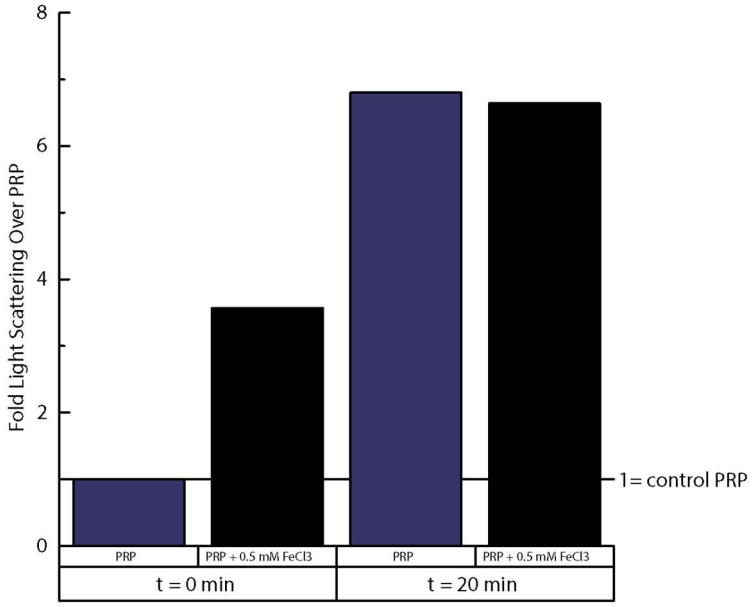

Figure 3.15. Physiological clotting occurs in addition to $FeCl_3$-induced aggregation. At t=0, PRP + 0.5 mM $FeCl_3$ scatters approximately three times as much light as PRP. After a 20 minute incubation, PRP and PRP + 0.5 mM $FeCl_3$ reach the same level of aggregation (approximately 7x that of unclotted PRP).

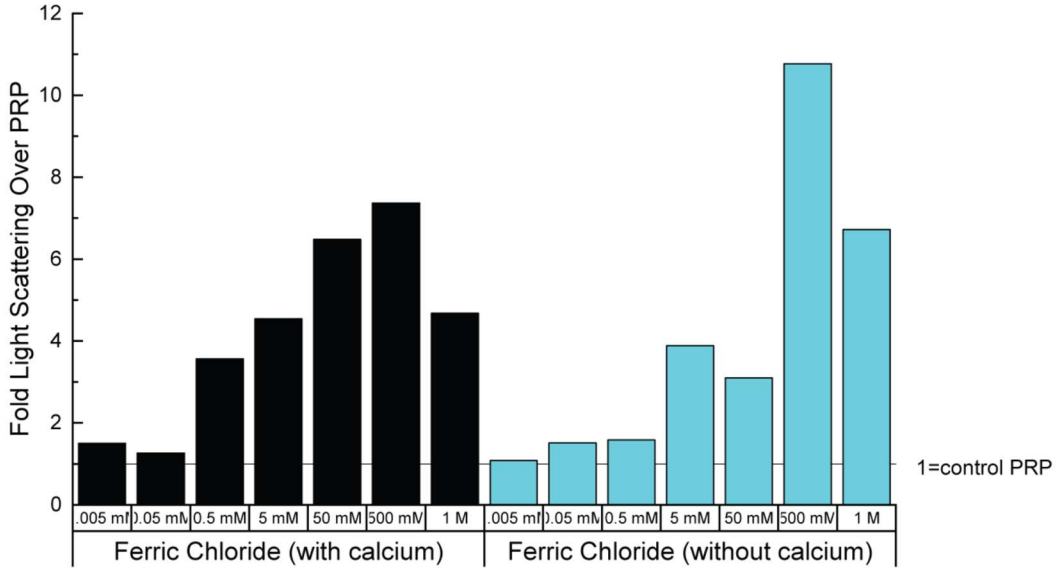

Figure 3.16. Light scattering of PRP with $Ca^{2+}$and Mg^{2+}.Light scattering was similar between PRP samples with and without the addition of calcium ions.

3.3.6 Determining the Role of $FeCl_3$ in Altered Hematological Environments

While the experiments performed implicate a charge-based mechanism of blood cell aggregation, *in vivo*, the $FeCl_3$ injury model has utility in studying clotting: clotting can be mitigated by the administration of therapeutic antithrombotic agents, as well as in knock-out mice whose clotting mechanisms are hindered.[73-76] This would suggest that, in addition to charge-based aggregation, the clotting cascade plays a role in the $FeCl_3$-induced thrombosis injury model. Altered clotting environments can be recreated *in vitro* and effects similar to those shown *in vivo* can be seen: cell aggregation and channel occlusion is mitigated when blood is pretreated with therapeutic antithrombotic agents and then exposed to 50 mM $FeCl_3$. However, when the $FeCl_3$ concentration is increased to 500 mM, the protective effects of the therapeutics are largely overcome.

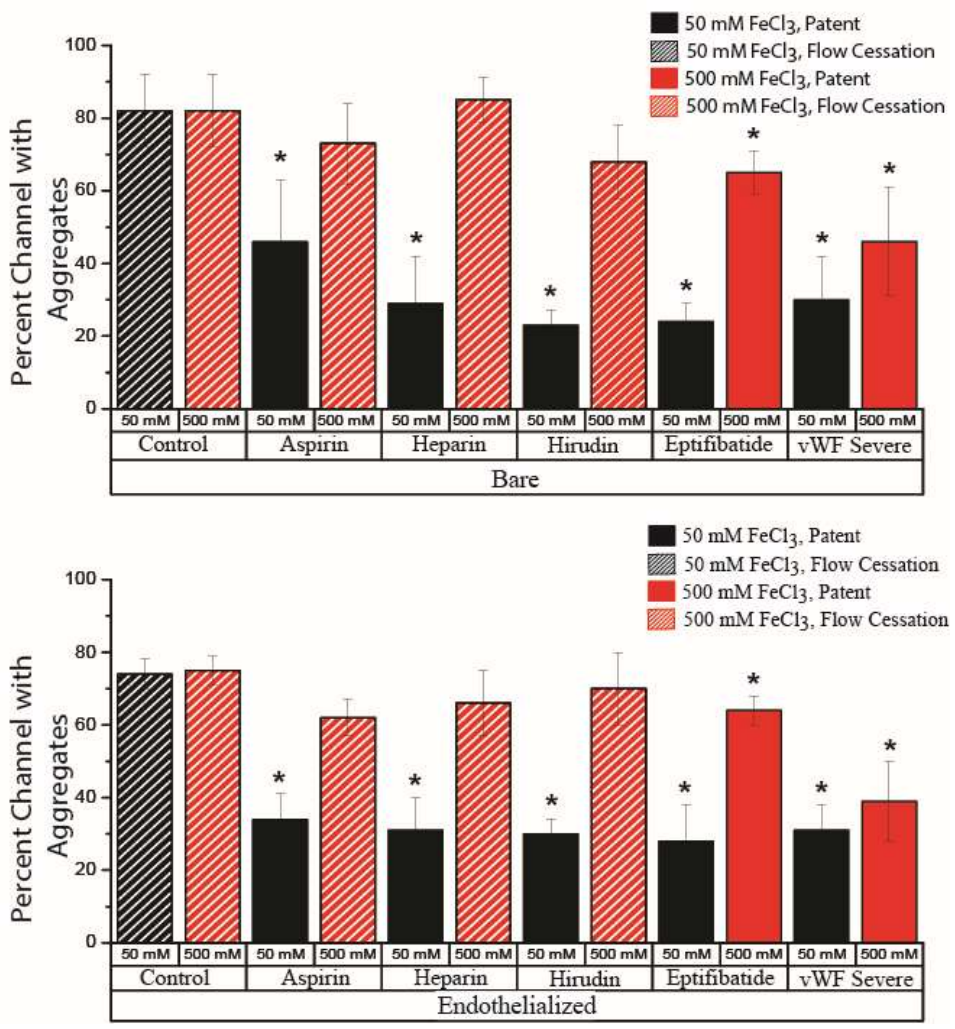

Figure 3.17. Aggregation of blood in altered clotting environments. In bare microfluidics, all drugs and phenotypic abnormalities lead to significant decreases in channel occlusion at 50 mM ($P < 0.5$) compared with the control solution, but 500 mM $FeCl_3$ overcomes the protective effect of aspirin, heparin, and hirudin In endothelialized microfluidics, drugs and phenotypic abnormalities lead to significant decreases in occlusion at 50 mM ($P < 0.5$), but 500 mM $FeCl_3$ overcomes the protective effect. Solid bars represent patent channels whereas the slant pattern represents flow cessation. There was not a significant difference in occlusion between untreated control blood exposed to 50 mM and that exposed to 500 mM. Significance is denoted by an asterisk (*), and was measured by a 2-tailed, Student t-test between the treatment condition and its paired control (eg, 50 mM control and 50 mM aspirin). N=4.

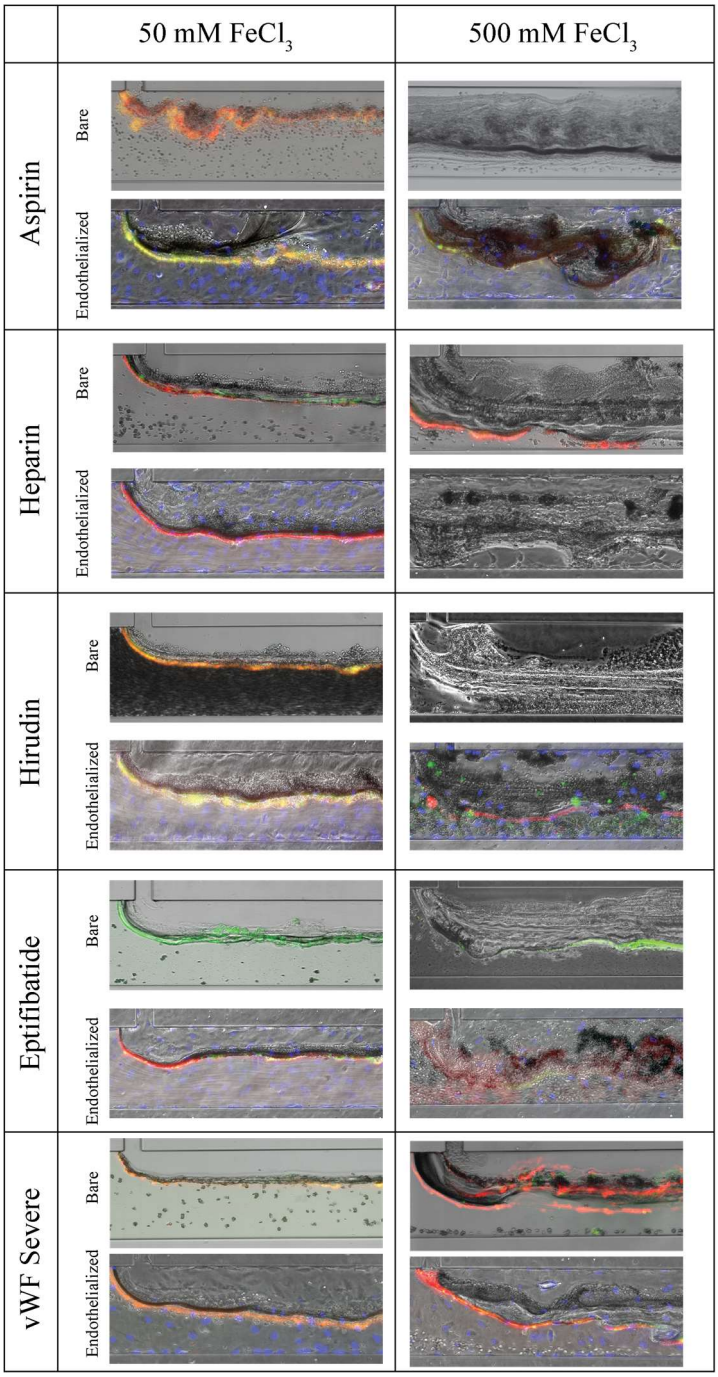

Figure 3.18. Blood cell aggregation in treated conditions. Representative images from drug treatments in bare and endothelialized microfluidics, at 50 mM and 500 mM. Platelets (green: CD41), fibrinogen (red), endothelial cells (blue).

Further, while blood from wild type mice formed an occlusive aggregate in the microfluidic when exposed to 50 mM $FeCl_3$, blood from mice lacking integrin GPIb-α (to bind vWF, a clotting factor) formed loose aggregate networks and vessel patency was

maintained, though aggregation was still extensive (Fig. 6D). I hypothesize that "at increasing $FeCl_3$ concentrations, pharmacologic inhibition does not effectively prevent channel occlusion because, although the clotting cascade is compromised, the $FeCl_3$ concentration is sufficiently high across the channel to induce charge-based aggregation." [77]

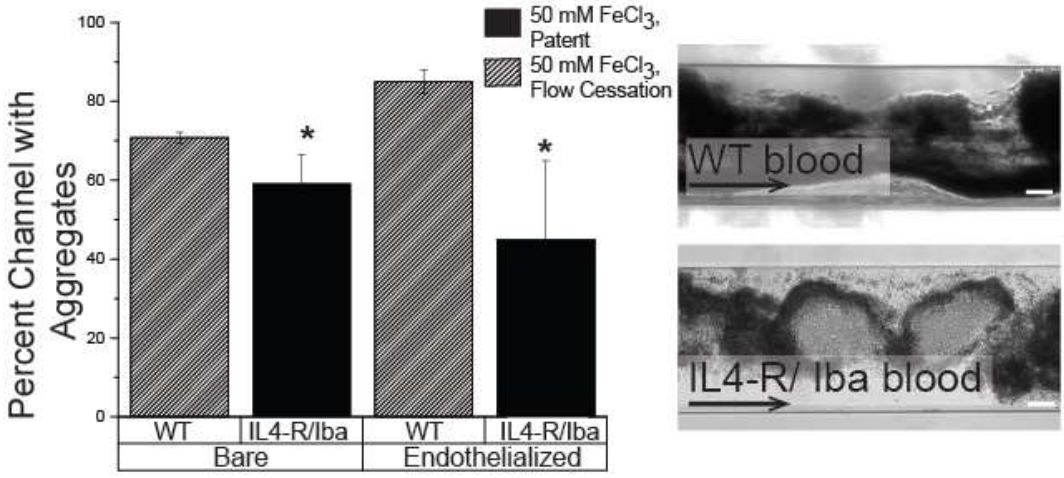

Figure 3.19. Aggregation in GPIb-alpha knock-out mice In bare and endothelialized channels, IL4-R/Iba blood forms fewer aggregates at 50 mM $FeCl_3$ than WT blood, and the channel remains patent. Representative image of WT blood and IL4-R/Iba blood aggregation in the microfluidic channel. All scale bars represent 50 μm; N = 4. Solid bars represent patent channels while the slant pattern represents flow cessation. Significance is denoted by an asterisk (*), and was measured by a 2-tailed, Student t-test between the treatment condition and its paired control (eg, 50 mM control and 50 mM aspirin).

3.3.7 Elucidating the Role of Mass Transfer in the $FeCl_3$ Injury Model

The extent of blood cell aggregation in the $FeCl_3$ injury model is highly dependent on the concentration of $FeCl_3$ throughout the vessel. This concentration varies based on the concentration applied to the vessel, properties of the vessel wall itself (thickness, composition, etcetera), and the fluid environment in the vessel. While the first two factors are outside of the scope of this study, the blood velocity and diameter of different blood vessels that $FeCl_3$ is applied to in the literature are considered. To determine how the

chemical concentration varies radially downstream of the patch site in different vessel types, I performed computational fluid dynamic (CFD) simulations for mass transfer of a dilute species using COMSOL (Figure 3.20). In small vessels, and those with lower blood velocities, the effective concentration that leads to aggregation (0.5 mM, as determined by *in vitro* experiments) is present across a larger extent of the vessel: in the carotid artery, the chemical reaches 12% of the vessel diameter, while in the mesenteric veins, it reaches 40% of the vessel. The extent of $FeCl_3$-induced clotting is then governed by mass transfer within different vessel types. This insight from mass transfer begins to resolve differences in the literature that arise when $FeCl_3$ is used on different vessel types.

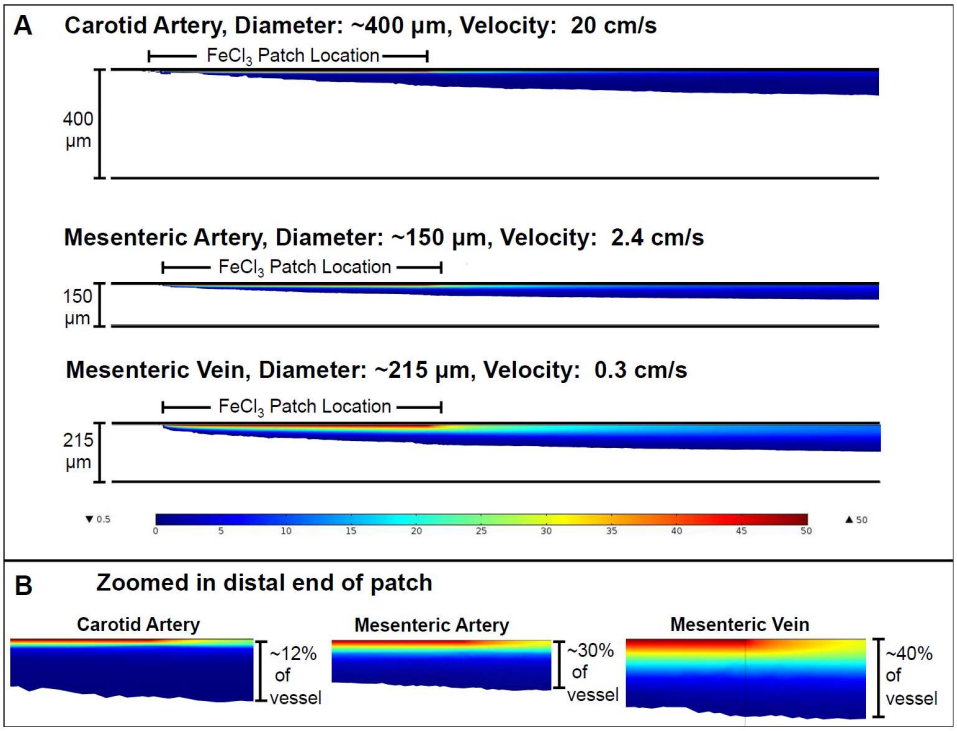

Figure 3.20. Mass transfer of $FeCl_3$ in relevant vessels. The role of vessel parameters (diameter and blood velocity) on transport of ferric chloride within the vessel was explored via COMSOL modeling. To focus on the role of mass transfer in the lumen, it was assumed that the intraluminal near-wall concentration was 50 mM for all vessel types; in other words, we ignored possible differences in diffusion of ferric chloride through the wall of the three vessel types. (A) The ferric chloride concentration profile in different vessels, where only concentrations greater than 0.5 mM are plotted (the concentration at which we have shown ferric chloride induces aggregation). (B) Zoomed in view of the concentration profile at the edge of the ferric chloride patch. The mesenteric vein has the largest span of concentrations over the largest vessel percentage due to its relatively low velocity of 0.3 cm/s.

3.4 Conclusions

Using the *in vitro* T-junction microfluidic system, I studied the effect of $FeCl_3$ on individual blood components and discovered that clot initiation and initial cell aggregation are due to complexation between negatively charged blood cells/ proteins and the positively charged iron species. Introducing therapeutics into the system allowed me to show that once clotting is initiated by $FeCl_3$ it continues by the standard clotting cascade,

but that the difference between concentrations that causes these disparate effects is small (Figure 3.21). These findings account for the varied results in literature for different injury models and different application locations and procedures, especially given the inability to tightly control $FeCl_3$ concentration *in vivo*.

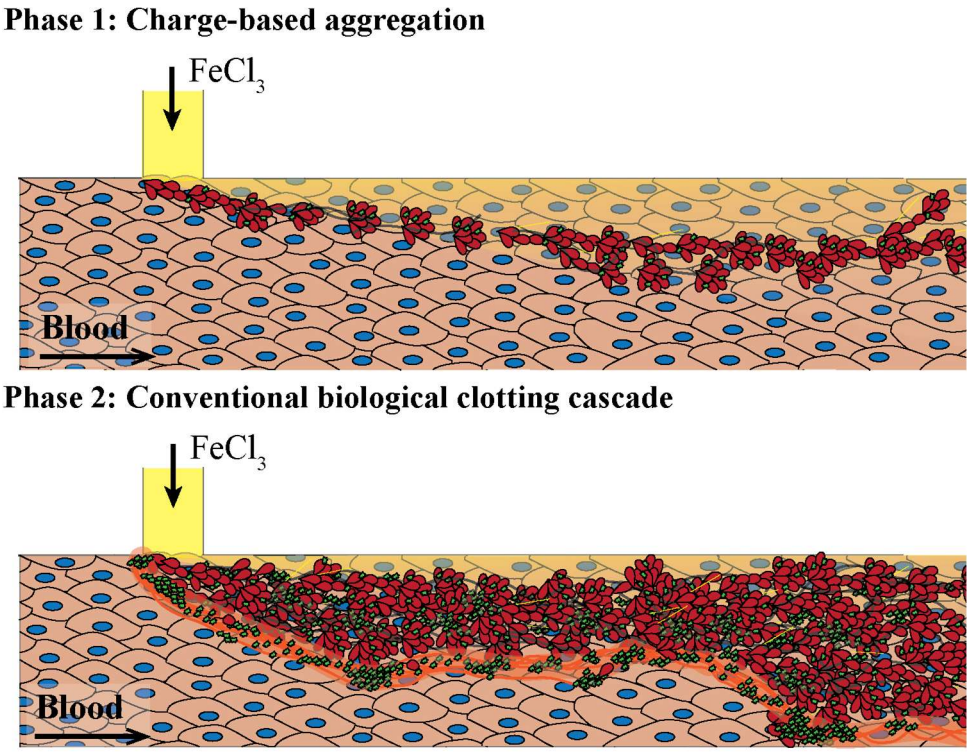

Figure 3.21. Two-phase mechanism of ferric chloride injury model. In the first phase, negatively charged RBCs bind to positively charged iron species and adhere to the endothelial surface. There are few proteins and platelets associated with the bound material. In the second phase, adherent blood cells and damaged endothelial cells initiate biological clotting cascade. Proteins and platelets are more abundant in the aggregate in this phase. Fibrinogen is shown to form a boundary layer at the distal edge of the aggregate.

"The controlled reductionist environment afforded by the *in vitro* endothelialized microfluidic system allows for precise control over $FeCl_3$ induced thrombosis and led me to propose a novel, two-phase mechanism for the action of $FeCl_3$ in thrombus formation. The first phase is independent of typical biological "clotting," and consists of the $FeCl_3$ concentration- dependent binding of negatively charged blood cells and proteins to

positively charged iron species. The adherent cells from the first phase initiate the second phase, the standard biological clotting cascade. Where one phase ends and the other begins is non-trivial to determine, as the effective $FeCl_3$ concentration in the channel (which determines the extent of the first phase) is dependent on mass transfer phenomena both through the vessel wall and in the vessel itself. Researchers should take caution that this will affect their findings, especially in small vessels, and that aggregation phenomena that seemingly suggest a novel ligand/receptor interaction may in fact be due to non-specific charge based-binding effects." [77] The results and figures presented in this chapter were published in *Blood* in 2015.

CHAPTER 4: DESIGNING MICROFLUIDIC DEVICES TO EXPLORE THE INTERACTIONS OF BLOOD CELLS WITH BIOPHYSICAL MATRICES

4.1 Introduction

Blood cells encounter a number of matrices: platelets transit nascent fibrin clots, red blood cells are filtered through the spleen's interendothelial splenic slits, and white blood cells extravasate through endothelial cell gaps. Biochemical aspects of cellular process are well characterized, but more recently, it has been shown that cells dynamically sense and respond to biophysical cues such as substrate stiffness and geometrical constraints; physical cues even direct cell differentiation and stem cell lineage.[1, 78] Blood cells pass through, and interact with, biological matrices such as fibrin clots and the vascular wall, but the physical and biochemical aspects of these interactions are largely indistinguishable from one another *in vivo*. As such, there is a gap in knowledge as to how RBCs deform through geometrically challenging matrices and how blood cells in general activate and respond to matrices as they transit them. The biological matrices that blood cells typically transit are on the size scale of hundreds of nanometers to single microns, both in terms of pore/ gap size and fiber diameter.[32, 79, 80] To begin to better understand the activity of cells when challenged by such matrices, a suite of microdevices was designed and fabricated to allow for real-time visualization of single cell/ matrix interactions. Creating features of these dimensions using traditional photolithography is non-trivial, so a silicon wafer was templated by electron-beam lithography (EBL) and then directly poured with polydimethylsiloxane (PDMS). A standard microfluidic channel can then bonded on top of

the array to create a sealed device through which blood components are perfused. To that end, we created a micropillar array to recapitulate the deformation of cells through individual matrices of "fibers" as well as a microcanal array that requires cells to deform in a tightly confined geometry over different time scales (this also corresponds to monitoring the response of cells to steep pressure drops at the point of constriction).

4.2 Materials and Methods

4.2.1 Device design

Microfluidics were designed to recapitulate the interactions of single cells with vascular matrices; the simplest controlled realization of these interactions can be described by the movement of cells through a pillar array with "fiber" size of 900 nm and gap size of 2 μm. These dimensions are on the size scale of physical geometries of diverse vascular matrices and PDMS is of a similar stiffness of various matrices, including fibrin clots, endothelial cell gaps, and splenic slits.[32, 79, 80] Micropillar arrays have previously been fabricated both in silicon and PDMS, often to describe the mechanical forces of cells or for the size-based separation of cells.[81-83] To our knowledge, however, no other system attempts to describe the interaction of cells and matrices by flowing cells through single micron pillar arrays. Likewise, while there are many studies (computational and microfluidics-based) that describe aspects of cell deformation, there is not currently a system that aptly describes deformation through a physically challenging geometry over different time scales, and thus a device to parse out the parameter space for RBC deformation versus fragmentation. [30, 35, 84-86] Thus, a simplified system of microcanals was created to recapitulate cell deformation over time. (Figure 4.1).

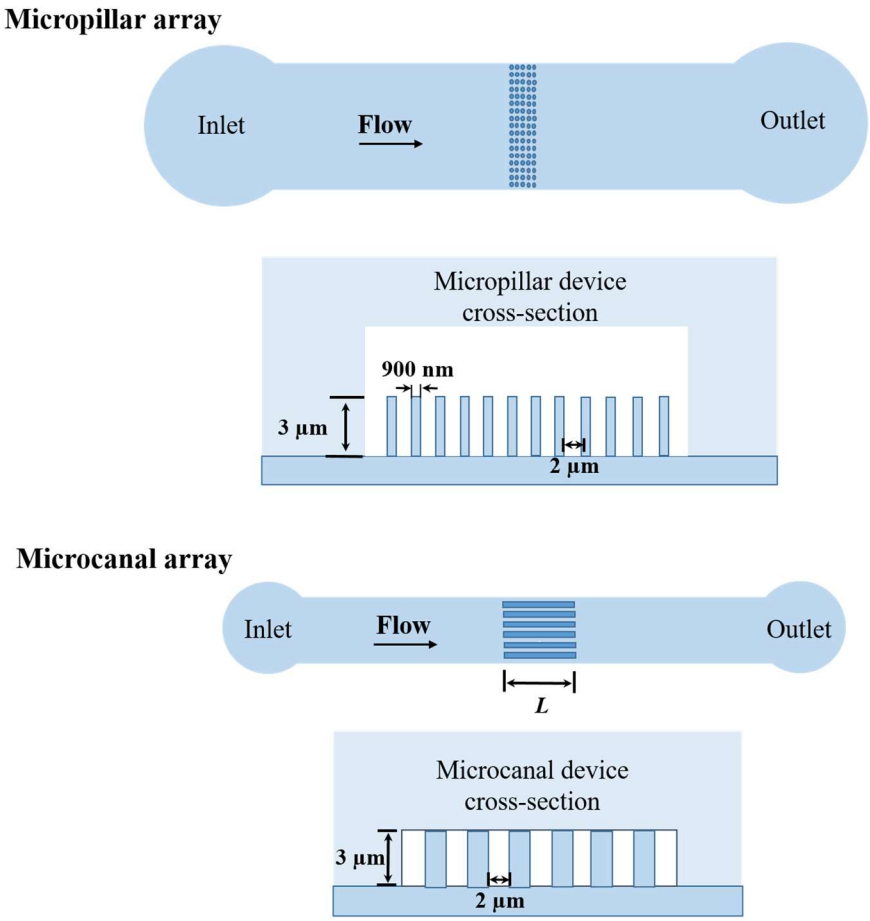

Figure 4.1 Schematic of micropillar array and microcanal devices.The micropillar (top) and microcanal (bottom) arrays both are highlighted by challenging physical geometries that cells are required to transit. The micropillar array is made up of pillars that are 900 nm in diameter, 3 µm in height with a 2 µm gap between adjacent pillars. The microcanal array features canals of lengths ranging from 5-90 µm with a transit cross-section of 2 µm width and 3 µm height

4.2.2 Device fabrication

To study the interactions of blood cells with their biophysical microenvironment, microfluidic devices were designed to have features on the order of biologically relevant matrices, that is < 3 µm. As creating high fidelity features of this dimension using traditional photolithography is non-trivial, electron-beam lithography (EBL) was used to create a silicon wafer template that could be used to create microfluidics via direct soft lithography using the elastomeric polymer, PDMS (Corning). To mitigate the poor silicon

to photoresist selectivity for deep etching of the sub-micron features, a layer of SiO_2 was deposited via plasma-enhanced- vapor-deposition (PECVD) to form a hard mask. Next, a thin layer of electron-beam- lithography (EBL) photoresist was spun on the SiO_2 layer and patterned using the EBL tool. Dry-etching transferred the patterned features from the photoresist to the hardmask. The silicon wafer was then etched. While EBL's sequential deep reactive-ion etching (DRIE) and passivation cycles of the Bosch process generally result in side wall roughness (scalloping), an optimized recipe, termed the nano-Bosch process, results in smooth side walls etched in the silicon substrate. [87, 88] The resulting feature smoothness is necessary for the successful release of cured PDMS from the master. Thus, using EBL, a silicon master was patterned with holes to create PDMS pillars (~900 nm diameter and 3 μm height, with a 2 μm gap) or with vias to create PDMS canals (2 μm width and 3 μm height, with lengths from 2-90 μm). After patterning, the silicon master was vapor treated with HMDS to create a hydrophobic substrate that further encourages PDMS release. PDMS (at a 10:1 ratio of elastomer to curing agent) was poured over the treated silicon wafer and the wafer was placed in a vacuum chamber for ~1 hour to ensure PDMS entry into the micron-sized features. PDMS was then cured overnight at 60 C, before the PDMS devices were cut out and the wafer was repoured. The direct EBL-patterned PDMS "feature layer" serves as the bottom surface of the microfluidic device.

To create a closed microfluidic device, PDMS channels were created from silicon wafers templated via traditional photolithography and SU-8. Surface activation of both layers (feature and channel) was accomplished using a handheld Corona Treater (Electro-Technic Products), and PDMS layers were bonded by aligning them under a microscope and placing the bonded device on a hot plate at 80 C for 10 minutes to set bond. The two-

part system—features on one PDMS layer and channels on another—allows the user to mix and match between micron-sized features and channels to study the desired system. For platelet micropillar experiments, the channel was 150 μm wide and 6 μm tall, inlet and outlet holes were punched ~500 μm from array, and the long axis of the micropillar array was bonded perpendicular to flow direction. For RBC and neutrophil micropillar experiments, the channel was 150 μm wide and 3 μm high to force the cells through the array. The channel for the microcanal device was 26 μm wide and 3 μm tall, and each canal was approximately centered between inlet and outlet holes that were ~1 mm apart. An additional outlet hole was punched downstream of the first outlet hole to reduce fluidic resistance and create a viewing window of cells post-canal.

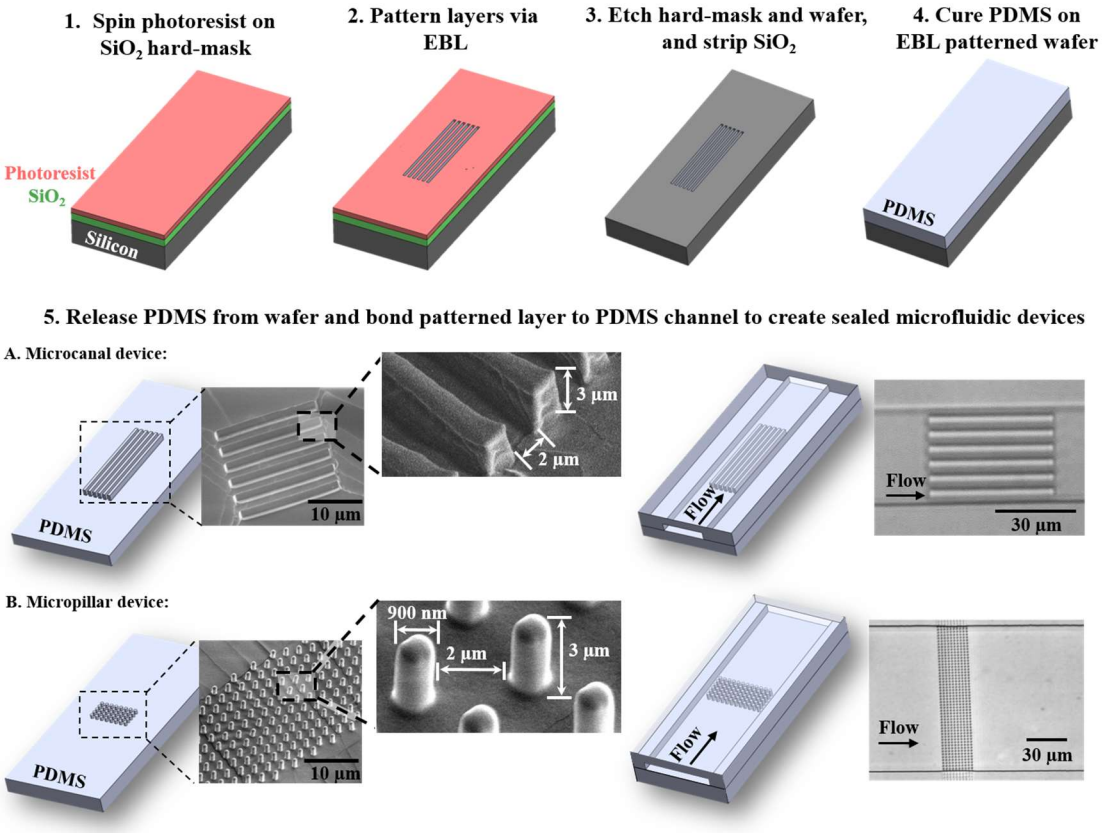

Figure 4.2 Fabrication of single-micron scale devices. (1-3) Electron beam lithography (EBL) was used to pattern the silicon wafer. (4) Direct soft lithography was used to transfer the pattern from the silicon wafer to PDMS. (5) Release cured PDMS from the silicon mold (SEM of PDMS features) and bond the EBL feature layer (A: microcanal, B: micropillar) to the desired PDMS channel.

4.2.3 Device characterization

Inspection and characterization of the PDMS features was achieved by scanning electron microscopy (SEM). SEM images confirm that direct lithography from a silicon master achieves PDMS pillars and canals of the expected geometries and dimensions (Figure 4.2). By performing SEM on devices after a number of pours, we saw that there was minimal loss in feature quality after >20 PDMS pours.

4.2.3.1 Micropillar Array Fluidic Environment

It is well established that blood components respond to shear stress and shear gradients, so characterizing the shear microenvironment of the micropillar array is of interest.[89] Shear stress (τ) in microfluidic channels can be estimated by a 2-D approximation as: $\tau = \frac{6Q\mu}{wh^2}$, where Q is the flow rate, μ is the viscosity, w is the channel width, and h is the channel height. A more precise constant term based on the channel dimensions for the shear stress equation with a 3D velocity profile can be found using Fourier expansions. [90, 91]. Using a two dimensional laminar flow COMSOL model for a 6 μm tall channel with an input velocity of 0.2 μL/min, the max fluid shear is calculated to be ~ 50 dyne/cm^2 in the micropillar array. (Figure 4.3) This shear is at the low end of pathological shear, or the shear that would be expected in a diseased state. The pillar geometry results in areas of high shear as well as stagnant zones behind the pillars; this creates areas with large shear microgradients. Different numbers of pillars in the arrays (5 or 10 columns), and consecutive pillar rows being either offset or inline with one another does not change the shear microenvironment. Due to the stiffness of the PDMS pillars and their aspect ratio, there is no visible shear induced deformation of the pillars themselves.

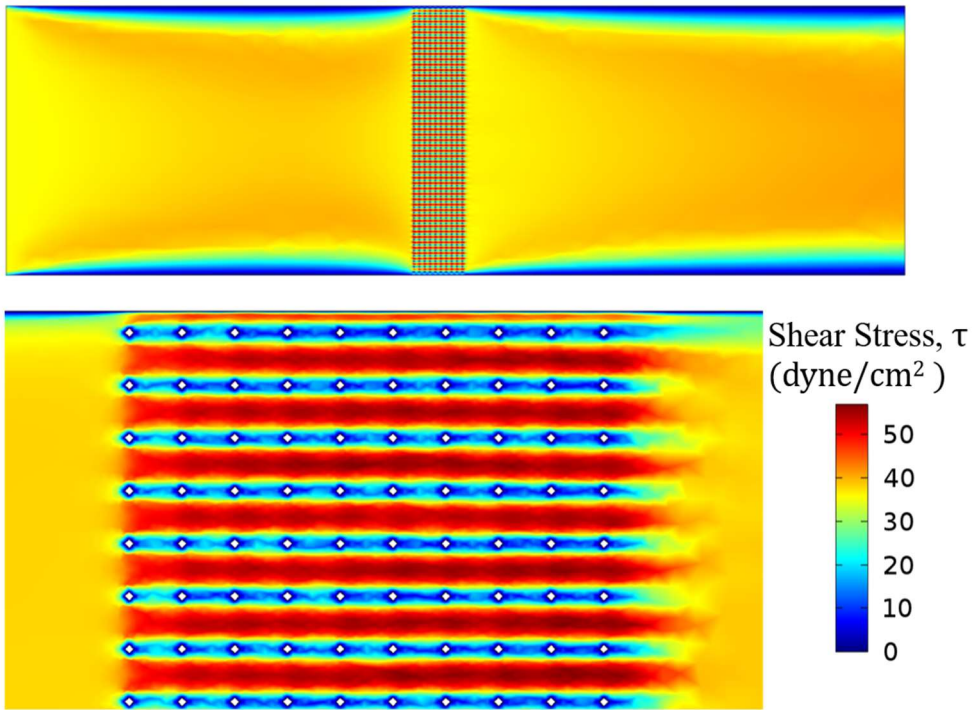

Figure 4.3. Shear microenvironment in the micropillar array. Shear stress profile in a 6 µm tall, 150 µm wide channel with ten columns of aligned micropillars. Close-up of pillar environment shows a maximum shear of ~50 dyn/cm^2 (shear rate of 5,000 1/s)

4.2.3.2 Microcanal fludic environment

The small cross-sectional area of the canals results in a very large shear stress (~20,000 dyn/cm^2) and while changing the length of the channel changes the length over which the cell is exposed to the high shear stress, it does not change the magnitude of the shear stress itself. The fluidic resistance in the canals, however, does change with canal length, and thus the pressure drop across the canals also changes with canal length. To find the pressure differential, I modeled the canal array in 2D with COMSOL, with an inlet flow of 0.5 µL/min and a boundary condition of atmospheric pressure (P=0) at the outlet.

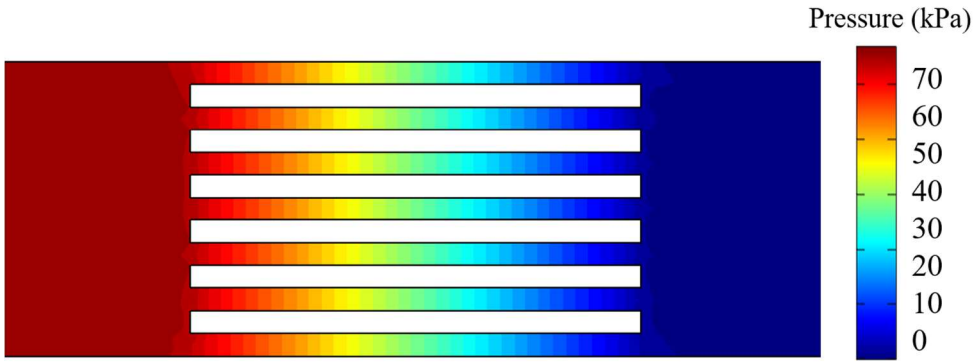

Figure 4.4 Pressure drop across a 40 µm microcanal device. There is a pressure drop of ~70 kPa across 40 µm microcanals.

Pressure calculations in the microcanals can also be approximated by modeling microfluidics as circuit.[90] Briefly, Ohm's law,

	$V = IR,$	(3)

where V is voltage, I is current, and R is resistance has an analogue in microfluidics via the Hagen Poiseuille law

	$\Delta p = QR_H,$	(4)

where Δp is the pressure drop across a channel, Q is flow rate, and R_H is the hydraulic resistance. R_H depends on fluid viscosity (µ) and channel width (w), height (h), and length (L). For a channel where $w \sim h$:

	$R_H = \frac{32\mu L(w+h)^4}{\pi(wh)^4}.$	(5)

Pressure drop then varies directly with the length of the microfluidic channel. As in circuits, microfluidic channels in parallel can be added as resistors in parallel:

	$\frac{1}{R_{eq}} = \frac{1}{R_{H,1}} + \cdots + \frac{1}{R_{H,n}}$	(6)

The canal fluidic can be treated as a circuit in which there are seven parallel resistors of the same resistance, as the channels have the same width, height, and length. The total resistance, R_{eq}, is then

	$R_{H,eq} = \frac{R_H}{7}.$	(7)

For blood (μ= 3.2x10^{-3} Pa·s) perfused at a flow rate of Q=0.5 μL/min, the pressure drop across microcanals of w= 2 μm, h =3 μm, and l is:

	$\Delta p = 4.61x10^9 \times l$ [Pa].	(8)

For canal lengths from 10- 90 μm, the pressure drop ranges from ~46 kPa to 415 kPa. We also designed microcanals with a cross-sectional area of 3 μm x 3 μm. In this case, the pressure drop across the microcanals is:

	$\Delta p = 1.91x10^9 \times l$ [Pa],	(9)

resulting in a pressure drop ranging from ~19 kPa to 172 kPa for lengths (l) of 10-90 μm. For equivalent canal lengths, the pressure drop across the 2x3 μm cross-section canals is ~2.4 times that of the 3x3 μm cross-section canals. In other words, a 2x3 μm canal of length l has the same pressure drop as a 2x3 canal of length (2.4)·l. These calculations describe is the pressure drop before cells are introduced to the system as confirmed by the Comsol model. The pressure environment becomes more dynamic and complicated as cells plug individual canals and transit the canals. If a cell is blocking one canal, the pressure in the rest of the system increases by a factor of resistance. Thus, if all canals are blocked but one, the pressure drop is 7 times those reported above.

4.2.4 Introducing Biologics to the PDMS Surface

Directly after bonding, devices were blocked with 3% BSA via gravity driven flow. To ensure fully filled, bubble-free channels, a BSA droplet was pipetted over inlet and outlets and devices were placed in vacuum chamber for 1 hour incubation. Other biologics were introduced to the PDMS surface by gravity driven flow and passive adsorption: fibronectin (10 μg/mL) or collagen (1 mg/mL) incubated for 1 hour.

4.2.5 Collecting and Staining Human Blood Samples

Human blood was drawn according to institutional review board–approved protocols per the Declaration of Helsinki. Washed platelets were isolated by centrifuging whole blood (drawn into ACD) at 150 g for 10 minutes, collecting the supernatant (PRP), and centrifuging the supernatant at 900g for 5 minutes. The platelet pellet was then resuspended in Tyrode's Buffer containing 1% BSA. Platelets were stained with 2 uM Calcein AM or anti-CD41 antibody (Novus) at 1:200. RBCs were isolated by centrifuging blood (drawn into sodium citrate) at 150g for 10 minutes (no acceleration, no brake), discarding the supernatant, and washing 3x with PBS (400g for 7 minutes). RBCs were resuspended in PBS to ~20% hematocrit, unless otherwise noted. Staining red blood cells with R18 (Sigma) greatly affected their mechanical stability (cells are destroyed into membranous debris), and thus all RBC studies were performed using bright field microscopy (Figure 4.5).

Figure 4.5. R18 stained RBCs fragment into membranous debris when transitting microcanals. When R18 stained red blood cells are perfused through microcanal device, cells, they fragment into stringy, membranous cell debris. This suggests that R18 has a significant effect on RBC structural integrity.

Neutrophils were isolated from whole blood using MACSxpress® Neutrophil Isolation Kit; neutrophils were then washed in PBS (210g for 10 minutes) and resuspended in either PBS or PRP. Staining was performed by adding primary and secondary antibody directly to the cell mixture. Neutrophils were stained with a combination of Hoescht 33342 at 1:000 ; Sytox green at 1:200 ; anti-histone H3 (Abcam, ab5103) at 1:200; or anti-elastase (Abcam, ab68672) at 1:200. Samples were perfused through microfluidic device at 0.5 µL/min using Harvard Apparatus syringe pump.

4.3 Results and Discussion

4.3.1 Platelets Adhere and Aggregate Due to the Physical Presence of Micropillars

Shear stress is known to be a biophysical activator of platelets, and the pathological relevance of shear stress is well described, especially as it relates to von Willebrand Factor (vWF) mediated clotting and the progression of atherosclerosis.[92-95] Literature suggests various shear ranges at which platelets adhere to surfaces, activate in the presence or absence of soluble factors, and aggregate.[89, 96] In addition, platelets are shown to bind immobilized ligands at different shear rates: platelet integrin αIIbβ3 binds fibrinogen at low physiological shear rates of 600-900 1/s while platelet integrin GPIb–A1 binds von Willebrand Factor (vWF) at 1,000-10,000 1/s.[97] While many studies

specify overall shear stress that platelets encounter, others instead argue that shear microgradients are more important to platelet activity.[98] Microfluidics allow for the piecewise study of these questions, and as our COMSOL simulations show, the micropillar array creates regions of high shear as well as stagnant zones.

The biophysical interaction of platelets with a PDMS matrix (absent biological factors) was thus recapitulated by the micropillar microfluidic device. Perfusion of washed platelets through the channel results in specific, localized platelet adherence to the pillars, extensive platelet aggregation, and the formation of an occlusive mass that extends to the edges of the micropillar array to arrest flow. (Figure 4.6)

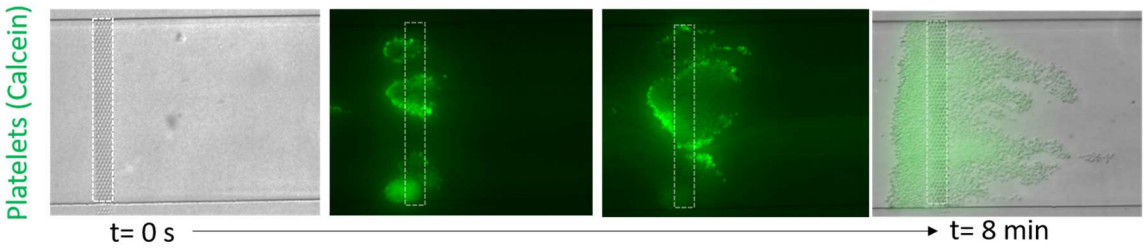

Figure 4.6. Platelets adhere and aggregate due to physical presence of pillars. Platelets (stained with calcein) are perfused at 0.2 µL/min through the micropillar array (white outline). The width of the pillar array is 15 µm.

Platelet adhesion initiates exclusively at the pillars and aggregation propagates to the extents of the channel area perpendicular to flow, resulting in channel occlusion and flow cessation. These findings suggest that in the absence of platelet agonists and biological ligands, platelets are activated by the shear environment afforded by the physical presence of "fibers." Thus, in addition to the biochemical players in clot formation, the geometry of the matrix with which platelets interact plays a role in platelet adhesion and clot propagation. As expected, passive adsorption of collagen and fibronectin to the pillar surfaces enhances platelet aggregation, as evidenced by a decrease in time to channel

occlusion from 10 min to 6 min and 2 min, respectively (Figure 4.7). This finding then begins to describe the synergistic action of biophysical and biochemical factors in clot propagation. This microfluidic both separates biophysical and biochemical aspects of clot formation and allows researchers to specify the precise location and extent of clot formation *in vitro*. Platelets were also perfused through the microcanals, but they did not adhere or aggregate within the microfluidic. The gaps are large enough for platelets to transit without interacting with the PDMS structures, and while the shear stress is sufficiently high for platelet activation, I posit that the lack of stagnant zones (and thus the lack of a shear microgradient) throughout the device prevents platelets from activating and then adhering. The shear stress in the device is also high enough to discourage adherence.

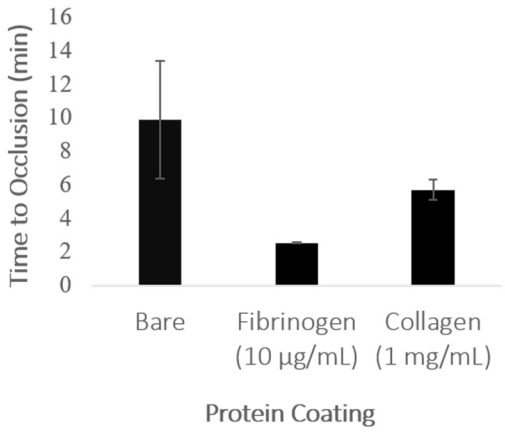

Figure 4.7. Platelet activity is enhanced by adsorbing biologics to PDMS micropillars The average time to channel occlusion (cessation of flow) is graphed for bare pillars, fibrinogen coated pillars, and collagen coated pillars. Fibrinogen coated pillars greatly increase platelet adherence and aggregate propagation.

4.3.2 RBC Fragmentation is a Function of Time in Deformed State

Red blood cells are highly deformable, allowing them to readily transit the 3-4 µm diameter capillaries of the microvasculature. They also maintain their oxygen carrying capability in the variety of the shear rates experienced in the vasculature. However, it is

known that RBCs can fragment *in vivo* when there is extensive pathological clotting, as well as in the presence of heart valve implants. The presence of the resulting cell fragments, termed schistocytes, on a blood smear is used as a diagnostic for pathologies such as hemolytic uremia syndrome (HUS), thrombotic thrombocytopenic purpura (TTP), and disseminated intravascular coagulation (DIC).[41, 99] While the *in vivo* presence of schistocytes is documented in the literature and there are many studies about quantification methods, the mechanism by which they are formed is not well characterized. A carefully conducted SEM study in 1970 reported that schistocytes result when "rapidly moving red cells encounter fine fibrin strands," and the resulting image of "hanged red blood cells" from the study is used extensively in medical literature.[100]

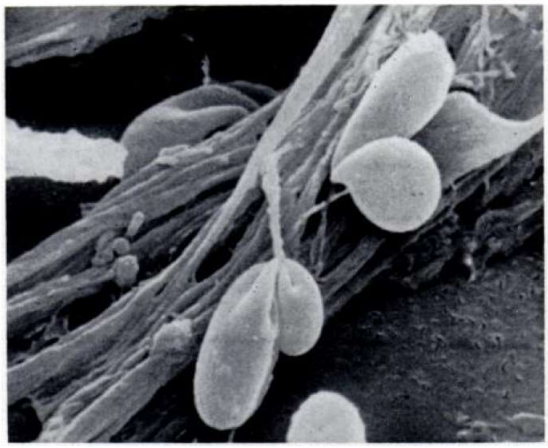

Figure 4.8. Red blood cell wrapped around a fine fibrin strand. SEM of a fixed sample from a patient with macroangiopathic hemolytic anemia. This is shown as the visual evidence for the mechanism of schistocyte formation. Image taken from [100]

The process of fragmentation is usually described in as a fibrin strand instantaneously cutting a cell in two, and the fibrin fibers have even been compared to a "guillotine."[101] Damaged RBCs can also rupture, expel their cytoplasmic load—hemoglobin— and become ghosts, or empty, closed membranous sacks. RBCs have been found to hemolyze at fluid-fluid shear interfaces of >15,000 dyn/cm^2, and at fluid-solid

interfaces between 1,500 and 3,000 dyn/cm^2.[41] However, the conditions under which these disparate states of damage result are largely unknown. Understanding the biophysical parameter space for RBC damage, fragmentation, and destruction is of immense interest for improved understanding of disease state as well as for development of diagnostics. (See Section 2.3.1 for discussion of RBC deformation and morphological abnormalities) To that end, we perfused RBCs in our micropillar and microcanal systems and analyzed their deformation in real-time.

RBCs deform elastically through the micropillar array: RBC morphology changes during transit, but RBCs return to their discoid shape upon matrix exit (Figure 4.9).

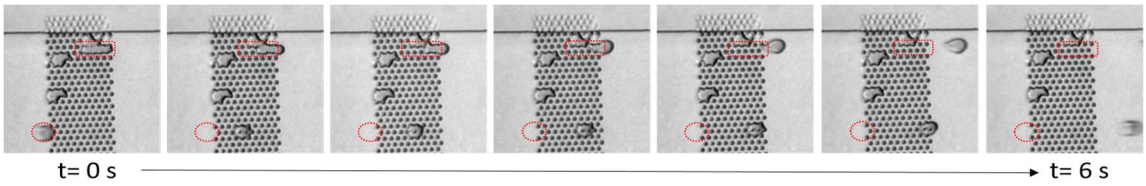

Figure 4.9. RBCs elastically deform through micropillar array. Over the course of 6 seconds, RBCs transit array with minimal downstream morphological changes.

This suggests that forces (including physical constriction) need to be maintained over an extended distance to affect plastic deformation of RBCs. To that end, the microcanal device challenges RBCs to deform through a 2x3 μm cross-sectional gap over various distances (length of canal). At short canal lengths (<20 μm), RBCs elastically deform through the canal; however, as canal length increases, RBCs emerge progressively more damaged. At 20-35 μm, a subset of cells emerge from canals as echinocytes—RBCs covered in short, blunt spicules—a reversible morphological change that is indicative of the ATP loss that is expected when RBCs are exposed to shear deformation (Figure 4.10).[39] At 35 μm lengths, there is intermittent RBC fragmentation, resulting in microspherocytes (Figure 4.10, black arrows).

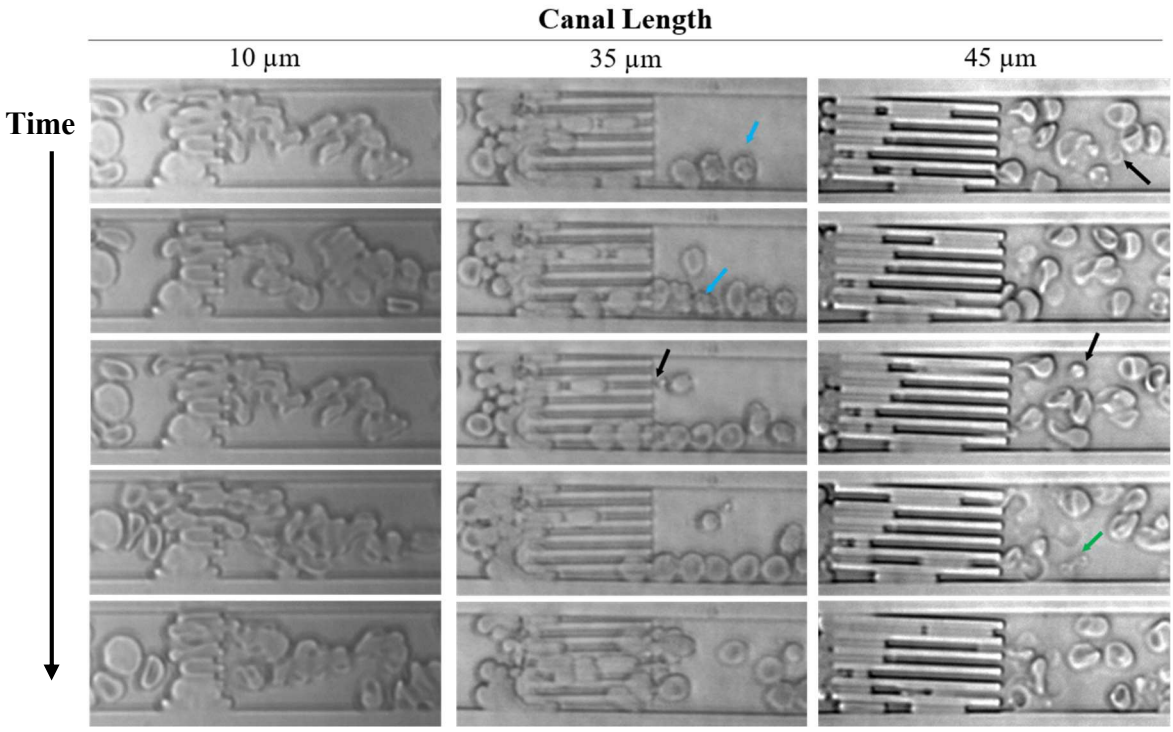

Figure 4.10 Time course images show that RBCs traverse short canals with minimal damage. As RBCs traverse 10, 35, and 45 µm lengths (top panel to bottom panel), the majority of cells emerge with minimal damage. As canal lengths increase, severity of damage also increases. Abnormal morphologies are denoted by arrows: blue for burr cells, black for microspherocytes, and green for schistocytes. Representative images from N>3.

At canal lengths > 70 µm, the majority of RBCs emerge as cell debris and ghosts—membranous sacs that have expelled their cytoplasmic load, hemoglobin. At interim residence times in a deformed state, RBCs emerge in fragmented morphologies: microspherocytes, or small spherical RBCs indicative of membrane and/or volume loss, and schistocytes. Resulting blood cell morphologies can be described, in part, by Giemsa staining of the effluent (Figure 4.13). Taken together these experiments suggest that different levels of damage occurs for different canal lengths, and thus possibly based on different pressures and times in a deformed state. Quantitatively, we see that the percent of damaged cells exiting the canal increases for increasing canal lengths, plateauing at 95%

damage for lengths > 50 µm (Figure 4.12). Based on qualitative analysis, we posit that different morphologies emerge at different canal lengths for canals with a 2x3 cross-section (Figure 4.14)

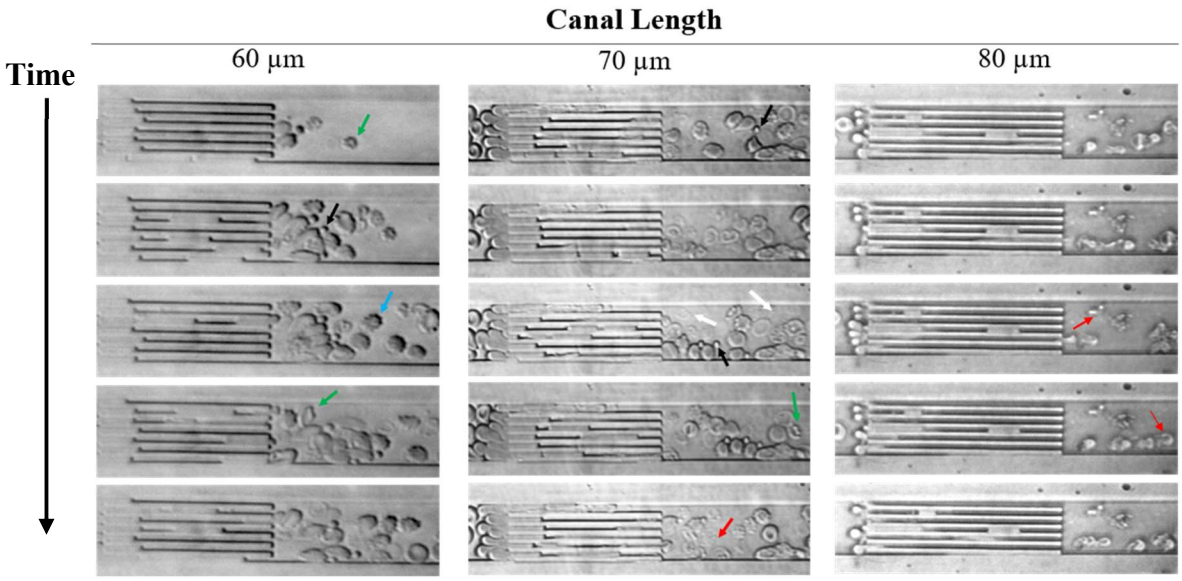

Figure 4.11. RBCs emerge damaged after traversing canals of 60, 70, and 80 microns. Time lapse of RBCs traversing canals (top to bottom in each column). Abnormal morphologies are denoted by arrows: green for schistocytes, blue for burr cells, black for microspherocytes, white for ghosts, and red for cell debris. N>3

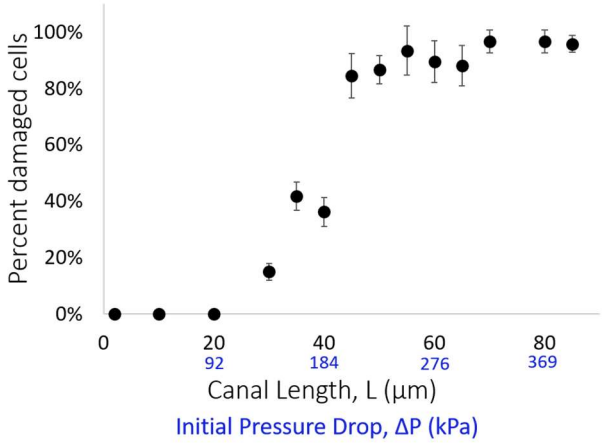

Figure 4.12. RBC damage increases with increasing canal length. As canal length increases, percent of damaged cells increases, beginning at around 30 µm and plateauing around ~95% at 50 µm.

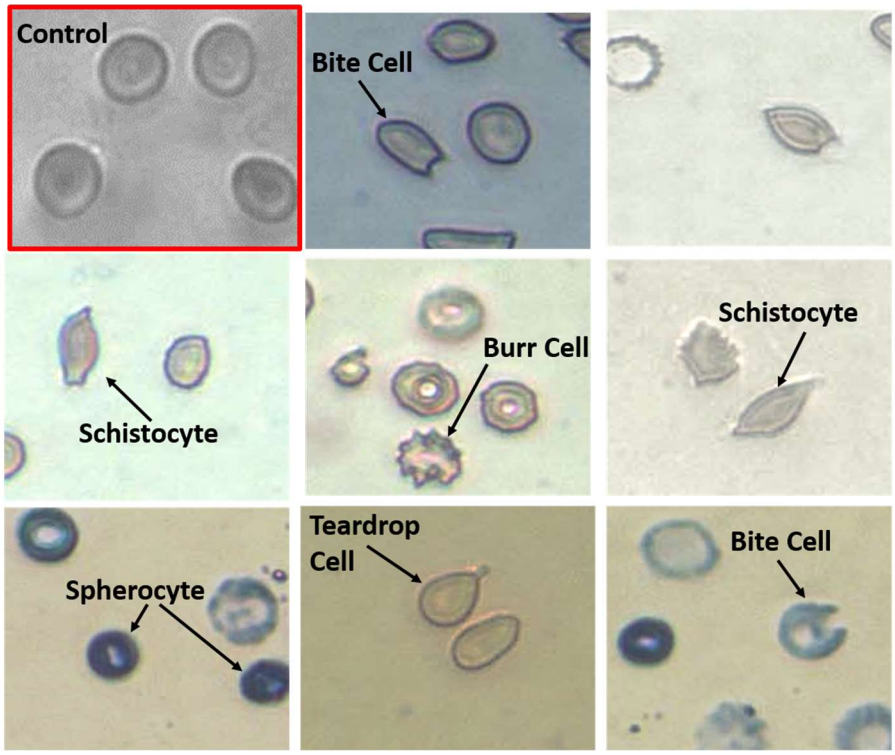

Figure 4.13. RBC morphologies present in microcanal effluent from a 60 µm canal. It appears that passage through canals results in various abnormal RBC. Spherocytes and microspherocytes were the most commonly seen abnormal RBC morphologies. Control cells refer to cells perfused through channel without canals.

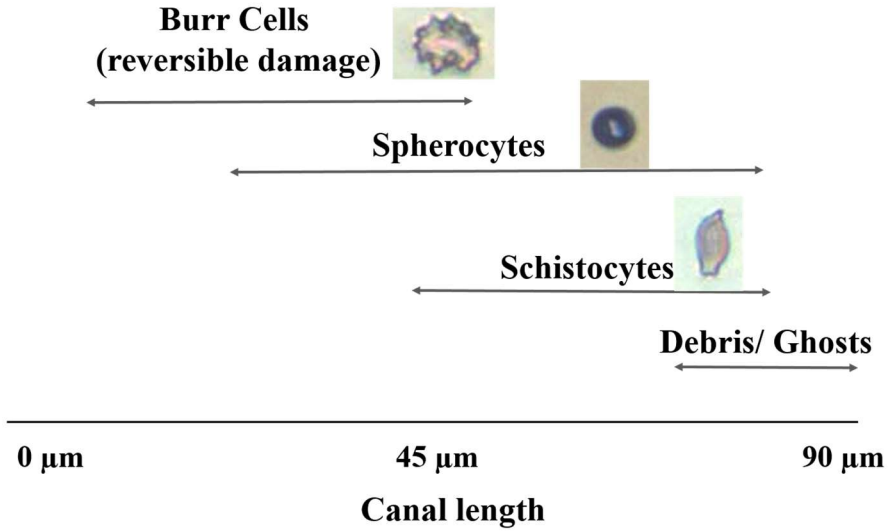

Figure 4.14. Proposed trend between canal length and RBC morphology. Based on experimental findings, it seems that ~20-50 µm lengths result in burr cells, >35 µm lengths result in spherocytes, >45 µm lengths result in schistocytes, and >70 µm canals result in ghosts and cellular debris.

If the degree of deformation is reduced by increasing the canal's cross-sectional dimensions to 3x3 µm, RBCs elastically deform for all tested canal lengths (up to 90 µm), with no discernible plastic changes (Figure 4.15). An array of 3x3 canals of 90 µm is similar in pressure drop to a 2x3 array of canals ~40 µm in length; we thus hypothesize that in this system, RBC mechanical damage and fragmentation require both a pressure differential and residence time under significant physical constraints. This is supported by quantifying the percent damaged cells: even when exposed to pressure drops that cause significant damage in 2x3 µm gap devices (40% of cells), all cells passing through the 3x3 µm array emerge morphologically unchanged (Figure 4.16).

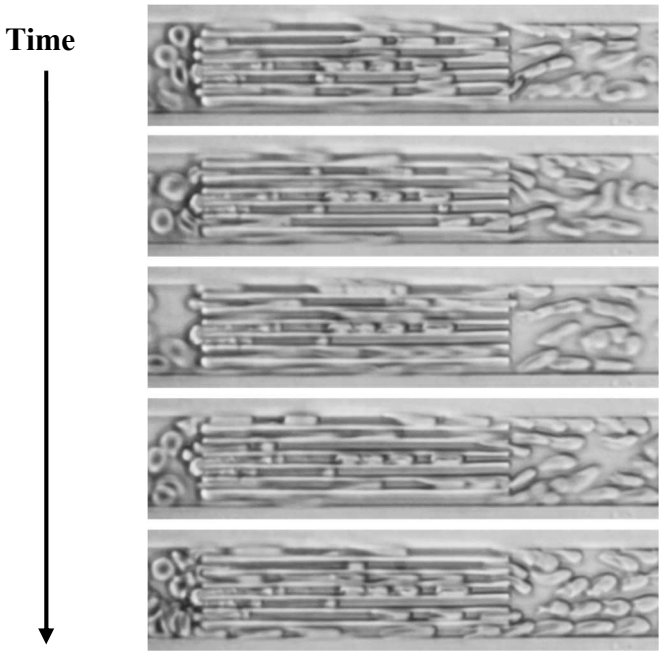

Figure 4.15. RBCs elastically deform through 90 µm canals with 3 µm x 3 µm cross section. Time lapse of RBCs traversing 90 µm canals (top to bottom). RBCs emerge with no significant morphology changes.

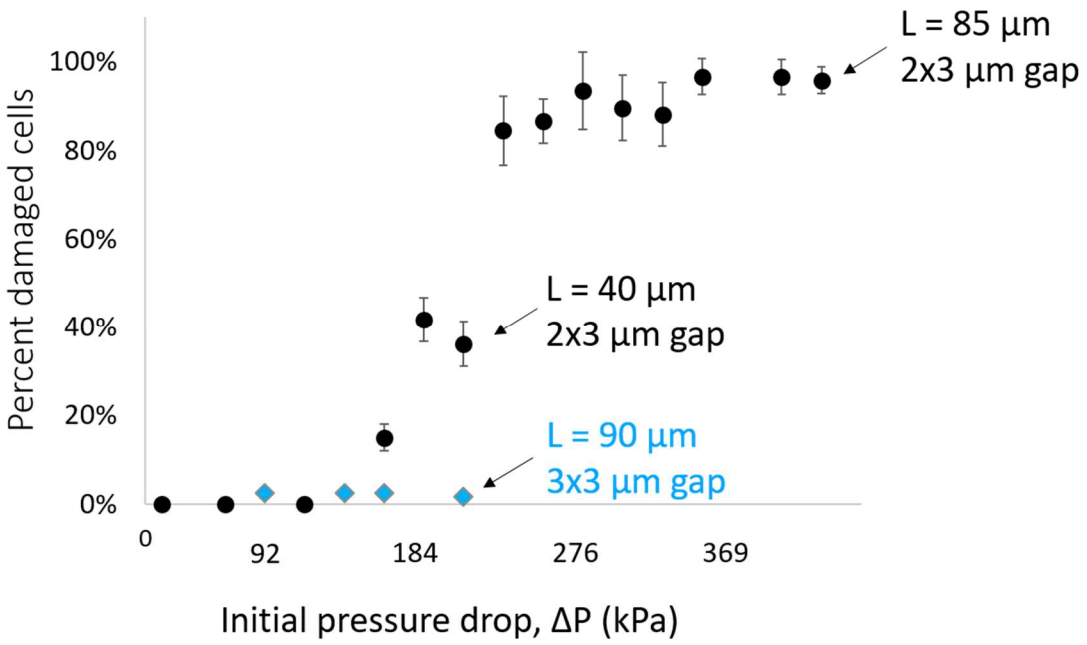

Figure 4.16. RBCs emerge from 3x3µm constriction with negligible damage. At the same initial pressure drop, 40% RBCs emerge damaged from the 2x3 µm constriction, while 0% emerge damaged from the 3x3 µm constriction.

More interestingly, preliminary evidence suggests that pathologically altered RBCs from a patient with sickle cell disease (SCD) fragment more readily than RBCs from healthy donors. It is known that pathologies introduce mechanical differences that change the ability of RBCs to deform through physically challenging matrices, and our finding suggest that mechanical changes shift the fragmentation profile. This has implications for hemolytic anemias in sickle cell disease. Furthermore, it appears that a subset of cells enter the array with a visibly "normal" morphology and emerge an irreversibly sickled cells (ISC) (Figure 4.17, white outline.traces ISC). For instance, at a canal length of 40 µm, ~40% of health RBCs emerge damaged, while ~90% of SCD RBCs emerge damaged (Figure 4.18.

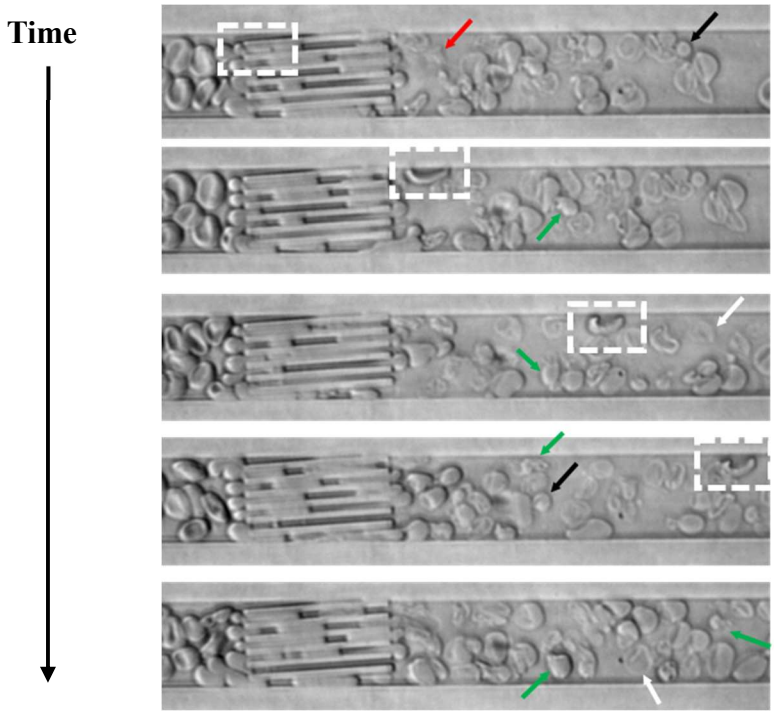

Figure 4.17. RBC from a sickle cell disease patient are significantly damaged after traversing 40 μm canals.Time lapse of sickle red blood cells emerging from canals shows various morphological abnormalities, including spherocytes (black), ghosts (white), and schistocytes (green). A cell also appears to be irreversibly sickled after transit (white dotted line).

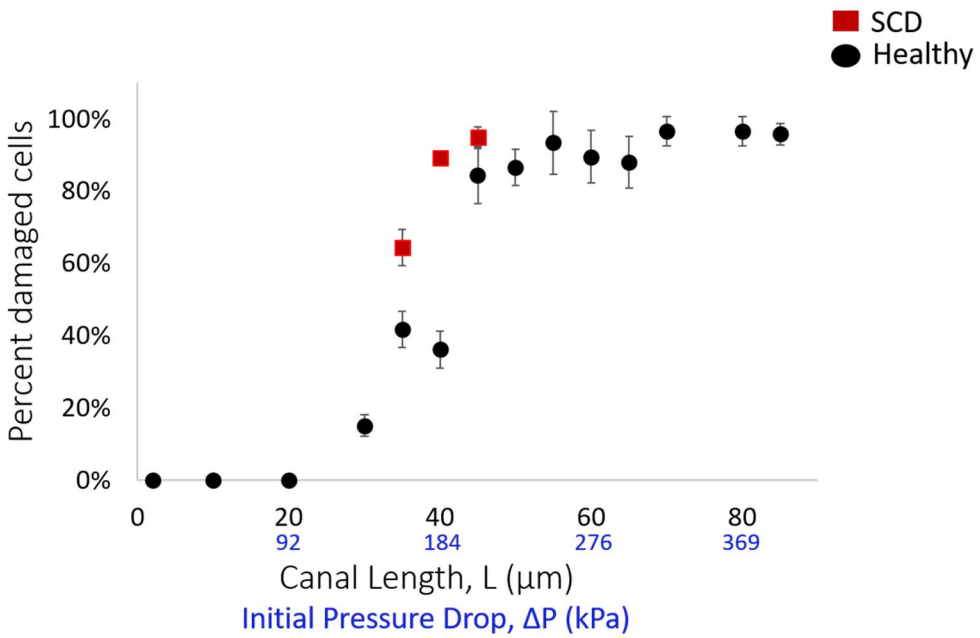

Figure 4.18. SCD RBCs fragment more readily than healthy RBCs. At the same canal lengths, RBCs from patients with SCD emerge more damaged than RBCs from healthy donors.

This study allows for the real-time visual analysis of RBC deformation and fragmentation, but the system is also marked by limitations. Because the processed sample volume is on the scale of picoliters, enumeration of cell subtypes from the effluent proves difficult. It is also not possible to draw direct correlation between pressure differentials and fragmentation profile, for as cells block the canals the pressure drop across the other canals changes. The pressure is thus dynamically changing throughout the experiments. Tighter control of these variables in future systems would yield more direct relationships between fragmentation and biophysical parameters.

4.3.3 Neutrophil Interaction with Microfluidic Matrices Results in Procoagulant NET-like Morphology

Neutrophils are the most numerous WBC subtype, comprising ~60% of the total WBC population, and they are well known as the "first responder" of the innate immune system as they migrate to sites of infection and phagocytose pathogens. In a process termed chemotaxis, neutrophils respond to chemoattractant signals to extravasate from the vasculature and respond to infection; it was recently shown that neutrophils are also involved in inflammation resolution via retrotaxis, reverse migration from sources of chemokines back to the vasculature.[102] Likewise, there is a wealth of recent literature that seeks to describe the process and biochemical pathways of NET (nuclear extracellular trap) formation, a process in which neutrophils release their nuclear material into the extracellular space. [103-106]

NETs are a meshwork of chromatin and DNA studded with histones and cytotoxic enzymes, and their release is thought to be part of the neutrophil's antimicrobial defense system, as NET entrapped pathogens are exposed to high concentrations of antimicrobial proteins. NETs are released in response to numerous factors, including inflammatory stimuli, contact with pathogens, and chemical activation; however, the *in vivo* circumstances in which neutrophils respond by forming NETs instead of phagocytosis is not well understood. NETs have been implicated as a complicating factor in numerous pathologies, such as sepsis, cystic fibrosis, and rheumatoid arthritis. [106] Furthermore, *in vivo*, NETs have been shown to be procoagulant and to play a role in pathological thrombosis.[107, 108] A recent *in vitro* study suggests that intact NETs do not directly stimulate coagulation, as measured by thrombin generation, and rather that NET components are procoagulant (histones proteins and neutrophil DNA).[109] Interestingly, it was recently reported that mechanical ventilation in patients with respiratory failure can

induce neutrophil extracellular trap formation: ventilation results in NETs, but the stimulus is unknown, as bacteria is necessary to recruit neutrophils to the lungs but not to create NETs. [110] These recent reports taken together suggest a role for a mechanical process in the formation of procoagulant "NET-like" structures. The mechanics of neutrophils, as studied through the previously described traditional assays, is well established. Mechanical changes during migration and activation have been described, and Yap and Kamm suggest that microfluidic constrictions can result in neutrophil activation and the formation of pseudopods.[111-113] Recently, a computational study described the fluidization of the neutrophil as it enters a constriction.[114] These studies give insight into the mechanical activation of neutrophils and further motivates our studies of neutrophil response through single-micron matrices.

When neutrophils are perfused through the microcanal device, neutrophils fragment into stringy, membranous material that adheres to the canals and aggregates under flow (Figure 4.19). This is the case for the canals with 5, 10, and 20 μm lengths (and their associated pressures) (Figure 4.20). Over time, membranous material from incoming neutrophils adds to the material that was left behind by previous passing neutrophils.

Figure 4.19. Neutrophil fragmentation. Schematic of neutrophil interaction with physical matrix

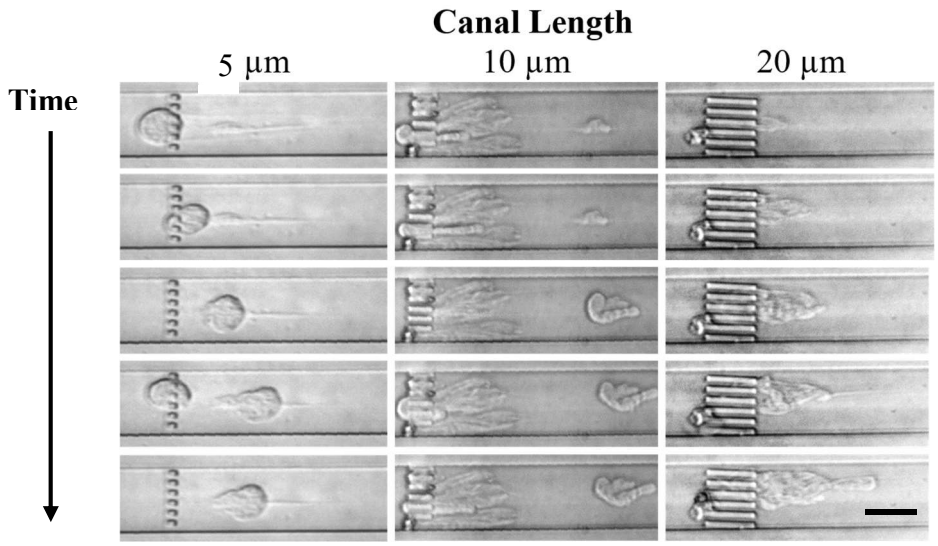

Figure 4.20. Time course of neutrophils perfused through microcanals. Neutrophils perfused through 5 µm, 10 µm, and 20 µm microcanals and fragment into membranous material that is tethered to the canals. Successive neutrophils add to the membranous material left behind from neutrophils that have previously interacted with the canals. Accumulation of material is evident when looking down the column for each canal length. Scale bar = 20 µm.

We confirm that the material adhered to the canals is indeed from neutrophils by staining with the membrane impermeable nucleic acid dye, Sytox green (Figure 4.21). Again, membranous material is tethered to the canals and accumulates over time as neutrophils are continuously perfused through the device. The remainder of neutrophil experiments were performed in the 20 µm canals as they provide improved scaffolding for neutrophil membrane attachment, and thus provide a better platform for the characterization of the membranous neutrophil material and its interactions with platelets. It is worth noting that the mechanical disruption of neutrophil membranes seen in the microcanals also occurs in the micropillar device, but as we are interested in the procoagulant nature of neutrophil material, we carried out all experiments in the microcanal device to avoid confounding results from platelet adherence due to the fluidic

environment in the micropillars. The fragmentation of neutrophils in both devices suggest that the required deformation is a more significant factor for formation of neutrophil membranous material than the extreme pressure differential or shear experienced in the canals.

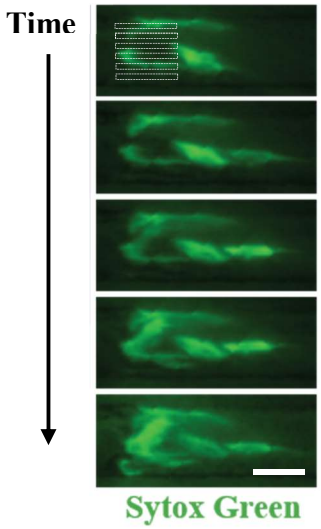

Figure 4.21. Time course of DNA accumulation at canals from fragmented, membranous neutrophils. Membranous neutrophil material represents a "dead" cell as it stained positive for membrane impermeable nucleic acid stains (sytox green). Accumulation of material can be seen as you move from the top to the bottom panel. White dotted "canals" represent location of canals in device. Scale bar = 20 μm.

To investigate whether the membranous neutrophil material forms a procoagulant surface we added isolated neutrophils to PRP at ~1 million cells/ mL and perfused the mixture through the 20 μL microcanal device (Figure 4.22). As expected, neutrophils (stained for DNA with hoescht) form tethered, membranous material at the microcanals, and platelets adhere specifically to the neutrophil material downstream of the canals.

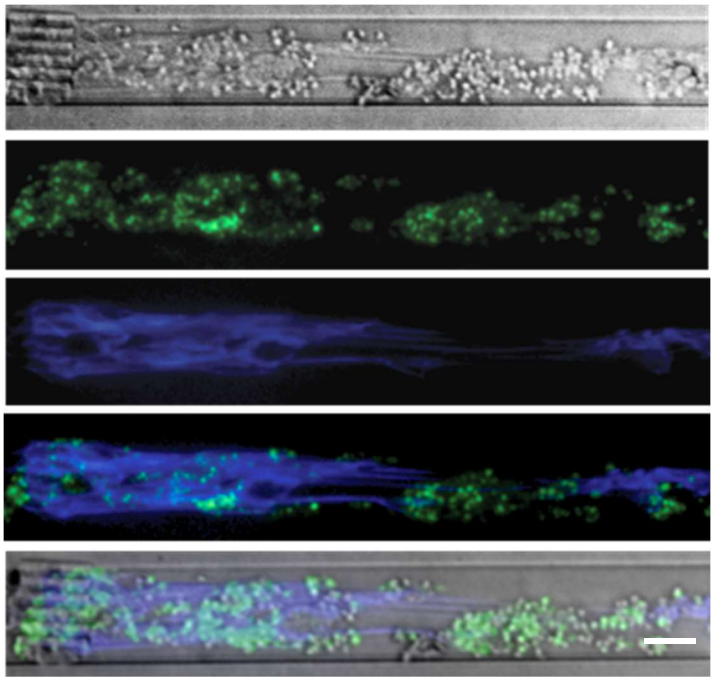

Figure 4.22. Platelets adhere to damaged neutrophil membrane. Platelets and neutrophils are perfused through 20 µm microcanals and platelets adhere to the membranous neutrophil material—platelets (CD41, green) and neutrophil DNA (hoescht, blue). Top panel: brightfield alone, Second: platelets alone, Third: neutrophils alone, Fourth: platelets and neutrophils, Fifth: all channels merged. Scale bar is 20 µm.

To further characterize the membranous material that arises from neutrophil's interacting with and transiting the microcanals, and to see whether they might be similar in composition to NETs, we added antibodies against histone H3, elastase, and MPO (Figure 4.23). The membranous structures tethered to the canals are in fact studded with histone, elastase, and MPO, all of which are considered to be integral components of NETs. When neutrophils in PRP are perfused through microcanals, there is some colocalization between platelets and histone, elastase, and MPO. It appears that the greatest colocalization occurs between platelets and MPO. Together, this suggests that the NET components implicated as prothrombotic are present on the surface of the mechanically induced neutrophil debris. This led me to refer to the neutrophil debris as NET-like structures.

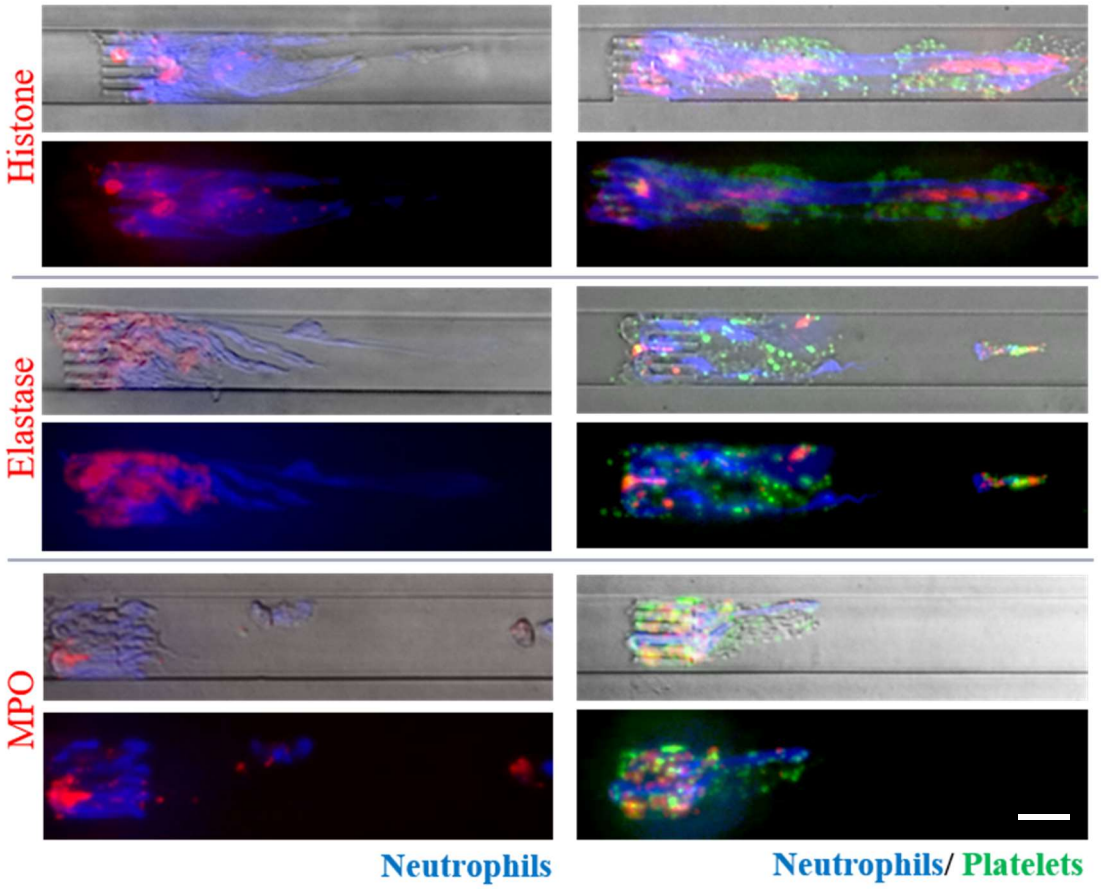

Figure 4.23. Mechanically induced NET-like material is studded with histone, elastase, and MPO, and forms a surface to which platelets adhere. Neutrophil membrane (DNA stained with hoescht) that is tethered to the microcanals displays histone, elastase, and MPO (red). Images are in pairs, with the top image comprising all channels and the bottom shown without brightfield. The left panel is neutrophils perfused on their own and the right panel is neutrophils mixed with PRP and perfused through the device. When platelets and neutrophils are perfused, the platelets adhere and aggregate on the membranous neutrophil material. Some colocalization is seen between platelets and traditional NET components, especially in the case of MPO. Scale bar is 20 μm.

NETs have been reported to bind to platelets, RBCs, and proteins and thereby promote thrombosis. [104] When RBCs and neutrophils are perfused together through the microcanals, RBCs do in fact become trapped in the tethered neutrophil membrane (Figure 4.24). RBCs take on a teardrop shape, whereby they are tethered at one end and elongate with the flow at the other (Figure 4.25). This suggests that mechanically disrupted neutrophils may have a role in RBC fragmentation and destruction. Neutrophils

then appear to form procoagulant NET-like structures when they are challenged by physical matrices (Figure 4.26).

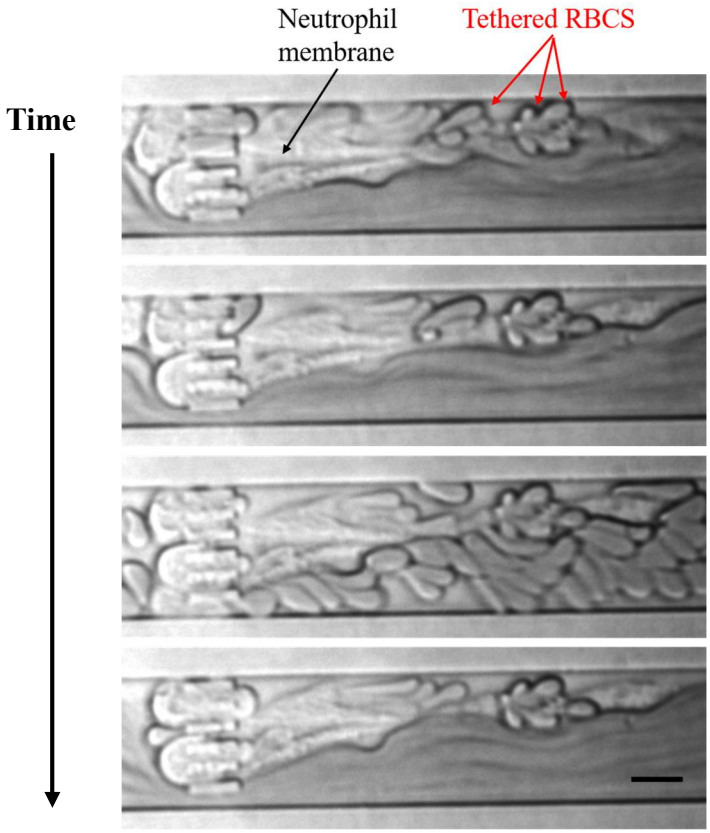

Figure 4.24. Time course of RBCs tethered in ruptured neutrophil membrane. RBCs and neutrophils are perfused through microcanals. As expected, neutrophils are damaged and display NET-like membranous structure as they traverse 20 µm microcanals RBCs interact with and become tethered in the neutrophil membranes. Scale bar is 20 µm.

Figure 4.25. RBCs trapped in neutrophil membrane. Mechanically induced neutrophil membranous material traps RBCs as they transit the canals and interact with the neutrophil membrane. RBCs are teadrop shaped as they appear to elongate with flow while their membrane is tethered to the neutrophil membrane material.

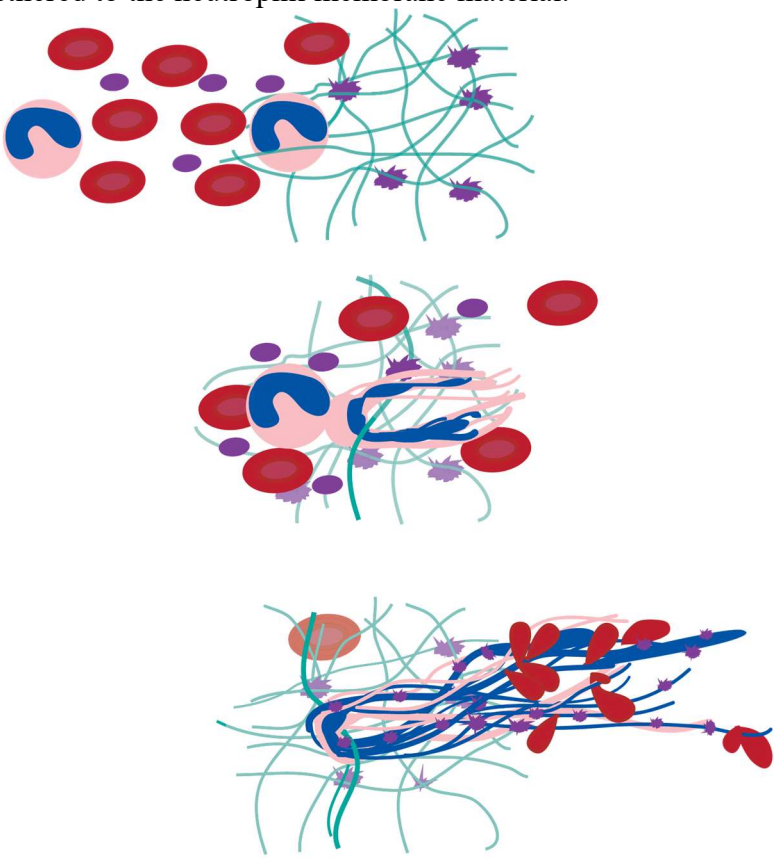

Figure 4.26. Platelets and RBCs interact with mechanically- induced NETs-like substrate Schematic shows the posited interaction of blood cells with a vascular matrix. As a neutrophil enters the matrix, it collides with fibers and fragments. The resulting NET-like material is procoagulant and also traps RBCs, possibly leading to their damage.

4.4 Conclusions

In this chapter we were able to leverage fabrication technologies to create a suite of microfluidic devices that allow for the real-time monitoring of blood cell transit through matrices whose dimensions are on the single micron scale. In doing so, we are able to recapitulate the passage of blood cells through physical challenges that are on the size scale of biological matrices, while still being able to decouple the effects of the physical presence of a matrix from the biological components of the matrix. Overall, we show that mechanical forces alone have significant, and sometimes surprising, effects on blood cells. We find that when platelets are perfused through a micropillar array (pillars are 900 nm in diameter, 3 μm in height, and there is a 2 μm gap between pillars), in the absence of agonists or biological ligands, platelets adhere in the array, aggregate, and the mass extends to the edges of the array until the channel is fully occluded. I posit that this spatially localized response to the physical presence of pillars is due to the shear microgradients created by the pillars and the stagnant zones throughout the array. Occlusion of the microchannel can be hastened by taking advantage of the synergy between the biophysical and the biochemical by adsorbing platelet ligands to the micropillars.

While it is known *in vivo* that RBCs fragment in response to mechanical forces, the mechanism of action of RBC fragmentation is not well understood. Although it was hypothesized that the extent of deformation required for RBCs to pass through the micropillar array would lead to RBC fragmentation, we found that RBCs were able to transit the pillar array without undergoing plastic deformation. This led us to consider the

temporal aspect of membrane remodeling that might result in fragmentation versus outright destruction of RBCs. To that end, we created a microfluidic device that features an array of canals to probe the deformation of cells as a function of time in deformed state. We found that over long periods of deformation (as controlled by the length of the canals) we could induce RBC fragmentation and watch fragmented cells exit the canals in real time. The extent of RBC damage, and thus the resulting morphological abnormality was dependent on the length of the canal (which corresponds both to residence time in deformed state and pressure differential). We were able to see mild, reversible damage in the form of echinocytes at short canal length, microspherocytes and schistocytes at intermediate lengths, and RBC ghosts and cell debris at the longest canal lengths. Preliminary findings suggest that pathologically abnormal cells (from a patient with SCD) show a different fragmentation profile than do healthy cells, and that extreme deformation may even induce irreversible sickling.

Finally, although NETs are thought to be created in response to biochemical stimuli provided by a pathogen or an inflammatory response, we show that by perfusing neutrophils through our microcanal device, we can create "NET-like" membranous structures that are marked by DNA, histone, elastase and MPO. Moreover, this mechanically damaged neutrophil membrane appears to be procoagulant: platelets adhere to the membranous substrate and colocalize with histone, elastase, and MPO. The recent report that NET components, as opposed to intact NETs, are procoagulant combined with our findings herein suggest that a purely mechanical stimulus could be implicated in the prothrombotic role of neutrophils. This neutrophil debris is further able to trap RBCs, at which point their membranes undergo deformation that can possibly lead to RBC ghosts

and fragmentation. In all, these findings suggest that there is an exquisite synergy between sepsis, microangiopathies, and hemolytic anemias that has roots in the three major cells present in blood, that may be at least in part mechanically regulated.

CHAPTER 5: CONCLUDING REMARKS AND FUTURE DIRECTIONS

Microfluidics provide a platform to study hematology in a reductionist manner that uniquely allows for the study of the independence and the interaction of the biophysical and biochemical aspects of hematology. My work shows that microfluidics can supplement *in vivo* studies, provide mechanistic insights into *in vivo* processes, and answer biophysical questions that were previously not technically feasible to answer. The long-term goal of this work is to determine how biophysical factors contribute to hematological processes, and thereby expand solution spheres for novel therapeutic targets and innovative diagnostics assays.

In the first part of my work, I was able to leverage microfluidics to resolve the mechanism of action of the most commonly used injury model for studying thrombosis—the $FeCl_3$-induced thrombosis model. My work with the $FeCl_3$ injury model shows the value of companion *in vitro* systems in determining the mechanisms of action of biological processes and in resolving discrepancies between findings in the literature. It also suggests ways in which *in vitro* systems could be used to supplement, or in some cases, replace animal-based injury models. I found that the initiating events in clotting in this injury model are non-biological in nature, and that researchers should use caution in interpreting their results if they choose to continue to use this model. Thus, my findings both inform future hematological research and serve to reconcile literature findings. While overall, this project serves as a closed chapter, it further suggests that biophysical factors, such as the role of mass transfer, should not be overlooked in biological assays.

The suite of devices that I created to probe the biophysical interactions of cells with physical challenges have provided exciting initial insights into blood cell/ matrix interactions, but these studies have served to inspire more questions about these processes. Our work shows that the physical presence of a matrix can lead to platelet adherence and aggregation. This provides insight into the fluidic environments that induce platelet activation and aggregation, and allows researchers to specify the location of a clot in their system. Elucidating the roles that additional matrix proteins play in this aggregation and in the propagation of the thrombus would enhance our findings.

Using the microcanal device we were able to show, for the first time, the real-time fragmentation of RBCs. The time dependency of fragmentation (or schistocyte formation) suggest that fragmentation is not an instantaneous process due to the application of a force, as it is often described in medical literature. Furthermore, our preliminary data from patient blood shows that sickle cell red blood cells show a much different fragmentation profile than does healthy blood. Moreover, cells emerged from the canals irreversibly sickled. These studies then begin to provide insight into the biophysical parameter space that results in schistocyte formation, but there are certainly limitations in our experiments: namely, that pressure is not tightly controlled in our system and thus the pressure that cells are exposed to changes dynamically as canals are blocked by transiting cells. Further studies should aim to create a pressure controlled system and/or a system in which pressure and residence time in a deformed state can be considered separately. Moreover, schistocytes are said to form *in vivo* when red blood cells interact with fine fibrin strands. Creating a device using technology, such as the new Nanoscribe 3D printer, with which a repeatable, biophysical, nanoscale matrix could be created to view these more physiologically similar

interactions would provide additional insights. Likewise, integration of a viewing window where different RBC morphologies could be more accurately enumerated, would provide additional information.

Our suite of microdevices also suggests for the first time that the biophysical presence of a matrix can mechanically disrupt neutrophils and create NET-like structures whose surface is procoagulant and studded with MPO, elastase, and histone. Further studies into these mechanically-induced "NETs" could provide a clear link between inflammation and thrombosis. Not only do platelets adhere to the neutrophil membranous material, but RBCs are trapped within the fibrous strands and are seen to be in a deformed state. Neutrophils could therefore be playing a significant role in schistocyte formation and hemolytic anemias. It is further posited that the stiffness changes resulting from the exposure of neutrophils to inflammatory stimuli, would predispose neutrophils to mechanically-induced fragmentation. This would further support a synergistic relationship in sepsis, NET formation, microangiopathies, and hemolytic anemias. Our work therefore begins to explore new areas of research that are based on biophysical interactions. Considering alternative therapeutic targets that stem from newly discovered biophysical mechanisms could greatly influence the field of hematology.

REFERENCES

1. Discher, D.E., Janmey, P. & Wang, Y.L. Tissue cells feel and respond to the stiffness of their substrate. *Science (New York, N.Y.)* **310**, 1139-1143 (2005).
2. Chen, C.S. Mechanotransduction – a field pulling together? *Journal of cell science* **121**, 3285-3292 (2008).
3. Fogelson, A.L. & Neeves, K.B. Fluid Mechanics of Blood Clot Formation. *Annual review of fluid mechanics* **47**, 377-403 (2015).
4. Rumbaut, R.E. & Thiagarajan, P. Platelet-Vessel Wall Interactions in Hemostasis and Thrombosis. *Colloquium Series on Integrated Systems Physiology: From Molecule to Function* **2**, 1-75 (2010).
5. Berkner, K.L. in eLS (John Wiley & Sons, Ltd, 2001).
6. Whitesides, G.M. The origins and the future of microfluidics. *Nature* **442**, 368-373 (2006).
7. Whitesides, G.M., Ostuni, E., Takayama, S., Jiang, X. & Ingber, D.E. Soft lithography in biology and biochemistry. *Annual review of biomedical engineering* **3**, 335-373 (2001).
8. Shin, Y. et al. Microfluidic assay for simultaneous culture of multiple cell types on surfaces or within hydrogels. *Nature protocols* **7**, 1247-1259 (2012).
9. Myers, D.R. et al. Endothelialized microfluidics for studying microvascular interactions in hematologic diseases. *Journal of visualized experiments : JoVE* (2012).
10. Moolman, M.C., Huang, Z., Krishnan, S.T., Kerssemakers, J.W. & Dekker, N.H. Electron beam fabrication of a microfluidic device for studying submicron-scale bacteria. *Journal of nanobiotechnology* **11**, 12 (2013).
11. Russell, M.T., Pingree, L.S., Hersam, M.C. & Marks, T.J. Microscale features and surface chemical functionality patterned by electron beam lithography: a novel route to poly(dimethylsiloxane) (PDMS) stamp fabrication. *Langmuir : the ACS journal of surfaces and colloids* **22**, 6712-6718 (2006).
12. Huang, S. et al. Towards microfluidic-based depletion of stiff and fragile human red cells that accumulate during blood storage. *Lab on a chip* **15**, 448-458 (2015).
13. Wang, G. et al. Microfluidic cellular enrichment and separation through differences in viscoelastic deformation. *Lab on a chip* **15**, 532-540 (2015).
14. Sulchek, T. Biomechanical Identification and Sorting of Single Cells. *Biophysical journal* **110**, 342a.
15. Hur, S.C., Henderson-MacLennan, N.K., McCabe, E.R. & Di Carlo, D. Deformability-based cell classification and enrichment using inertial microfluidics. *Lab on a chip* **11**, 912-920 (2011).
16. Hochmuth, R.M. Micropipette aspiration of living cells. *Journal of biomechanics* **33**, 15-22 (2000).
17. Ashkin, A. & Dziedzic, J.M. Optical trapping and manipulation of viruses and bacteria. *Science (New York, N.Y.)* **235**, 1517-1520 (1987).
18. Moffitt, J.R., Chemla, Y.R., Smith, S.B. & Bustamante, C. Recent advances in optical tweezers. *Annual review of biochemistry* **77**, 205-228 (2008).

19. Radmacher, M., Fritz, M., Kacher, C.M., Cleveland, J.P. & Hansma, P.K. Measuring the viscoelastic properties of human platelets with the atomic force microscope. *Biophysical journal* **70**, 556-567 (1996).
20. Rotsch, C., Jacobson, K. & Radmacher, M. Dimensional and mechanical dynamics of active and stable edges in motile fibroblasts investigated by using atomic force microscopy. *Proceedings of the National Academy of Sciences of the United States of America* **96**, 921-926 (1999).
21. Korin, N., Bransky, A. & Dinnar, U. Theoretical model and experimental study of red blood cell (RBC) deformation in microchannels. *Journal of biomechanics* **40**, 2088-2095 (2007).
22. Adamo, A. et al. Microfluidics-Based Assessment of Cell Deformability. *Analytical chemistry* **84**, 6438-6443 (2012).
23. Fay, M.E. et al. Cellular softening mediates leukocyte demargination and trafficking, thereby increasing clinical blood counts. *Proceedings of the National Academy of Sciences of the United States of America* **113**, 1987-1992 (2016).
24. Bennett, V. The membrane skeleton of human erythrocytes and its implications for more complex cells. *Annual review of biochemistry* **54**, 273-304 (1985).
25. Chien, S. Red cell deformability and its relevance to blood flow. *Annual review of physiology* **49**, 177-192 (1987).
26. Guo, Q. et al. Microfluidic analysis of red blood cell deformability. *Journal of biomechanics* **47**, 1767-1776 (2014).
27. Kwan, J.M., Guo, Q., Kyluik-Price, D.L., Ma, H. & Scott, M.D. Microfluidic analysis of cellular deformability of normal and oxidatively damaged red blood cells. *American journal of hematology* **88**, 682-689 (2013).
28. Myrand-Lapierre, M.-E. et al. Multiplexed fluidic plunger mechanism for the measurement of red blood cell deformability. *Lab on a chip* **15**, 159-167 (2015).
29. Salehyar, S. & Zhu, Q. Deformation and internal stress in a red blood cell as it is driven through a slit by an incoming flow. *Soft Matter* **12**, 3156-3164 (2016).
30. Salehyar, S. & Zhu, Q. Effects of stiffness and volume on the transit time of an erythrocyte through a slit. *Biomechanics and modeling in mechanobiology* **16**, 921-931 (2017).
31. Picot, J. et al. A biomimetic microfluidic chip to study the circulation and mechanical retention of red blood cells in the spleen. *American journal of hematology* **90**, 339-345 (2015).
32. Pivkin, I.V. et al. Biomechanics of red blood cells in human spleen and consequences for physiology and disease. *Proceedings of the National Academy of Sciences of the United States of America* **113**, 7804-7809 (2016).
33. Picot, J. et al. A biomimetic microfluidic chip to study the circulation and mechanical retention of red blood cells in the spleen. *American journal of hematology* **90**, 339-345 (2015).
34. Duez, J. et al. Mechanical clearance of red blood cells by the human spleen: Potential therapeutic applications of a biomimetic RBC filtration method. *Transfusion clinique et biologique : journal de la Societe francaise de transfusion sanguine* **22**, 151-157 (2015).
35. Deplaine, G. et al. The sensing of poorly deformable red blood cells by the human spleen can be mimicked in vitro. *Blood* **117**, e88-95 (2011).

36. Sakuma, S. et al. Red blood cell fatigue evaluation based on the close-encountering point between extensibility and recoverability. *Lab on a chip* **14**, 1135-1141 (2014).
37. Ito, H. et al. Mechanical diagnosis of human erythrocytes by ultra-high speed manipulation unraveled critical time window for global cytoskeletal remodeling. *Scientific reports* **7**, 43134 (2017).
38. Horade, M., Tsai, C.-H., Ito, H. & Kaneko, M. Red Blood Cell Responses during a Long-Standing Load in a Microfluidic Constriction. *Micromachines* **8**, 100 (2017).
39. Bain, B.J. Blood Cells: A Practical Guide. (Wiley, 2008).
40. DiBella, N.J., Silverstein, M.N. & Hoagland, H.C. Effect of splenectomy on teardrop-shaped erythrocytes in agnogenic myeloid metaplasia. *Archives of internal medicine* **137**, 380-381 (1977).
41. Orkin, S.H. & Nathan, D.G. Nathan and Oski's Hematology of Infancy and Childhood. (Saunders/Elsevier, 2009).
42. Eysholdt, K.-G. Die experimentelle Thrombose und ihre Beeinflussung durch Heparin und Heparinoide. *Arch. f. klin. Chir* **277**, 455-470 (1954).
43. Kurz, K.D., Main, B.W. & Sandusky, G.E. Rat model of arterial thrombosis induced by ferric chloride. *Thrombosis research* **60**, 269-280 (1990).
44. Farrehi, P.M., Ozaki, C.K., Carmeliet, P. & Fay, W.P. Regulation of arterial thrombolysis by plasminogen activator inhibitor-1 in mice. *Circulation* **97**, 1002-1008 (1998).
45. Denis, C. et al. A mouse model of severe von Willebrand disease: defects in hemostasis and thrombosis. *Proceedings of the National Academy of Sciences of the United States of America* **95**, 9524-9529 (1998).
46. Wang, X. et al. Effects of factor XI deficiency on ferric chloride-induced vena cava thrombosis in mice. *Journal of thrombosis and haemostasis : JTH* **4**, 1982-1988 (2006).
47. Joglekar, M.V., Ware, J., Xu, J., Fitzgerald, M.E. & Gartner, T.K. Platelets, glycoprotein Ib-IX, and von Willebrand factor are required for FeCl(3)-induced occlusive thrombus formation in the inferior vena cava of mice. *Platelets* **24**, 205-212 (2013).
48. Westrick, R.J., Winn, M.E. & Eitzman, D.T. Murine models of vascular thrombosis (Eitzman series). *Arteriosclerosis, thrombosis, and vascular biology* **27**, 2079-2093 (2007).
49. Konstantinides, S. et al. Distinct antithrombotic consequences of platelet glycoprotein Ibalpha and VI deficiency in a mouse model of arterial thrombosis. *Journal of thrombosis and haemostasis : JTH* **4**, 2014-2021 (2006).
50. Massberg, S. et al. A crucial role of glycoprotein VI for platelet recruitment to the injured arterial wall in vivo. *The Journal of experimental medicine* **197**, 41-49 (2003).
51. Eckly, A. et al. Mechanisms underlying FeCl3-induced arterial thrombosis. *Journal of thrombosis and haemostasis : JTH* **9**, 779-789 (2011).
52. Barr, J.D., Chauhan, A.K., Schaeffer, G.V., Hansen, J.K. & Motto, D.G. Red blood cells mediate the onset of thrombosis in the ferric chloride murine model. *Blood* **121**, 3733-3741 (2013).

53. Chauhan, A.K., Kisucka, J., Lamb, C.B., Bergmeier, W. & Wagner, D.D. von Willebrand factor and factor VIII are independently required to form stable occlusive thrombi in injured veins. *Blood* **109**, 2424-2429 (2007).
54. Owens, A.P., 3rd et al. Towards a standardization of the murine ferric chloride-induced carotid arterial thrombosis model. *Journal of thrombosis and haemostasis : JTH* **9**, 1862-1863 (2011).
55. Kanaji, T., Russell, S. & Ware, J. Amelioration of the macrothrombocytopenia associated with the murine Bernard-Soulier syndrome. *Blood* **100**, 2102-2107 (2002).
56. Tsai, M. et al. In vitro modeling of the microvascular occlusion and thrombosis that occur in hematologic diseases using microfluidic technology. *The Journal of clinical investigation* **122**, 408-418 (2012).
57. LIde, D.R.K., Henry V CRC Handbook of Thermophysical and Thermochemical Data, Vol. 1. (CRC Press, 1994).
58. Lacolley, P. et al. Mechanical properties and structure of carotid arteries in mice lacking desmin. *Cardiovascular research* **51**, 178-187 (2001).
59. Rudic, R.D., Bucci, M., Fulton, D., Segal, S.S. & Sessa, W.C. Temporal events underlying arterial remodeling after chronic flow reduction in mice: correlation of structural changes with a deficit in basal nitric oxide synthesis. *Circulation research* **86**, 1160-1166 (2000).
60. Parzy, E., Miraux, S., Jean-Michel, F. & Thiaudière, E. In vivo quantification of blood velocity in mouse carotid and pulmonary arteries by ECG-triggered 3D time-resolved magnetic resonance angiography. *NMR in Biomedicine* **22**, 532-537 (2009).
61. Hartley, C.J. et al. Noninvasive ultrasonic measurement of arterial wall motion in mice. *American journal of physiology. Heart and circulatory physiology* **287**, H1426-1432 (2004).
62. Truskey, G.A.Y., Fan; Katz, David F Transport Phenomena in Biological Systems Edn. 2. (Pearson Prentice Hall, Upper Saddle River, N.J.; 2009).
63. Blesa, M.A. & Matijević, E. Phase transformations of iron oxides, oxohydroxides, and hydrous oxides in aqueous media. *Advances in colloid and interface science* **29**, 173-221 (1989).
64. Matilainen, A., Vepsalainen, M. & Sillanpaa, M. Natural organic matter removal by coagulation during drinking water treatment: A review. *Advances in colloid and interface science* **159**, 189-197 (2010).
65. Flynn, C.M. HYDROLYSIS OF INORGANIC IRON(III) SALTS. *Chemical Reviews* **84**, 31-41 (1984).
66. Stefansson, A. Iron (III) hydrolysis and solubility at 25 degrees C. *Environmental science & technology* **41**, 6117-6123 (2007).
67. Hoeschele, J.D., Turner, J.E. & England, M.W. QSAR in Environmental Toxicology Inorganic concepts relevant to metal binding, activity, and toxicity in a biological system. *Science of The Total Environment* **109**, 477-492 (1991).
68. Duan, J. & Gregory, J. Coagulation by hydrolysing metal salts. *Advances in colloid and interface science* **100–102**, 475-502 (2003).
69. Neeves, K.B. Physiochemical artifacts in FeCl3 thrombosis models. *Blood* **126**, 700-701 (2015).

70. Wolters, M. et al. MRI artifacts in the ferric chloride thrombus animal model: an alternative solution: preventing MRI artifacts after thrombus induction with a non-ferromagnetic Lewis acid. *Journal of thrombosis and haemostasis : JTH* **11**, 1766-1769 (2013).
71. Hoeschele, J.D., Turner, J.E. & England, M.W. Inorganic concepts relevant to metal binding, activity, and toxicity in a biological system. *The Science of the total environment* **109-110**, 477-492 (1991).
72. Pusey, P.N. & Van Megen, W. Dynamic light scattering by non-ergodic media. *Physica A: Statistical Mechanics and its Applications* **157**, 705-741 (1989).
73. Surin, W.R., Prakash, P., Barthwal, M.K. & Dikshit, M. Optimization of ferric chloride induced thrombosis model in rats: effect of anti-platelet and anti-coagulant drugs. *Journal of pharmacological and toxicological methods* **61**, 287-291 (2010).
74. Bird, J.E. et al. Prediction of the therapeutic index of marketed anti-coagulants and anti-platelet agents by guinea pig models of thrombosis and hemostasis. *Thrombosis research* **123**, 146-158 (2008).
75. Wang, X. et al. Effects of factor IX or factor XI deficiency on ferric chloride-induced carotid artery occlusion in mice. *Journal of thrombosis and haemostasis : JTH* **3**, 695-702 (2005).
76. Schwarz, M. et al. Conformation-specific blockade of the integrin GPIIb/IIIa: a novel antiplatelet strategy that selectively targets activated platelets. *Circulation research* **99**, 25-33 (2006).
77. Ciciliano, J.C. et al. Resolving the multifaceted mechanisms of the ferric chloride thrombosis model using an interdisciplinary microfluidic approach. *Blood* **126**, 817-824 (2015).
78. Discher, D.E., Mooney, D.J. & Zandstra, P.W. Growth factors, matrices, and forces combine and control stem cells. *Science (New York, N.Y.)* **324**, 1673-1677 (2009).
79. Blombäck, B. & Okada, M. Fibrin gel structure and clotting time. *Thrombosis research* **25**, 51-70 (1982).
80. Okada, M., Blombäck, B., Chang, M.D. & Horowitz, B. Fibronectin and fibrin gel structure. *Journal of Biological Chemistry* **260**, 1811-1820 (1985).
81. Xiao, J. et al. PDMS micropillar-based microchip for efficient cancer cell capture. *RSC Advances* **5**, 52161-52166 (2015).
82. Sniadecki, N.J. et al. Magnetic microposts as an approach to apply forces to living cells. *Proceedings of the National Academy of Sciences of the United States of America* **104**, 14553-14558 (2007).
83. Sniadecki, N.J. & Chen, C.S. Microfabricated silicone elastomeric post arrays for measuring traction forces of adherent cells. *Methods in cell biology* **83**, 313-328 (2007).
84. Guido, S. & Tomaiuolo, G. Microconfined flow behavior of red blood cells in vitro. *Comptes Rendus Physique* **10**, 751-763 (2009).
85. Myrand-Lapierre, M.E. et al. Multiplexed fluidic plunger mechanism for the measurement of red blood cell deformability. *Lab on a chip* **15**, 159-167 (2015).
86. Guo, Q. et al. Microfluidic analysis of red blood cell deformability. *Journal of biomechanics* **47**, 1767-1776 (2014).

87. McAuley, S.A. et al. Silicon micromachining using a high-density plasma source. *Journal of Physics D: Applied Physics* **34**, 2769 (2001).
88. Hynes, A.M. et al. Recent advances in silicon etching for MEMS using the ASE™ process. *Sensors and Actuators A: Physical* **74**, 13-17 (1999).
89. Hathcock, J.J. Flow Effects on Coagulation and Thrombosis. *Arteriosclerosis, thrombosis, and vascular biology* **26**, 1729-1737 (2006).
90. Oh, K.W., Lee, K., Ahn, B. & Furlani, E.P. Design of pressure-driven microfluidic networks using electric circuit analogy. *Lab on a chip* **12**, 515-545 (2012).
91. in Laminar Flow Forced Convection in Ducts. (ed. A.L. London) ii (Academic Press, 1978).
92. Doggett, T.A. et al. Selectin-like kinetics and biomechanics promote rapid platelet adhesion in flow: the GPIb(alpha)-vWF tether bond. *Biophysical journal* **83**, 194-205 (2002).
93. Mody, N.A. & King, M.R. Platelet adhesive dynamics. Part II: high shear-induced transient aggregation via GPIbalpha-vWF-GPIbalpha bridging. *Biophysical journal* **95**, 2556-2574 (2008).
94. Kaplan, Z.S. & Jackson, S.P. The role of platelets in atherothrombosis. *Hematology. American Society of Hematology. Education Program* **2011**, 51-61 (2011).
95. Dasi, L.P., Simon, H.A., Sucosky, P. & Yoganathan, A.P. FLUID MECHANICS OF ARTIFICIAL HEART VALVES. *Clinical and experimental pharmacology & physiology* **36**, 225-237 (2009).
96. Gutierrez, E. et al. Microfluidic devices for studies of shear-dependent platelet adhesion. *Lab on a chip* **8**, 1486-1495 (2008).
97. Savage, B., Saldívar, E. & Ruggeri, Z.M. Initiation of Platelet Adhesion by Arrest onto Fibrinogen or Translocation on von Willebrand Factor. *Cell* **84**, 289-297 (1996).
98. Nesbitt, W.S. et al. A shear gradient-dependent platelet aggregation mechanism drives thrombus formation. *Nature medicine* **15**, 665-673 (2009).
99. Zini, G. et al. ICSH recommendations for identification, diagnostic value, and quantitation of schistocytes. *International journal of laboratory hematology* **34**, 107-116 (2012).
100. Bull, B.S. & Kuhn, I.N. The production of schistocytes by fibrin strands (a scanning electron microscope study). *Blood* **35**, 104-111 (1970).
101. Rosenblatt, P. et al. Schistocytes, echinocytes, iron deficiency anemia, and thrombocytopenia - hematologic manifestations of splenic angiosarcoma. *Archives of Iranian medicine* **16**, 602-605 (2013).
102. Mathias, J.R. et al. Resolution of inflammation by retrograde chemotaxis of neutrophils in transgenic zebrafish. *Journal of leukocyte biology* **80**, 1281-1288 (2006).
103. Brinkmann, V. et al. Neutrophil extracellular traps kill bacteria. *Science (New York, N.Y.)* **303**, 1532-1535 (2004).
104. Zawrotniak, M. & Rapala-Kozik, M. Neutrophil extracellular traps (NETs) - formation and implications. *Acta biochimica Polonica* **60**, 277-284 (2013).

105. Kaplan, M.J. & Radic, M. Neutrophil extracellular traps: double-edged swords of innate immunity. *Journal of immunology (Baltimore, Md. : 1950)* **189**, 2689-2695 (2012).
106. Yipp, B.G. et al. Infection-induced NETosis is a dynamic process involving neutrophil multitasking in vivo. *Nature medicine* **18**, 1386-1393 (2012).
107. Varju, I. et al. DNA, histones and neutrophil extracellular traps exert anti-fibrinolytic effects in a plasma environment. *Thrombosis and haemostasis* **113**, 1289-1298 (2015).
108. Fuchs, T.A. et al. Extracellular DNA traps promote thrombosis. *Proceedings of the National Academy of Sciences of the United States of America* **107**, 15880-15885 (2010).
109. Noubouossie, D.F. et al. In vitro activation of coagulation by human neutrophil DNA and histone proteins but not neutrophil extracellular traps. *Blood* **129**, 1021-1029 (2017).
110. Yildiz, C. et al. Mechanical ventilation induces neutrophil extracellular trap formation. *Anesthesiology* **122**, 864-875 (2015).
111. Wu, T. & Feng, J.J. Modeling the Mechanosensitivity of Neutrophils Passing through a Narrow Channel. *Biophysical journal* **109**, 2235-2245 (2015).
112. Ekpenyong, A.E. et al. Mechanical deformation induces depolarization of neutrophils. *Science advances* **3**, e1602536 (2017).
113. Wang, Q. et al. Changes in the biomechanical properties of neutrophils and endothelial cells during adhesion. *Blood* **97**, 660-668 (2001).
114. Yap, B. & Kamm, R.D. Mechanical deformation of neutrophils into narrow channels induces pseudopod projection and changes in biomechanical properties. *Journal of applied physiology (Bethesda, Md. : 1985)* **98**, 1930-1939 (2005).